IChF
Institute of Physical Chemistry PAS

INFLUENCE OF MORPHOLOGY ON THE PLASMONIC PROPERTIES OF CHEMICALLY SYNTHESIZED SILVER NANOWIRES: EXPERIMENTAL AND NUMERICAL STUDIES

PhD thesis by

Michał Ćwik

prepared under supervision of:

prof. dr hab. Joanna Niedziółka-Jönsson

within the International PhD Studies at the
Institute of Physical Chemistry
of the Polish Academy of Sciences
Kasprzaka 44/52, 01-224 Warsaw

May 2025

Acknowledgements

The research presented in this dissertation would not have been possible without the support, encouragement, and collaboration of many individuals.

I would like to express my sincere gratitude to those who supported my work and academic development throughout my doctoral journey. I am particularly thankful to **prof. Joanna Niedziółka-Jönsson** for her involvement during the supervision of my doctoral research.

My appreciation also goes to **dr. Dorota Buczyńska** and **dr. Karolina Sulowska**, whose technical assistance and commitment were invaluable during the experimental phases, particularly in managing and troubleshooting laboratory equipment.

I am grateful to **dr. Saeid Izadshenas** and **dr. hab. Karolina Słowik** for introducing me to the field of numerical simulations and for their insightful input during our collaborative efforts.

A heartfelt thank you goes to all my colleagues from the **Surface Nanoengineering Group** and the **Department of Nanophotonics**, whose camaraderie, intellectual exchange, and support helped make this PhD experience both productive and personally enriching.

Lastly, I wish to acknowledge those challenges and circumstances that tested my perseverance. Despite them, I remain proud of the work I have accomplished and the integrity with which I approached it.

This research was supported by the Narodowe Centrum Nauki, Grant Sonata Bis 2016/22/E/ST5/00531

Abbrevations

ABT - 4-aminobenzenothiol

AFM – atomic force microscope

AgNWs – silver nanowires

APD – avalanche photodiode

CCD - charge-coupled device

Chl A – chlorophyll A

CMOS - Complementary Metal-Oxide-Semiconductor

CTAB - N,N,N-Trimethylhexadecan-1-aminium bromide

CVD – chemical vapor deposition

DNA - deoxyribonucleic acid

EDC - 1-ethyl-3-(-3-dimethylaminopropyl) carbodiimide hydrochloride

EDTA - Ethylenediaminetetraacetic acid

fcc – face centered cubic system

FDTD – finite differences time domain

FEM – finite elements method

FWHM – full width at the half maximum

HE – hybrid electric mode

his-tag - hexahistidine-tagged

LED - light-emitting diode

LSPR – localised surface plasmon resonance

NA – numerical aperture

NHS - N-hydroxysuccinimide

NPs – nanoparticles

OTMS - Octadecyltrimethoxysilane

PCP – peridinin chlorophyll protein

Per – peridinin

PVA -polyvinyl alcohol

PVD – physical vapor deposition

PVP – polyvinylpyrrolidone

QDs – quantum dots

rhcp - random hexagonal close-packing

SAv-PerC – bioconjugate of PCP and streptavidin

SEM – scanning electron microscope

SPP – surface plasmon polaritons

TCSPC - Time-correlated single-photon counting

TM – transverse magnetic mode

Contents

Streszczenie

Głównym celem niniejszej rozprawy było otrzymane nanodrutów srebra o różnej morfologii wykorzystując do tego syntezę chemiczną. Następnie wykazanie wpływu morfologii nanodrutów srebra na ich właściwości optyczne (wzmocnienie fluorescencji i długości propagacji powierzchniowych polarytonów plazmonowych), wykorzystując do tego metody mikroskopii fluorescencyjnej, gdzie rolę fluorofora pełnił kompleks perydynina-chlorofil-białko oraz metody numeryczne do symulacji oddziaływań fal elektromagnetycznych z materią.

Pierwszy rozdział stanowi wstęp teoretyczny dla tej rozprawy. Omówione są w nim metody syntezy nanocząstek (ze szczególnym uwzględnieniem nanodrutóww srebra) i zjawiska fizyczne zachodzące w czasie wzrostu nanokryształów oraz chemiczna modyfikacja powierzchni nanocząstek. Kolejną część stanowi opis oddziaływania nanocząstek i fluoroforów ze światłem, których znajomość jest kluczowa dla zrozumienia oddziaływań pomiędzy nanocząstkami i fluoroforami. Podsumowanie stanowi przegląd literaturowy zawierający kluczowe wyniki badań dotyczące wzmocnienia fluorescencji przez nanocząstki i tłumienia powierzchniowych polarytonów plazmonowych. Wyniki te koncentrują się na wzmocnieniu fluorescencji molekuł przez nanodruty srebra oraz analizie modów powierzchniowych polarytonów plazmonowych w zależności od morfologii.

Drugi rozdział opisuje użyte materiały, techniki eksperymentalne i pomiarowe. Opisane są w nim główne techniki eksperymentalne wykorzystane w pracy: fluorescencyjna mikroskopia szerokiego pola, fluorescencyjna mikroskopia konfokalna oraz spektroskopia czasowo-rozdzielcza, skaningowa mikroskopia elektronowa, spektrolfuorymetria i spektroskopia UV-Vis. Przedstawione są schematy wykorzystanych mikroskopów optycznych wraz z detalami technicznymi. Zakończenie rozdziału stanowią opisy metod numerycznych. W symulacjach oddziaływania nanodrutów srebra ze światłem wykorzystano metodę elementów skończonych zaimplementowaną w oprogramowaniu COMSOL.

W rozdziale trzecim przedstawiono wyniki badań własnych. Jako pierwsza została opisana synteza hydrotermalna o różnych składach mieszanin do redukcji, prowadząca do nanodrutów srebra o odmiennych morfologiach. Właściwości optyczne nanodrutów srebra badano w dwóch konfiguracjach: 1)matrycy polimerowej z białkiem fotoaktywnym PCP i 2) monowarstwie PCP pokrywającej nanodruty. Do zbadania wzmocnienia fluorescencji przez nanodruty srebra i tłumienia propagacji powierzchniowych polarytonów plazmonowych wykorzystano zarówno techniki teoretyczne jak i ekperymentalne. W ostatniej części przedstawiono metodę lokalnej modyfikacji nanodrutu srebra za pomocą PCP oraz dowiedziono, że struktury uzyskane w wyniku syntezy opisanej w tej pracy mogą być wykorzystane do wzbudzania molekuł znajdujących się w odległości 100 µm od ich końca, na który pada światło lasera. Ostatni rozdział pracy stanowi podsumowanie wyników.

Introduction

The main aim of this thesis was to obtain silver nanowires of various morphologies using chemical synthesis. It then aimed to demonstrate the influence of silver nanowire morphology on their optical properties. These properties included the enhancement of fluorescence and the propagation length of surface plasmon polaritons. Fluorescence microscopy methods were used for this analysis, with a peridinin-chlorophyll-protein complex as the fluorophore. Additionally, numerical methods were applied to describe the interactions of electromagnetic waves with matter.

The first chapter serves as a theoretical introduction to this thesis. It discusses methods for synthesising nanoparticles (with particular emphasis on silver nanowires), physical phenomena occurring during the growth of nanocrystals, as well as chemical modification of nanoparticle surfaces. The next part describes the interaction of nanoparticles and fluorophores with light, a comprehension of which is crucial for understanding interactions between nanoparticles and fluorophores. The summary includes a literature review containing key research findings regarding fluorescence enhancement by nanoparticles and surface plasmon polariton (SPP) damping. These results focus on the fluorescence enhancement of various types of molecules by AgNWs and characterisation of surface plasmon polariton modes depending on morphology.

The second chapter describes the materials and experimental techniques used. It includes a description of the main experimental techniques used in the study: wide-field fluorescence microscopy, confocal fluorescence microscopy, time-resolved spectroscopy, scanning electron microscopy, spectrofluorimetry, and UV-Vis spectroscopy. Schemes of the optical microscopes used along with technical details are presented. The chapter concludes with descriptions of numerical methods - finite element simulations used to simulate the interaction of silver nanowires with light implemented in the COMSOL software.

The third chapter presents the results of the study. The hydrothermal method for synthesising silver nanowires with different morphologies is described first. The optical properties of silver nanowires were investigated in two configurations: 1) polymer matrix with photoactive PCP protein and 2) PCP monolayer covering the nanowires. Both experimental and numerical techniques were used to investigate fluorescence enhancement by silver nanowires and damping of surface plasmon polariton propagation. The last part demonstrates the method of coating the tip of a silver nanowire with PCP and proves that nanowires obtained through the synthesis described in this work can be used to excite molecules located 100 µm away from the laser focused on the nanowire end. The final chapter of the thesis summarizes the results.

Chapter 1

Review of Literature

1.1 Synthesis and chemistry of nanoparticles

Nanotechnology is a rapidly developing area of science. Most people credit its beginning to the lecture of R.P. Feynman "There's Plenty of Room at the Bottom"[1]. Usually, nanoparticles (NPs) are described as materials for which at least one dimension is smaller than 100 nm[2]. Nanoparticles are widely used in research as their physicochemical properties strongly depend on their size, shape, and composition. For example, water dispersions of 20 nm spherical nanoparticles of gold (Au), platinum (Pt), silver (Ag), and palladium (Pd) have characteristic colors, respectively: red, yellow-gray, black, and dark-black. As shown in Figure 1.1, a change in the morphology or composition of nanoparticles, results in a change of absorption spectra and, thus, a change in the visible color, which finds application in multiple areas of research i.e. in bioimaging[3].

Figure 1.1: Photographs of AuNPs dispersions. In each solution AuNPs vary in morphologies, which results in variations in color of their dispersions[3].

1.1.1 Methods of synthesis of nanoparticles

Up to these days, numerous methods of NPs synthesis have been described in literature, which naturally leads to multiple ways of grouping them. However, the most convenient one is based on the dimensions of the initial substrate. If the substrate is bigger than the final product, so during the synthesis, particles are downscaled, then

this method is called Top-Down. On the other hand, if the initial substrate is smaller than the product, it's called Bottom-Up synthesis[4]. The most common methods of NPs synthesis grouped into two main branches are shown in Figure 1.2.

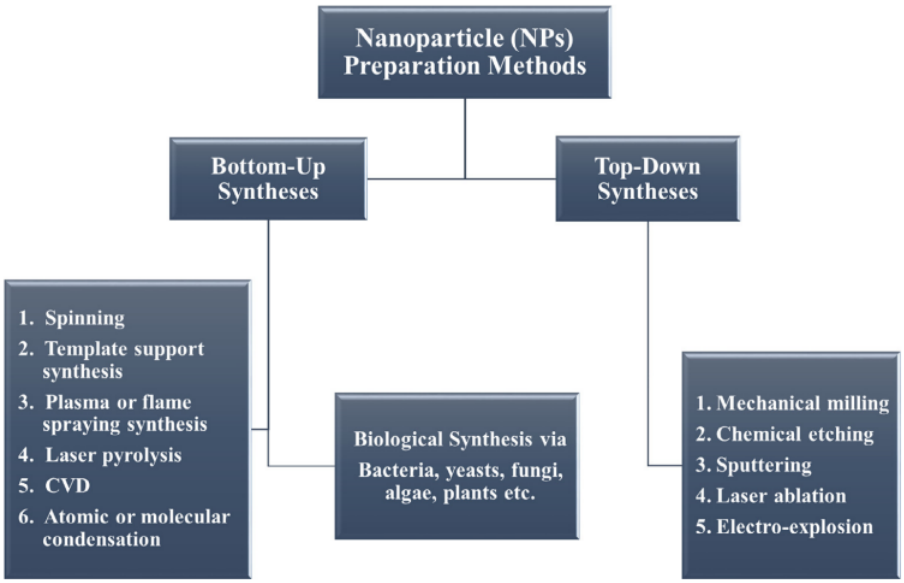

Figure 1.2: Scheme of methods of nanoparticles synthesis and corresponding commonly used techniques[4].

Top-Down

It is a method based on the fragmentation of a larger chunk of material. In mechanical milling and chemical etching surface of big particles is slowly degraded, reducing the size of particle itself. In sputtering due to bombarding with high energy particles a target, microscopic particles of material are ejected from target into substrate, forming new particles on its surface. In laser ablation process nanoparticles are created by removing material from a solid surface by irradiating it with a laser beam. Although these techniques are inexpensive and technically uncomplicated, their main drawback is a lack of shape control. Thus these methods are mainly applied to produce spherical NPs[5] quantum dots (QDs)[6] or exfoliated graphene[7].

Bottom-Up

In this approach, NPs are created from simple chemical compounds like inorganic salts subjected to the chemical reduction process. In that way, nanoparticles have fewer defects in their structure compared to Top-Down approach. At the same time, it is easier to control the dimensions of the nanostructures. Dimensions control is

the main reason why the Bottom-up approach is more frequently used than the Top-down. Moreover, based on the nature of the process, they are further categorized into subgroups: chemical methods, which often involve sedimentation and reduction and physical methods, where the two most commonly used techniques are chemical vapor deposition (CVD) and physical vapor deposition (PVD).

Thus, the Bottom-Up approach is utilized to obtain nanoparticles with complicated shapes (i.e. nanowires, which are the main focus of this thesis). The final shape of the nanoparticles is determined by conditions during the crystal's growth. In this thesis, the NPs were obtained only by chemical methods. Thus, further discussion will focus only on the mechanisms occurring in chemical synthesis, with particular emphasis on the synthesis of silver nanowires (AgNWs).

1.1.2 Nanocrystals growth

Although mechanisms of chemical reactions leading to nanocrystals growth are uncomplicated[8], explicit rules governing crystal growth are still unknown or unclear. Yet, three main stages of crystal growth can be defined:

1. nucleation,
2. evolution of nuclei into seeds,
3. growth of seeds into nanocrystals.

In a typical chemical synthesis in a solution, a chemical precursor is decomposed or reduced to achieve atoms on 0 oxidation state - main the building of metallic crystals. Upon precursor decomposition, the concentration of atoms steadily grows up, reaching a critical point. At this moment, nuclei start to form. In typical synthesis if any impurities are present, the atoms will form crystals on their surface. Thus to achieve homogeneous crystals high purity materials have to be used, to reach critical concentration of 0 oxidation state atoms to form homogeneous nuclei. In impurity free solution after formation of nuclei, they grow very rapidly, leading to a decrease in atom concentration in the solution. If atom concentration drops significantly, then no new nuclei are created. At this moment, atoms in a solution are in thermodynamical equilibrium with atoms at the surface of crystals. If the precursor is still decomposed, additional atoms start to appear on the crystal's surface, inducing the crystal's growth[8]. All these processes were described by LaMer[9]. Figure 1.3 presents atom concentration in the solution plotted against time, the horizontal lines represents distinctive atom concentration that occur during the process.

When the nuclei reach their critical size, fluctuation of the structure is no longer possible; at this point, they are called seeds. Seeds are defined as objects bigger than nuclei, but energy barriers do not allow for fluctuations in their structures. It is commonly accepted that the nanoparticle's final shape depends on the seed's crystal structure and chemical affinity to surfactants. All these are true for at least metals

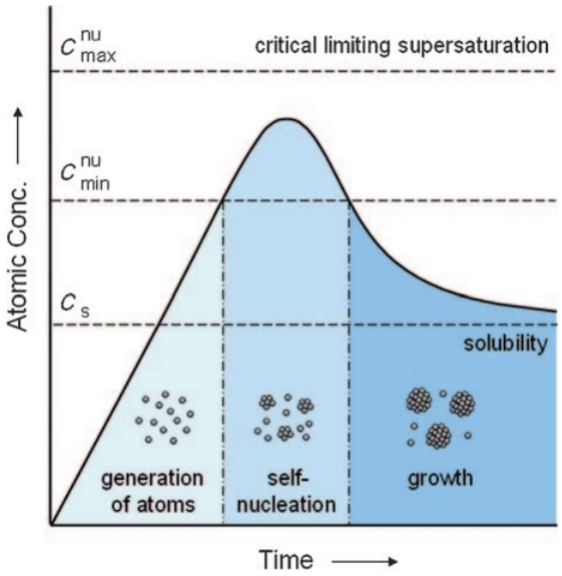

Figure 1.3: Atom concentration against time, during chemical precursor decomposition. At the beginning concentration steadily grows up to a critical point, once reached crystals start to nucleate, and atom concentration decrease reaching thermodynamic equilibrium. The atom concentration in the solution in the thermodynamic equilibrium with crystals surface has been marked as c_s, minimal concentration to begin nucleation as c^{nu}_{min} and maximum concentration without start of the nucleation as c^{nu}_{max}. Actual nucleation begins at the maximum of atom concentration against time[8].

such as Ag[10], Au[11], Pd[12], as shown in Figure 1.4. From this point of growth, the crystal maintains the initial structure (symmetry). Thermodynamically stable seeds exist as single, twinned, or multiply twinned crystals. The key to nanocrystal synthesis is to achieve the desired structure. The structure can be controlled by two factors:
- thermodynamical - every seed is trying to minimise its Gibbs free energy
- kinetical - every crystallographic plane has a different speed of atom addition.
The process is kinetically controlled if the process of nanocrystal growth is rapid and cannot reach thermodynamic equilibrium. On the other hand, if the process is relatively slow and the crystal can easily reach its thermodynamic equilibrium, then its thermodynamically controlled. This dependency is shown in protocols on nanoparticles synthesis: small crystals are obtained in rapid uncontrolled synthesis, while bigger crystals with nonspherical shapes are obtained in slow reactions with strictly controlled rate of atom generation.

Thermodynamical control

The thermodynamically controlled synthesis yields the products with the lowest Gibbs energy. One of the factors contributing to the total Gibbs energy is surface-free en-

Structures	Shapes	Schematic drawings	Metals
single-crystal	perfect/truncated cube[a]		Pd, Ag, Au, Pt, Cu, Rh, Bi, Fe
	perfect/truncated octahedron[a]		Pd, Ag, Au, Pt
	perfect/truncated tetrahedron[a]		Ag, Au, Pt, Rh
	rectangular bar		Pd, Ag, Pt
	octagonal rod		Pd, Au, Fe, Co, Ni
	rectangular or octagonal wire		Pb, In, Sn, Sb, Fe, Co
singly twinned	right bipyramid		Pd, Ag
	beam		Ag
multiply twinned	decahedron[a]		Pd, Ag, Au
	icosahedron[a]		Pd, Au
	five-fold twinned pentagonal rod		Pd, Ag, Au, Cu
	five-fold twinned pentagonal wire	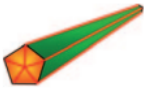	Ag, Au, Cu
	triangular/hexagonal plate		Pd, Ag, Au, Cu, Pb, Bi, Co, Ni
	disc		Sn, Co

[a] Platonic solid.

Figure 1.4: Scheme of nanoparticles shapes based on their initial structures and metals for which such synthesis has been described in the literature[8].

ergy. Wulff construction describes the most stable product by minimising surface-free energy for a given volume. The surface free energy (surface energy) γ is the energy required to create a new surface given by Equation 1.1, where G is the Gibbs free energy and A is the surface area[13].

$$\gamma = (\frac{\partial G}{\partial A})_{n,T,P} \tag{1.1}$$

For materials that crystallize in a face-centered cubic lattice (fcc) (like silver), the surface energy of facets can be lined up in increasing order: $\gamma_{111} < \gamma_{100} < \gamma_{110}$. Lowest energy single crystals that corresponding to these shapes have the shape of octahedrons, or tetrahedrons[8]. Nevertheless, the aforementioned shapes have a higher surface area than cubes with the same volume. As a result, seeds have to adopt the intermediate structure of truncated octahedrons to minimize surface energy. Such octahedrons have a close to spherical shape and {111} and {100} facets on the surface (Figure 1.5).

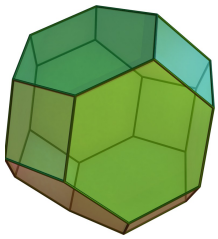

Figure 1.5: Truncated octahedron[14].

Two crystals can merge to minimize their surface energy, creating twinned crystals. Typical crystals are connected through {111} planes, which leads to defects and strains in their structure[15]. For multiple twinned crystals, the strains increase rapidly with increasing crystal size. For example, a five-fold twinned crystal consists of five tetrahedrons with a common edge. The angle between {111} planes is 70,53°. This means that to fully complete circle 360°-5*70,53°=7,35° must be compensated[8] by the increased distance between atoms at the crystals junction. As a result, only relatively small multiply twinned crystals are stable[16].

Kinetic control

When the seeds are relatively small (in the order of 1 nm), during their growth, the increase in surface energy can be compensated by the increased contribution of {111} facets on their surface. Nevertheless, theoretical calculations indicate that during rapid growth, low energy of {111} is insufficient to stop seeds' decomposition into monocrystals[17]. This analysis indicates that seeds have to be small to obtain multiply twinned crystals with good efficiency. It is usually achieved by a slow rate of atoms generation. When this condition is fulfilled, atoms crystallize in random hexagonal close-packing (rhcp) structures, which conserve defects in the crystal lattice[18].

These defects can result in thermodynamically unfavorable nanostructures, such as nanodiscs. In experiments, kinetic control is achieved by:

1. slow decomposition or reduction of chemical precursor[19],
2. using weak reducing agent[20],
3. combining reduction process with oxidation[21],
4. utilizing Ostwald ripening process[22].

Types of stable seeds and the following final crystal shapes have been shown in Figure 1.6[8].

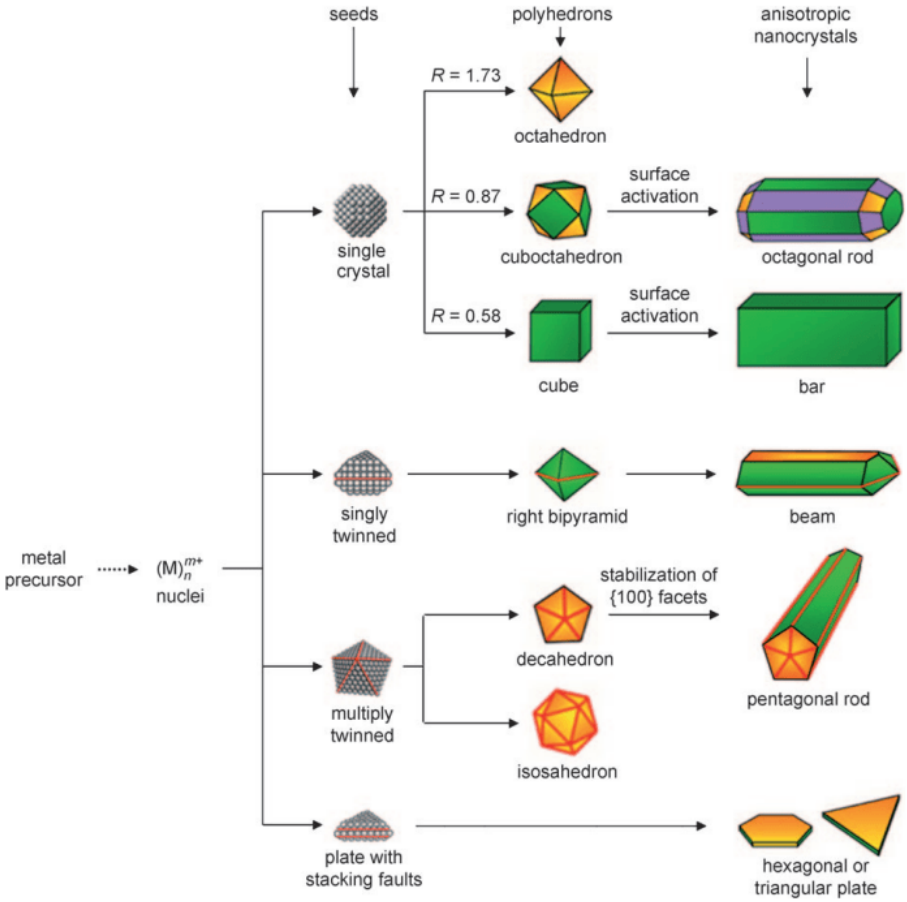

Figure 1.6: Growth routes for different types of seeds. The green, yellow and purple colors represent {100},{111} and {110} facets respectively. Twin planes are marked with red lines. Parameter R is defined as the growth ratio between <100>and <111>directions[8].

These rules apply to the synthesis of all types of nanoparticles. However, from this point, the discussion will focus on the only type of nanoparticles that is important from the point of view of this thesis: silver nanowires.

1.1.3 AgNWs synthesis

Silver nanowires (AgNWs) are one-dimensional silver nanostructures, typically with diameters ranging from 10 to 200 nm and lengths up to 100 μm[23]. A key distinguishing feature from nanorods is their aspect ratio, defined as the ratio of length to diameter, which must exceed 10[24]. In the last 30 years, many methods of AgNWs synthesis have been described. AgNWs can be obtained by physical and chemical methods. In chemical methods, two subgroups are present: hard template and soft template. Even though all methods may lead to high-quality nanowires, soft template methods are gaining more and more interest due to ease, high yield, low costs and low number of defects[24].

Physical methods of AgNWs synthesis

Physical methods are mainly based on lithography[25]. In lithography, in the first step, the mask determining the shape of the desired structure is deposited on a substrate. In the second step, the material is deposited onto the substrate. Finally, the mask is removed from the substrate. These methods give nanowires with strictly controlled dimensions. However, they have multiple drawbacks: the equipment utilised is expensive, and they require many optimisation steps to produce smooth nanowires with good plasmonic properties. Typically, they result in a stick-together agglomerate of nanoparticles, which has to be further processed(i.e. by elevating temperature), to achieve a structure similar to a monocrystal[26]. Thus, over the years, as advances in chemical synthesis were made, these methods became less and less popular.

Chemical methods of AgNWs synthesis

In chemical methods, silver nitrate is reduced to metallic silver. Basing on the nature of the template used to direct the growth of the crystals, one can distinguish two subgroups of the AgNWs synthesis:

- hard template in which template physically blocks crystal growth in the selected directions;
- soft template in which crystal growth is controlled by thermodynamics or kinetics of the process.

In hard template methods, cylindrical holes in materials (such as aluminium oxide membrane[27] or carbon nanotubes[28]) are used to direct nanowire growth. Nevertheless, following template removal is problematic, leading to additional defects in the AgNWs structure.

This problem has been overcome in soft template methods by introducing shape-directing agents. In these methods, water-soluble surfactants and polymers are used to direct crystal growth. The two most commonly used are: Cetrimonium bromide (CTAB)[29] and Polyvinylpyrrolidone (PVP)[30]. PVP is used more often because the resulting AgNWs have a better aspect ratio (length/diameter). The exact role of PVP in AgNWs growth is yet unknown. For many years, it has been suggested that differences in energy binding to different facets ({100} and {111}) are major factors[10]. However, the latest measurements suggest that thermodynamic differences are not sufficient and that kinetic effects play a main role[31]. It indicates that it is possible to change the dimensions of nanowires by regulating the kinetics of the process, i.e., by changing the reducing agent or temperature.

Furthermore, basing on the solvent used in the soft template AgNWs synthesis, two main methods are utilized:

- polyol - is a method where the reaction is conducted in ethylene glycol, which serves the role of solvent and reducing agent[30];
- hydrothermal - reaction is conducted in water environment in autoclave reactors in temperatures above 100°C[32] with the presence of an additional reducing agent.

Dimensions of AgNWs highly depend on reaction conditions in both methods, although the hydrothermal method usually gives longer AgNWs[25].

1.1.4 Influence of reaction parameters on AgNWs size

Mechanisms governing AgNWs formation are not yet fully understood. This subsection systematises information about the influence of the parameters on dimensions of AgNWs present in the literature. The most popular method of synthesis of AgNWs is a polyol; thus, most studies on the influence of parameters are described only for this method. It is impossible to conduct similar analysis for hydrothermal synthesis, due to lack of data in literature. However, it is anticipated that the hydrothermal and polyol methods should produce similar results.

Temperature and time influence

At room temperature, ethylene glycol does not act as a reducing agent. However, it oxidises to aldehyde at higher temperatures, which can reduce silver cations[33]. The equations for these reactions are presented in Figure 1.7. Temperature determines the reducing potential of ethylene glycol, and together with time, it's one of the most critical parameters in polyol synthesis. In polyol synthesis, the optimal reaction temperature was estimated to 160°C at 1 hour synthesis[35]. At 100°C no formation of AgNWs was observed[34], while at 185°C the main product was silver nanorods.

When cations acting as oxygen scavengers such as Fe^{3+} and Cu^{2+} were introduced into reactions, they facilitated the formation of AgNWs at 150°C[36]. Silver nanowires

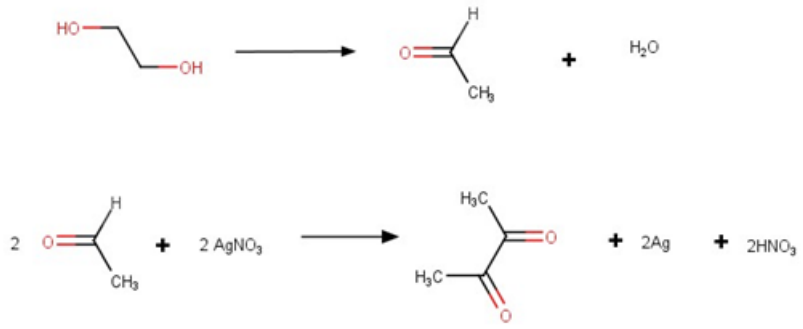

Figure 1.7: Reaction equation of ethylene glycol oxidation and silver nitrate reduction[34].

can be incorporated as conductive component into a polymer matrix to create a transparent and conductive macro-scale layer. The optical transparency and electrical conductivity of this layer are influenced by the dimensions of the AgNWs. This motivated studies of the influence of temperature on AgNWs' lengths and diameters. It was shown that with increasing temperature, nanowires tend to be shorter and have smaller diameters[37]. On the contrary, some studies show that with increasing temperature, the nanowires obtained are longer and have smaller diameter[38].

Polyvinylpyrrolidone

Nowadays, polyvinylpyrrolidone (PVP) is the most widely used crystal growth directing agent[8]. It is postulated that not the raw concentration of PVP has the major influence on crystal growth, but rather its ratio to Ag^+ concentration. For efficient AgNWs synthesis PVP:Ag^+ ratio should be around 1.5:1 at 1 hour at 160°C. While higher PVP:Ag ratios were used, nanorods become the predominant product. Conversely, at lower Ag:PVP ratios , nanowires are still formed but are shorter and have smaller diameters compared to those produced at the optimal ratio[35]. Studies on the influence of PVP molecular weight revealed that only nanoparticles with irregular shapes are obtained in monomer syntheses (1-ethylpyrrolidone). When the polymer contains 90 mers, synthesis results in nanoparticles with nanorod-like shape. When the polymer consists of at least 300 mers (molecular weight greater than 30 kDa), then the final product is mainly AgNWs. Additional studies have shown that the mixture of PVP with different molecular weights might result in longer and thinner nanowires[39]. As an example at 140°C using mixture of PVP360000+PVP55000 at ratio 1:1 nanowires have a diameter of 29.5 nm and a length of 29.2 µm. When the ratio is adjusted to 2:1, the diameter decreases to 24.8 nm, while the length increases to 34.8 µm. Nanowires obtained in syntheses with varying PVP molecular weigth are presented in Figure 1.8.

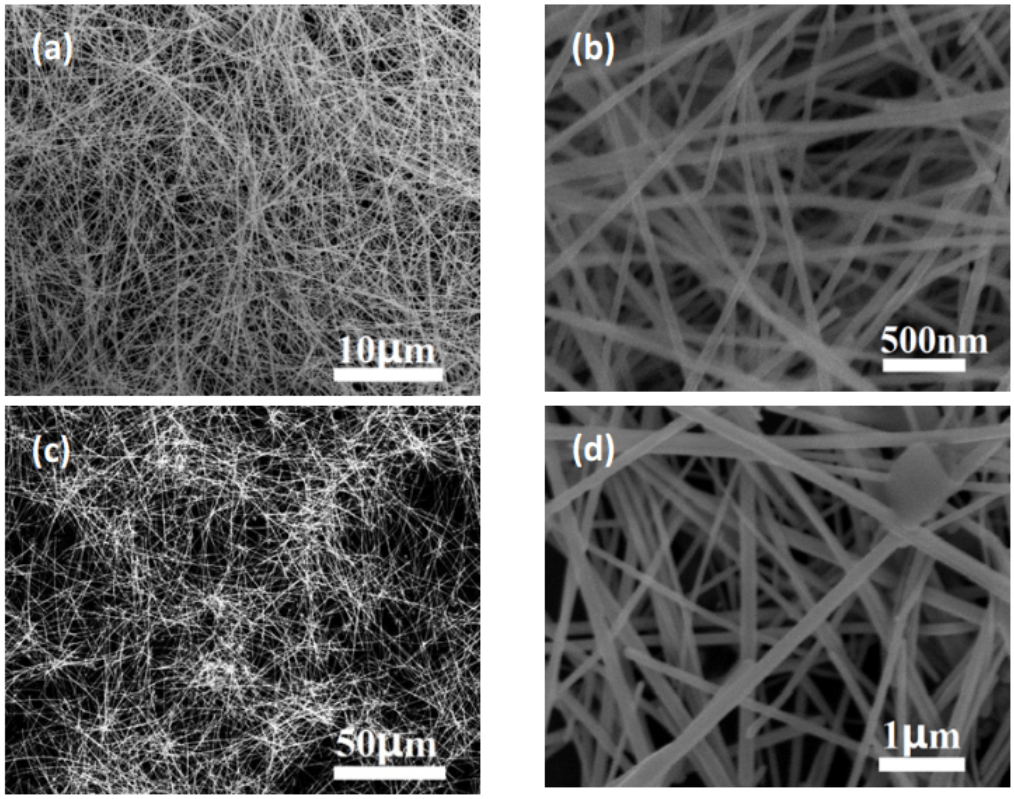

Figure 1.8: SEM images of AgNWs synthesized with (a,b) PVP-360000+PVP-55000 and (c,d) PVP-1300000+PVP-55000. Polymers with various chain lengths used in synthesis result in nanowires with different dimensions[39].

$AgNO_3$ concentration

The concentration of silver nitrate ($AgNO_3$) significantly impacts both the dimensions and the yield of silver nanowires in each synthesis. According to LaMer theory, maintaining a relatively low $AgNO_3$ concentration is critical to favor crystal growth over the nucleation of new seeds. Experimental results confirm that one of the most effective strategies to produce high-efficiency nanowires with a high length-to-diameter ratio involves maintaining a low and constant $AgNO_3$ concentration throughout the synthesis. This is achieved through the controlled and gradual addition of 0.1 M $AgNO_3$ solution using a syringe pump. The syringe pump plays a vital role in this process by delivering the $AgNO_3$ solution at a precisely regulated flow rate[35][34]. Literature reports tried to achieve more efficient (higher number) AgNWs synthesis. One of the attempts was made to increase $AgNO_3$ concentration to the range of 0.1-0.6 M. Nevertheless, it resulted in short nanowires (8 µm) with a very large diameter (300 nm)[40]. These experiments also revealed that the volume of the reactions itself might influence AgNWs dimensions.

Influence of chloride anions and other substances

Chloride anions are another chemical species that have a critical influence on the shapes of silver nanoparticles[41]. Their absence in synthesis results in nanoparticles with irregular shape, and even a trace amount of chlorides influences the shape of the seeds and the final product - silver nanowires[33][41][42]. They adsorb at the seed surface, blocking the aggregation of nanoparticles[43]. In water solutions, chloride anions, upon contact with silver cations, form insoluble silver chloride. The process of silver chloride formation decreases Ag^+ concentration so that it can substitute a slow injection into the solution with a syringe pump. Studies have also shown that silver can nucleate on the surface of cubic crystals of silver chloride, so it acts as initiators of nucleation[44][45]. Bromide anions can substitute chlorides; usually, they are introduced into the solution in the form of CTAB or KBr. When bromide anions were used instead of chloride in the syntheses, the nanowires obtained had smaller diameters[46][47]. Studies show that factors such as mixing speed or shape of magnetic stirrer affect the final dimensions of AgNWs, but these studies were not carried out systematically[23].

Influence of reaction parameters in the hydrothermal synthesis

Hydrothermal synthesis of AgNWs is relatively novel, and as a consequence, its description in the literature is not as exhaustive as for polyol synthesis. Publications focus mainly on the influence of different reducing agents such as: glucose[32][48], and sodium citrate[49]. There are no extensive studies on the influence of other parameters, such as temperature or PVP chain length. Although the data is fairly limited, few trends can be spotted. Usually, the temperature oscillates around 160 ° C, the reducing agents are described as mild with redox potential around -0.5 V , the PVP concentration is much higher than $AgNO_3$, and chloride anions are always present. The aforementioned data were the starting point for the research in this thesis.

1.1.5 Chemical modification of nanoparticles surface

Silver surface chemistry is not rich in chemical reactions. Adsorption might seem like a plausible method for the surface modification of silver nanoparticles. It is a straightforward single-step approach, and nanoparticles have a high surface area, at which chemical compounds can adsorb. However, it is a spontaneous, reversible, and dynamic process. Adsorbed proteins are bound to the surface via weak intermolecular forces, namely, ionic bonds and hydrophobic or polar interactions. Thus physisorbed proteins may easily detach from the surface during measurement[50]. Therefore, proteins are often immobilised onto the surface by covalent bonds formed between protein and molecules at the nanoparticle's surface. Molecules of interest are introduced during synthesis impacting nanoparticles growth (e.g., citrates[51], polyethylene glycol[52]) or afterwards. Surface modification of silver after synthesis is usually conducted with short-chain length molecules with functional groups

at both ends. On one end is the thiol (-SH) group which strongly binds to the surface of the silver, forming a self-organising monolayer, on the another end is functional group such as amine (-NH_2) or carboxylic (-COOH)[53]. Molecules with short aliphatic chains are preferred as such modified nanoparticles have a higher water solubility. The amine and carboxylic groups can further react, creating a peptide bond, which can be utilized to binding various molecules, i.e. proteins.

In the side chains of proteins exist multiple chemical moieties with various chemical groups. When so many chemically reactive groups are present it often leads to unwanted reactions between the proteins. The most popular functional groups present in the side chain of the proteins and their relative groups at the surface of the nanoparticles, with which they can react, are presented in table 1.1[54].

Side groups	Amino acids	Surface funcionality
-NH_2	Lysine	carboxylic acid active ester (NHS) epoxy aldehyde
-COOH	Aspartic acid, glutamic acid	amine
-SH	cysteine	maleimide vinyl sulfone pirydyl disulfide
-OH	serine, tyrosine	epoxy
Streptavidin/Avidin	-	biotin
His Tag	-	Ni^{2+}

Table 1.1: Functional groups in side chains of proteins and functional groups utilized to bind them to the surface of nanoparticles[54].

Coupling between amine and carboxyl moieties is most widely used in protein binding. Nevertheless, this reaction has nearly zero value of enthalpy (≈-3,6 kJ/mol[55]) and thus maximal yields of about 50%. Moreover, to induce the reaction, a catalyst has to be used. To overcome these thermodynamical and kinetic problems, carboxyl-reactive crosslinkers are used. Carbodiimide compounds such as 1-ethyl-3- (3-dimethylaminopropyl) carbodiimide hydrochloride (EDC) are commonly used. EDC reacts with carboxyl groups which can react further with primary amines. Such EDC-activated carboxyl undergoes hydrolysis in water; thus, these compounds are unstable in water solutions. Therefore in most cases, carboxyls are coupled with N-hydroxysuccinimide (NHS), forming NHS ester, which is more stable and can react with primary amines at physiological pH (around 7.4). Other widely used surface attachment strategies utilise thiol groups from cysteine residues to maleimide activated, iodoacetyl modified, or metallic surfaces[56][57][58].

The covalent bonding of proteins is robust and quite simple. However, this approach suffers from a random and nonselective place of binding, which affects the protein properties. Another surface immobilization is based on the biochemical affin-

ity reactions[59]. Biotin-avidin/streptavidin interaction is an example of such an approach. It is one of the strongest known non-covalent bonds (≈-100kJ/mol[60][61]), with a strength comparable to weak covalent bonds. In this method, proteins must be conjugated with either biotin or streptavidin[62]. Another standard method of protein immobilisation is the interaction of hexahistidine-tagged (His-tag) proteins with Ni^{2+}[63]. In this procedure, nitrilotriacetic acid is usually bound to the sensors' surface. In the next step, three carbonyl groups form a complex bond with the Ni^{2+} cation, and three histidine bind to the nickel cation, fulfilling its coordination sphere. This procedure has the advantage of surface regeneration. Nickel with bound protein can be removed from the surface by strong metal chelation agents such as ethylenediaminetetracetic acid (EDTA)[64][65].

1.2 Interactions of light with nanoparticles and fluorophores

1.2.1 Surface plasmon resonance

Due to the high ratio of surface area to volume, metallic nanoparticles exhibit properties not observed in bulk materials. One notable occur upon interaction with light. When a nanoparticle is illuminated by an electromagnetic wave, localized surface plasmon resonance (LSPR) is excited. LSPR occurs when the conduction electrons on the surface of metallic nanoparticles collectively oscillate in resonance with the incident electromagnetic field. This phenomenon arises in nanoparticles that are much smaller than the wavelength of the incident light.

The interaction with the electromagnetic wave leads to the coherent oscillation of free electrons, which is confined to the nanoparticle's surface. This creates a strong localized electromagnetic field near the nanoparticle, significantly enhancing optical phenomena such as absorption and scattering. Additionally, LSPR is highly sensitive to the nanoparticle's size, shape, composition, and surrounding environment. The process is schematically illustrated in Figure 1.9[66].

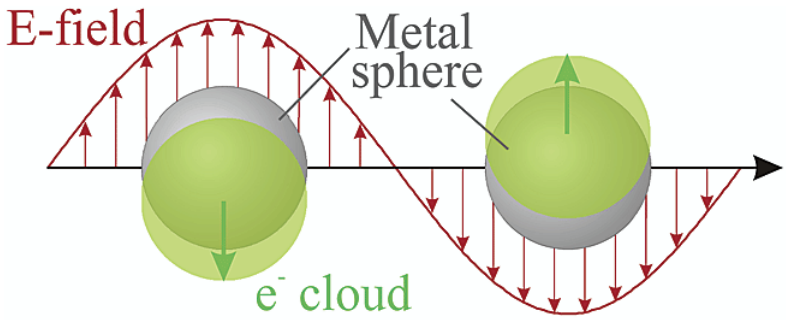

Figure 1.9: Schematic of electrons oscillation in a metallic sphere upon illumination. When the electric field is applied, the electron cloud is displaced relative to the nuclei. Oscillations of electric field result in oscillations of electron cloud[66].

Gustav Mie provided the first mathematical description of light scattering, and absorption for spherical nanoparticles in 1908[67][68]. For light-matter interactions, the metallic nanoparticle can be treated as a core consisting of packed positively charged atomic cores and negatively charged electrons moving freely in their volume. Upon illumination (application of electric field), electrons, that do not contribute to chemical bonds, start to move to the nanoparticle's surface. Then, they return to their previous state due to Coulomb's attraction. Electrons are confined inside the nanoparticles; thus, when a negative charge accumulates on one side, then a positive charge accumulates on the other side of the nanoparticle. This induced dipole generates an electric field opposite to the incident electric field, forcing electrons to oscillate. The electrons oscillation frequency, known as plasma frequency, is determined by the properties of the system and environment (electron density, di-

electric constant of the medium, etc.). Increased electric field intensity in the vicinity of the nanoparticle results from electron acceleration and is known as the antenna effect[69]. Localized surface plasmon resonance is a well-known and widely used phenomenon; thus, it is well described theoretically and experimentally[70]. Surface plasmons have been used to enhance the surface sensitivity of several types of spectroscopic measurements including fluorescence, Raman scattering, and second-harmonic generation[71][72].

1.2.2 Surface Plasmon Polaritons

If one of the dimensions of the nanoparticle far exceeds the wavelength of the incident light, in that case, electron oscillations are no longer confined in space and can travel along the nanoparticle in the form of Surface Plasmon Polaritons (SPP)[70]. The electric field intensity of SPP is shown in Figure 1.10. Such waves traveling along

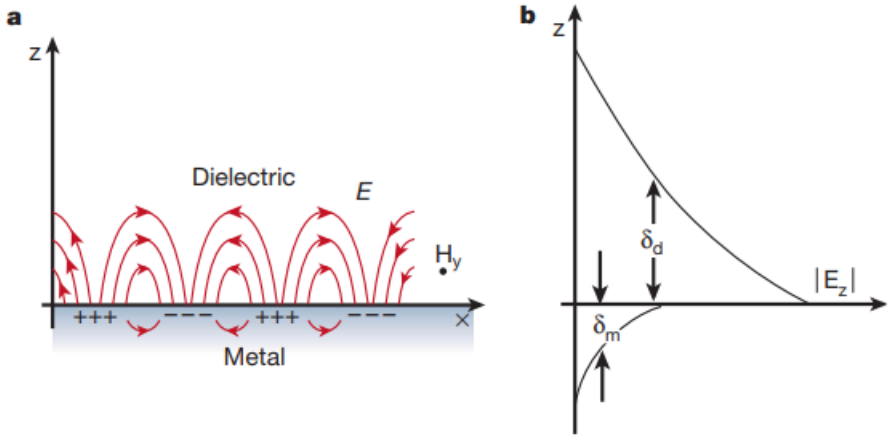

Figure 1.10: Schematic representation of SPP at the boundary of metal and dielectric (a) the electric field is perpendicular to the surface, and the magnetic field is transverse. (b) the z component of the electric field is evanescent in both media, δ_d is a decay length into dielectric usually is of the order of half wavelength, δ_m is a decay length into the metal of the order of tens of nanometers[73].

the boundary of metal and dielectric are described by Maxwell equations. The electric field of SPP that propagates along the boundary of metal and dielectric altogether with induced charges and electric field intensity near the boundary is characterized by two values: 1) δ_d the distance in the dielectric at which the electric field intensity reaches 1/e of its maximum value and 2) δ_m the distance in the metal at which the electric field intensity reaches 1/e of its maximum value. Typically $\delta_d > \delta_m$ due to stronger damping of the electric field in metals than in dielectrics. Compared to localised plasmon resonance, Surface Plasmon Polaritons can transport energy over micrometre distances[74].

1.2.3 Interactions of nanoparticles and fluorophores

Metallic nanoparticles during light illumination act as antenna concentrating electromagnetic field. The presence of a nanoparticle affects fluorophores in its vicinity, which leads to two effects:

- fluorescence quenching - when a fluorophore is directly in contact or very close vicinity of a nanoparticle, then most of the energy is transferred to the metal and then dissipated as a heat,
- fluorescence enhancement - increased excitation probability due to higher strength of the electric field and increased probability of radiative decay[75].

Interactions of single fluorophores with light have been shown in the simplified Jabłoński diagram in Figure 1.11. All three main processes of light-matter interactions have

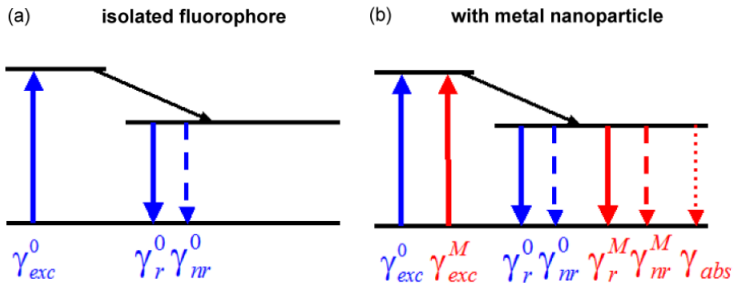

Figure 1.11: Simplified Jabłoński diagram. (a) An isolated fluorophore is characterised by three quantities: excitation rate (γ^0_{exc}), radiative rate (γ^0_r), and nonradiative rate (γ^0_{nr}). Fluorophore-plasmons interactions modify all of them (γ^M_{exc}, γ^M_r and γ^M_{nr}) but also allow for additional process in which energy is transferred from the fluorophore to the metal γ_{abs}[76] .

been marked: excitation (rate γ^0_{exc}), radiative decay (rate γ^0_r), and non-radiative decay (rate γ^0_{nr}). In a free-space quantum yield (Q_0) and excited state lifetime (τ_0) is defined by[77]:

$$Q_0 = \frac{\gamma^0_r}{\gamma^0_r + \gamma^0_{nr}} \tag{1.2}$$

$$\tau_0 = \frac{1}{\gamma^0_r + \gamma^0_{nr}} \tag{1.3}$$

On the other hand, when the fluorophore is placed in the vicinity of the nanoparticle, interactions between the electronic states of the fluorophore and nanoparticle introduce additional channels (γ^M_{exc}, γ^M_r and γ^M_{nr}). Then quantum yield and excited state lifetime are defined as[78]:

$$Q_M = \frac{\gamma^0_r + \gamma^M_r}{\gamma^0_r + \gamma^M_r + \gamma^0_{nr} + \gamma^M_{nr}} \tag{1.4}$$

$$\tau_M = \frac{1}{\gamma_r^0 + \gamma_r^M + \gamma_{nr}^0 + \gamma_{nr}^M} \tag{1.5}$$

Interactions between the fluorophore and electronic states of nanoparticle can be observed experimentally in the change in fluorescence signal intensity or fluorescence lifetime as shown in Figure 1.12. Radiationless energy transfer from fluorophore

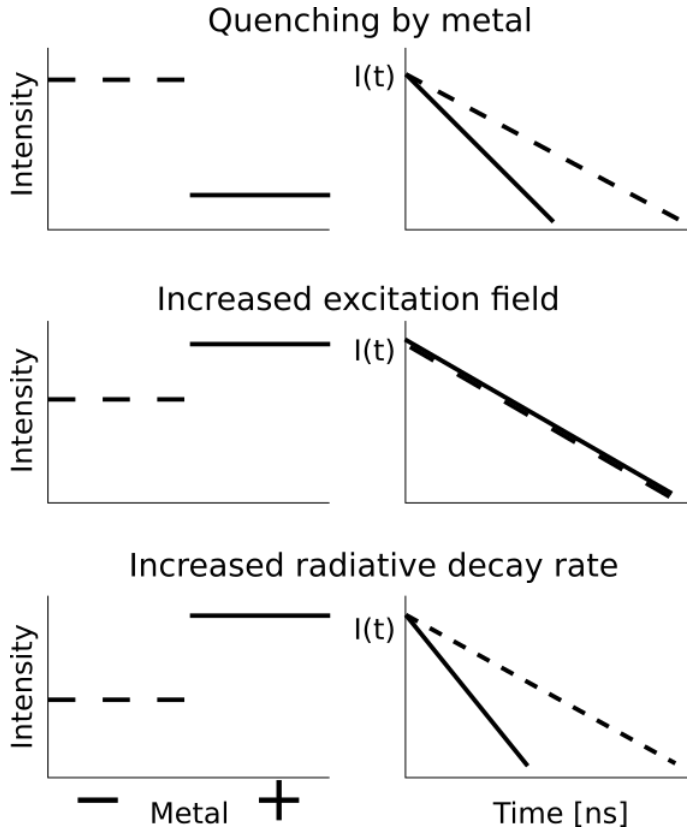

Figure 1.12: Effects of fluorophore-metal interactions on measured intensity and fluorescence lifetime. The dashed lines indicate the absence of the metal, and the solid line indicates the presence of the metal. Recreated from[79].

(Quenching) into metal results in decreased fluorescence intensity and shortening of the excited state lifetime. The enhanced electric field around the nanoparticle results in an increased absorption due to a stronger electric field, not affecting the fluorescence lifetime. While the increased probability of emission results in increased emission intensity and shortening of the excited-state lifetime. In typical physical systems, usually all three effects are observed.

Two conditions must be fulfilled to observe fluorescence emission enhancement: fluorophore and nanoparticle must be placed at a certain distance, and absorption or emission band of fluorophore must match the scattering spectrum of nanoparticle[77].

Experiments conducted in group lead by prof. Novotny perfectly display the processes described above[80]. In these experiments, 80 nm gold nanoparticle was placed at the edge of the AFM (Atomic Force Microscope) cantilever. They observed differences in fluorescence intensity by varying the distance between the nanoparticle and a single fluorophore (nile blue). When the nanoparticle approached fluorophore, they observed increase of fluorescence intensity. Upon reaching the critical distance (5 nm), they observed reversed effect (fluorescence quenching). This experiment proves that varying distance between fluorophore and nanoparticles induces transition between processes influencing fluorophores brightness. Figure 1.13 shows experimental setup to observe this phenomenon and measured fluorescence intensity of the fluorophore.

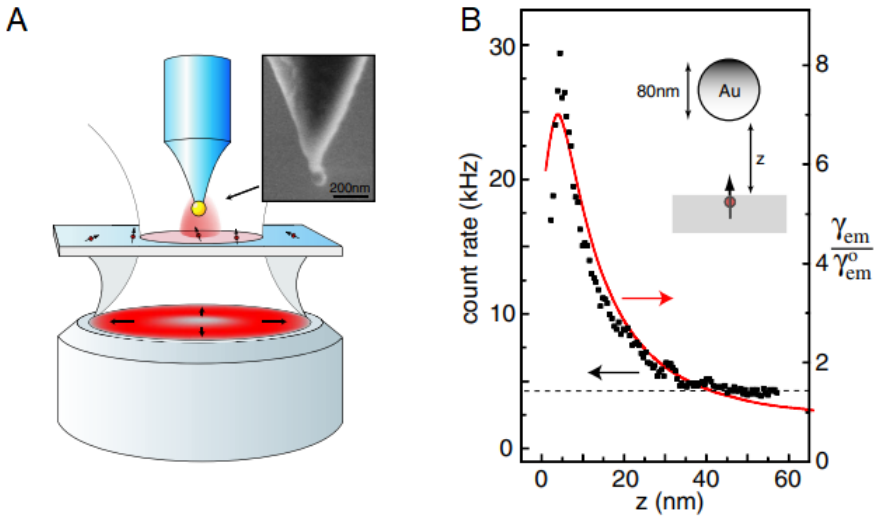

Figure 1.13: Experiment investigating fluorescence intensity as a function of the distance between fluorophore and nanoparticle.(A) Experimental setup consisting of a metallic nanoparticle mounted on AFM tip and investigated single fluorophore mounted on a fluorescence microscope, (B) fluorophore fluorescence intensity as a function of the distance between nanoparticle and fluorophore[80].

1.2.4 Metal-enhanced fluorescence with silver nanowires

The strength of interaction between emitters and silver nanowires depends mainly on the relationship between fluorophore excitation and emission characteristics to nanowire, plasmon resonance and the distance between the fluorophore and nanoparticle[81]. The latter can be controlled by chemically bonding fluorophores to the surface of nanoparticles via appropriate linkers[82][83], or alternatively thin dielectric layer containing fluorophores is deposited on nanowires. Such configurations are usually obtained by either mixing nanowires with polymer and fluorophores[84][85]

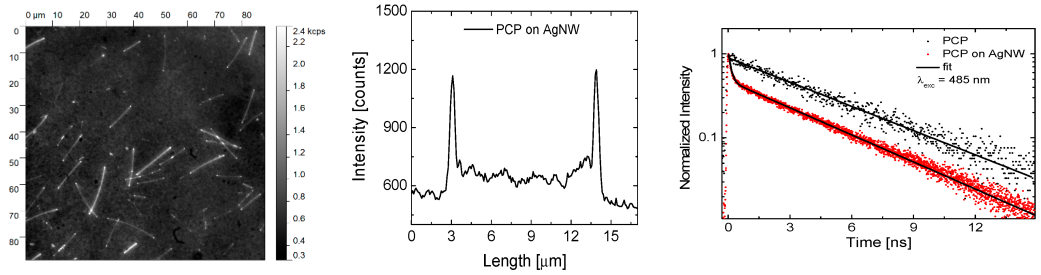

(a) (b) (c)

Figure 1.14: Results of fluorescence imaging and spectroscopy of planar structure consisting AgNWs and PCP: (a) fluorescence intensity map obtained by exciting sample with 405 nm wavelength, intensity cross section measured along the nanowire, (c) fluorescence decay curves obtained on nanowire (red) and off nanowire (black)[85].

or placing the polymer layer above the nanowires[86][87][85].

Planar Structures

The simplest hybrid nanostructure can be achieved by depositing a mixture of nanowires and emitters onto a substrate. In such a structure first example of coupling between electronic states in peridinin-chlorophyll-protein (PCP) (emitter) and silver nanowires was observed. The fluorescence imaging experiments of such nanostructure are displayed in Figure1.14. In the fluorescence intensity maps of such nanostructure (Figure 1.14a), bright elongated shapes appear which position correlates with the position of the AgNWs on the substrate, indicating enhanced emission of PCP in the vicinity of AgNWs. What is more interesting and cannot be straightforwardly deduced is that plasmonically enhanced fluorescence noticeably overcomes the contribution of PCP molecules which emission is quenched (those localised close to the silver nanowire) as well as those not coupled due to too big separation distance. The fluorescence enhancement can be measured more quantitatively by extracting fluorescence intensity along the nanowire (Figure 1.14b). For the 405 nm excitation wavelength, the fluorescence intensity on the nanowires is only 1.3 times bigger compared to the area of the nanowire. However, fluorescence intensity is 2.4 times higher at the ends of nanowires, indicating higher fluorescence intensity enhancement at these points.

In planar structures, separation distances range from very small values (a few nanometers), where quenching dominates, up to relatively big values (tens of nanometers), where no coupling is present. Therefore primarily qualitative information about interacions between AgNWs and fluorophores can be extracted, and another approach must be utilized to understand the phenomena with details. Such experiments can be carried out utilizing confocal microscopy, where the laser spot is focused up to a diffraction-limited area of the sample. This kind of microscopy allows

measurements of fluorescence emission spectra or fluorescence decays. The latter gives information about the coupling efficiency between emitters and nanostructures and provides hard evidence of the plasmonic origin of fluorescence enhancement. In Figure 1.14c, fluorescence decay curves of PCP molecules in the vicinity and far away from nanowires are presented. The PCP molecules deposited on the substrate fluorescence decay is monoexponential with a decay constant of about 4 ns. In contrast, decays for PCP on nanowires are shorter and bi-exponential. One of the decay components is similar to the previously measured (4 ns), and another one is substantially shorter (about 0.3 ns). Such shortening might indicate that the actual fluorescence enhancement for molecules coupled with silver nanowires can be up to tenfold[81].

Similar experiments for materials and compounds that can be potentially utilized in photovoltaics have also been conducted[88][89]. In such cases, nanowires may play a bimodal role, enhancing absorption and emission of compounds and providing a charge network while preserving high transparency[90][91]. In the following experiments, nanowires were embedded in conductive in a conducive polymer poly(3,4-ethylenedioxythiophene):poly(styrene-sulfonate) (PEDOT:PSS) layer, with a semiconducting polymer utilized in photovoltaics poly(3-hexylthiophene) (P3HT) layer deposited above the layer with nanowires. The layer of PEDOT:PSS had a thickness of 40 nm, and a layer of P3HT was about 30 nm thick. Results of these experiments are presented in Figure 1.15. The fluorescence intensity maps (Figure

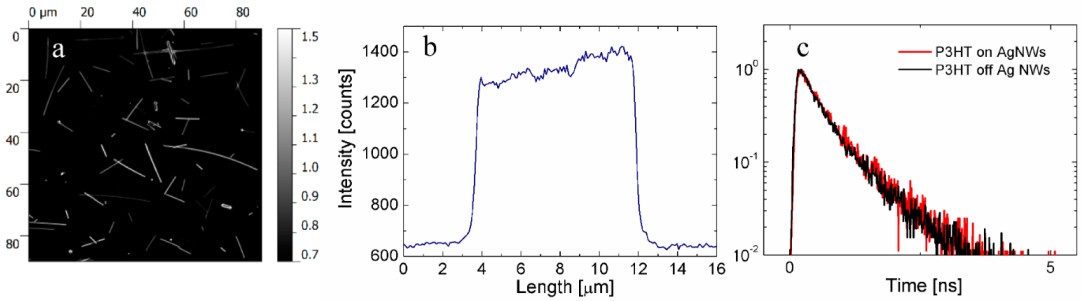

Figure 1.15: Results of fluorescence imaging and spectroscopy of P3HT deposited over AgNWs: (a) fluorescence intensity map obtained by exciting sample with 485 nm wavelength, intensity cross section measured along the nanowire, (c) fluorescence decay curves obtained on nanowire (red) and off nanowire (black)[81].

1.15a) and a cross-section along the nanowire (Figure 1.15b) suggests fluorescence enhancement higher than the above-discussed PVP structure. Indeed analysis of over 100 nanowires estimated the fluorescence enhancement factor to 2.1. However, the discrepancies between samples were acquiesced to discrepancies in fluorescence enahncement of both samples[92].

Time-resolved fluorescence spectroscopy leads to an explanation of the dominant process of the observed increase in fluorescence intensity, which might be in-

duced by an increase in absorption rate or radiative rate, or a combination of thereof. However, the fluorescence decays curves (Figure 1.15c) measured on nanowires and off nanowires are identical, which strongly suggests that this increase in fluorescence intensity is caused by increased excitation rate.

Bioconjugated Systems

The examples presented so far illustrate cases where the control over the morphology of hybrid structure was somewhat limited, especially in the distance between nanostructure and fluorophore. All these drawbacks are overcome when (bio)conjugation approach is utilized. In this way, the fluorophore is bound to the nanoparticle's surface through chemical bonds. Thus, the distance between elements of the hybrid nanostructure can be controlled by choosing appropriate building blocks. Moreover, it enables to creation monolayer of fluorophores. In bioconjugation, mainly proteins (such as PCP) are utilized, as they can be easily equipped with proper functional groups. The most common modification of protein is streptavidin which exhibits high binding affinity to biotin[93]. Therefore, to obtain bioconjugation in the system, it is required to functionalize nanoparticles with biotin. The formation of a hybrid nanostructure takes place in solution, where a bond between biotin-functionalized nanowires and PCP-streptavidin is formed. Then the solution containing conjugates can be deposited on a glass substrate, which allows studying the optical properties of the hybrid nanostructure. Wide-field fluorescence microscopy images of the prepared sample are presented in Figure 1.16. The fluorescence emission of PCP

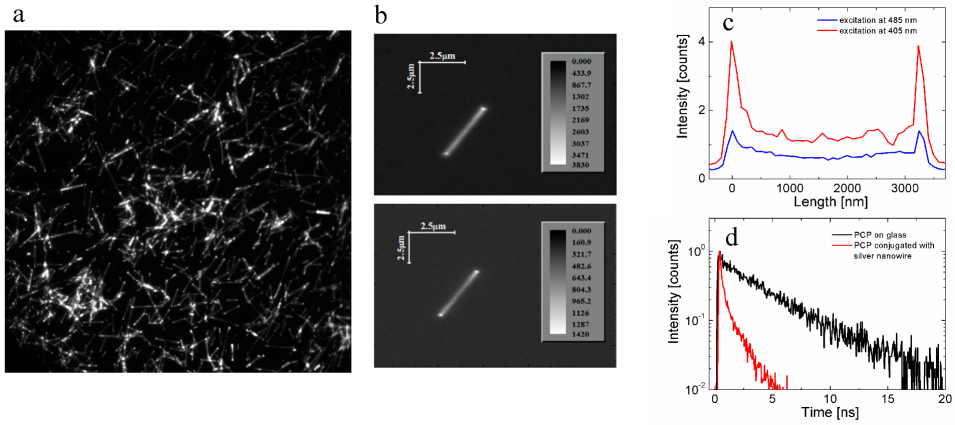

Figure 1.16: Wide-field fluorescence microscopy images of PCP conjugated with AgNWs: (a) fluorescence map excited at 485 nm, (b) the same nanowire excited at 405 nm (upper) and 480 (lower), (c) intensity cross-sections along the nanowire for both excitation wavelengths, (d) fluorescence decays curves measured on nanowire (red) and a layer of PCP on glass (black)[81].

molecules appears exactly at the locations of the nanowires, which demonstrates that

PCP attaches to the nanowires, and its fluorescence is not quenched. However, due to a lack of reference at this point, it cannot be concluded that the optical properties of PCP are affected by silver nanowires. As a consequence, another way of deduction has to be conducted. Anyway, if the coupling between PCP and nanowires exists, it should exhibit qualitatively as different responses to excitation wavelength compared to free PCP. This property is visualized in Figure 1.16b, where single nanowires excited at two wavelengths are presented. The first one corresponds to the maximum of plasmon resonance in silver nanowires (405 nm), and the latter is the maximum absorption of PCP (485 nm). For free PCP, maximum fluorescence intensity should appear at 485 nm excitation. Yet on the result displayed in Figure 1.16b maximum fluorescence intensity is measured for 405 nm excitation. This is further seen in cross-sections along the nanowires, where emission for 485 nm is two times higher than for 405 nm. Such results demonstrate that coupling between the fluorophore's electronic states and metallic nanowires occurs.

One can measure fluorescence dynamics to further quantify the effects of plasmons excitations. Results of such experiments for PCP conjugated with nanowires are presented in Figure 1.16d. When comparing fluorescence decay for conjugated sample and reference, shortening in the first case is observed. Moreover, both curves are qualitatively different as no long decay component is present.

Silver nanowires provide a high potential for sensing due to the high density of functional groups, direct visualisation with optical systems, and metal-enhanced fluorescence. Moreover, they provide the ability to monitor the binding of proteins in real-time[94]. The universality of bioconjugated hybrid nanostructures could also be the extent to other commonly utilized emitters such as semiconductor quantum dots[95][93].

1.2.5 Plasmonic waveguides

Optical fibres are extensively utilized in optical communication systems. However, the diffraction limit imposes constraints on the smallest possible size of dielectric waveguides below lenngth of operating wavelength. Interestingly, metal nanostructures can sustain surface plasmon polaritons (SPPs), which are collective oscillations occurring at the metal-dielectric interface. These oscillations enable light to be guided over micrometer-scale distances. SPP light confinement is much greater than in a typical dielectric waveguide resulting in a stronger electric field at the subwavelength scale. To direct light propagation, one-dimensional (1D) waveguide structures are used. 1D plasmonic waveguides can be realized in many geometries as metal nanowires[96][97], stripes[98][99], grooves or slots in metal film[100][101] or dielectrics deposited on metal films[102][103]. Although all noble metals can be used as materials for NWs, silver is the preferred one. Due to the dielectric constant of silver and thus plasma resonance frequency, which provide the best waveguiding properties[104] in the optical range. The comparison of dielectric constants of metals and calculated SPP lengths of infinite flat surfaces are presented in Figure 1.17. Due to the main focus of this thesis, the analysis below is carried with particular emphasis on silver nanowires. However, most of the described phenomena are true for all kinds of metallic nanowires.

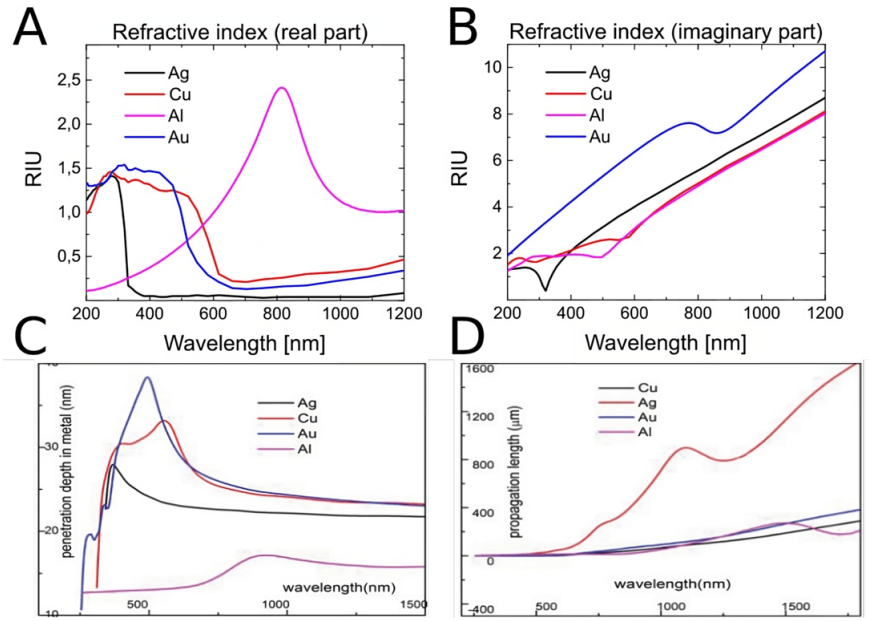

Figure 1.17: (A)Real and (B)imaginary part of the dielectric constant of silver (data taken from [105])and (C)corresponding penetration depths in metal and (D)SPP propagation length calculated for an infinite flat boundary between metal and vacuum[106].

General properties of SPP in metal nanowires

A metal NW can be treated as a quasi-one-dimensional structure with translational symmetry (as a convention, it is assumed they are infinite in the z-direction). Due to its the symmetry electric field distribution of the guiding modes can be expressed as: $E(r) = E(x,y)e^{i(k_\parallel z - \omega t)}$, and it gives a two-dimensional Helmholtz equation in the form[107]:

$$\nabla_\perp^2 E(x,y) = (k^2 - k_\parallel^2)E(x,y) \tag{1.6}$$

where $\nabla_\perp^2$ is the two-dimensional Laplace operator in the transverse plane, $k_\parallel$ is the wave number of the mode parallel to the NW, and k_i is defined as $k_i^2 = \epsilon_i \mu_i k_0^2$ in respective regions (ϵ_i is the permittivity of the material, μ_i is permeability and k_0 is the wave vector in the vacuum). The corresponding transverse wave vectors can be obtained from $k_{\perp,i}^2 = k_i^2 - k_\parallel^2$. This case is illustrated in Figure 1.18, where i = 1 is the core region and i = 2 is the cladding region. For guiding modes, $k_{\perp,i}$ are imaginary in both

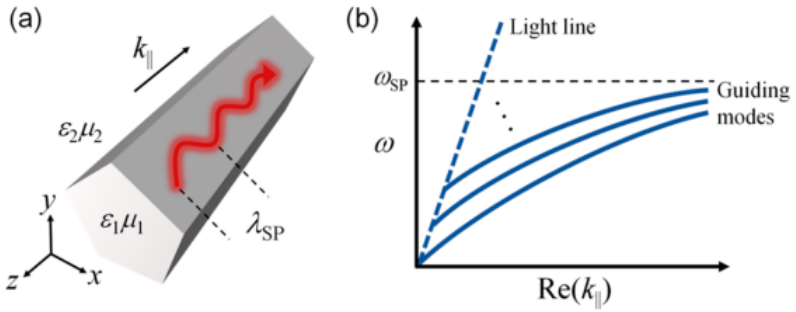

Figure 1.18: (a) Scheme of SPP propagating on metal NW. The core is a metallic pentagon with ϵ_1 and μ_1 and the cladding is an outer region with ϵ_2 and μ_2 (b) Dispersion relations of the SPP modes in a metal NW[107].

core and cladding, and $k_{\perp,i}^2 = k_i^2 - k_\parallel^2 < 0$. As a result, the fields decay exponentially on both sides of the metal-dielectric interface. However, in some configurations (for example, NW deposited on a substrate with the refractive index of n_s), $Re(k_\parallel)$ might be smaller than the wave vector of light in the cladding $Re(n_s k_0)$, and field in the substrate is no longer evanescent. This results in radiation leakage from plasmon mode (leaky modes) and additional damping factor during propagation[107].

In a typical dielectric waveguide, the wave vector inside the core is purely real, and the wave is not evanescent inside the core. The diffraction limit indicates that at some point, with decreasing size of the waveguide leads to more power extending outside the core region. This condition is not valid for plasmonic waveguides, where the electric field is highly confined in a metal-dielectric interface, accounting for strong light-matter interactions at the interface.

A thick NW can support several modes. These modes correspond to specific configurations of the electromagnetic field and charge distribution along the nanowire.

For chemically synthesised nanowires that are pentagonal, these modes are symmetric or antisymmetric in the x direction because of mirror symmetry. The real part of the wave vector parallel to propagation (and the nanowires itself) is determined by the wavelength of the plasmon modes $Re(k_\parallel) = 2\pi/\lambda_{SPP}$. An effective refractive index of the plasmon mode is defined as $n_{eff} = Re(k_\parallel)/k_0$. In similarity to the refractive index of the medium, it also describes the change of the wavelength, $n_{eff} = \lambda_0/\lambda_{SPP}$. n_{eff} and $k_\parallel$ depend on the frequency, and their dispersion relations are presented in Figure 1.18. Larger n_{eff} is associated with higher confinement and thus more field distributed inside the metal region leading to higher damping due to Ohmic losses. Two factors determine dispersion relations: material dispersion and geometry constraints. From equation 1.6, the eigenvalue and $k_\parallel$ are determined by the cross-sectional geometry and the distribution of the material. The first factor contributes to waveguide dispersion, implying that more field spreads from the core into cladding for a longer wavelength. When the frequency approaches localized plasmon resonance frequency ω_{SPP}, localized plasmon resonance behaviour dominates for every plasmon mode in a NW. The first two modes are important for metal NWs with radii bigger than 50 nm (typical for a chemically synthesised nanowire); their interference can be utilised in the construction of various devices[107].

Plasmon modes in cylindrical nanowires

Although nanowires in real-life experiments usually have a pentagonal or rectangular shape, a cylinder is the most straightforward geometry for calculations. It represents the general properties and phenomena of other geometries. The electric field distribution of modes in cylindrical symmetry nanowires can be expressed as $E(x,y,z) = E(r)e^{im\varphi + ik_\parallel z}$, where r is the distance from the centre of the nanowire $r = \sqrt{x^2+y^2}$; $E(r)$ is the radial field distribution; $e^{im\varphi}$ is the angular distribution and term $e^{ik_\parallel z}$ is responsible for the distribution along the nanowire (z-direction). The sign of m determines the handedness of the plasmon mode. Except for the fundamental mode for which $m = 0$, higher modes are doubly degenerate $m = \pm 1, \pm 2, ...$ with different handedness (chirality). Different combinations of the $m = \pm 1$ modes are depicted in Figure 1.19d. Panels a-c of Figure 1.19 present two lowest-order plasmon modes. Unlike the dielectric fibre, the fundamental mode (m = 0) is a transverse magnetic mode (TM_0) with a radially polarised electric field. In this case, induced magnetic fields are perpendicular to the surface of the NW. Second-order modes are hybrid (HE_1) and doubly degenerated. The experimentally observed characteristics of modes is the field distribution, which is reflected in Figure 1.19 d via the fluorescence intensity of QDs coupled with plasmonic modes. Different modes are selectively excited by different laser beam polarization. Interference of plasmonic modes leads to variations in the electric field, which results in differences in observed fluorescence intensity.

As the radii of NW increase and their curvature resembles a flat surface, then n_{eff}

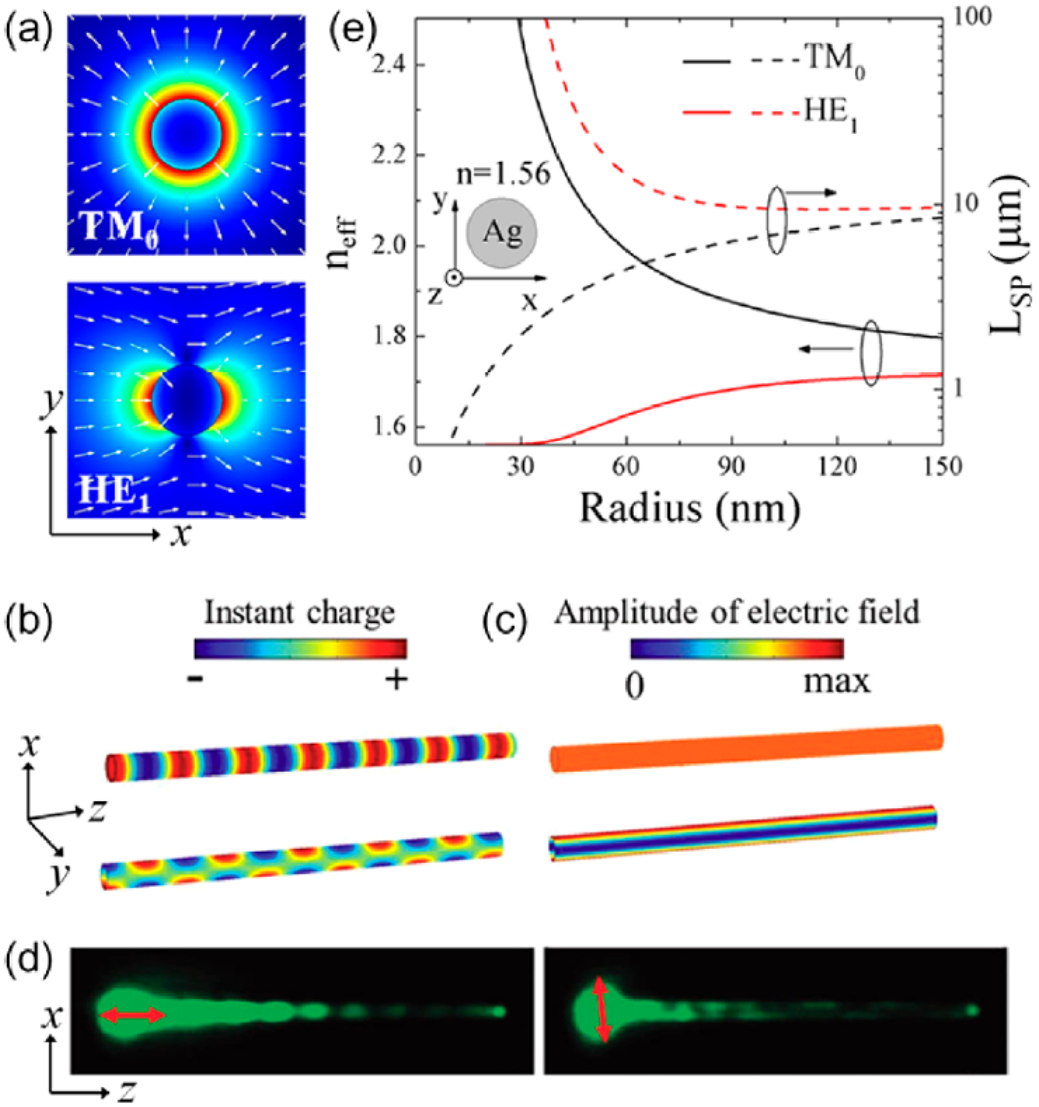

Figure 1.19: Behaviour of different SPP modes. (a) TM_0 and HE_1 modes and their electric field distributions.(b) Instant charge and (c) electric field amplitude for TM_0 (upper) and HE_1 (lower) modes. (d) QDs fluorescence maps when the laser is focused at the end of the nanowire with polarization marked by the arrow. (e) Effective refractive index (solid line) and length of plasmon propagation (dashed line) as a function of silver nanowire radii[107].

approaches its value on a flat surface (Figure 1.19 e). As radii decrease, n_{eff} of HE_1 tends to the value of the refractive index of the medium. This implies that this mode is nearly non-confined, and the field expands and resembles a polarised wave in free space. Compared to each other, n_{eff} of TM_0 increases dramatically, indicating a high confinement of the mode. This relationship is reflected in the propagation length behaviour of both modes (propagation length (L_{SPP}) is defined as the distance at

which the plasmon intensity decays to 1/e of its initial value). As mentioned above, higher confinement leads to greater damping. Both modes have similar n_{eff} and propagation lengths for large NW radii. However, for small radii n_{eff} of HE_1 mode is much smaller than of TM_0, thus propagation length for HE_1 is greater than for TM_0.

Plasmon modes on substrates

In typical experiments, NWs are placed on a substrate. It introduces the inhomogeneity of the environment, breaks the symmetry, and modifies the supported eigenmodes. Figure 1.20 presents examples of SPP modes on the substrate. These plas-

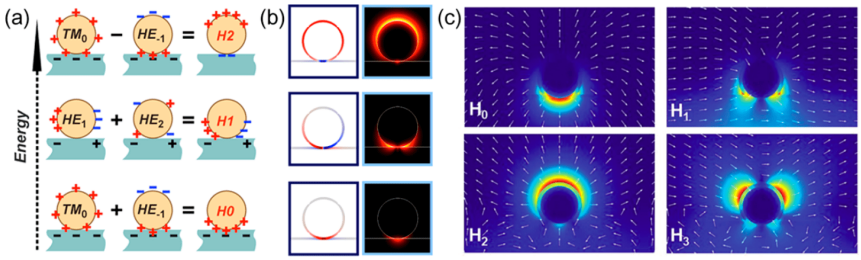

Figure 1.20: (a) Modes on a substrate as hybridisation of cylindrical NW plasmon modes induced by the substrate. (b) Calculated charge and power distribution. (c) Four lowest energy-mode and their electric field distributions[107]

mon modes can be seen as a hybridization of the original plasmon modes between metal and different dielectrics. For example, the in-phase coupling between the TM_0 and HE_1 modes results in hybridised H_0 and out-of-phase coupling results in the H_2 mode. Hybridisation theory states that in-phase coupling leads to lower energy than out-of-phase coupling, which is consistent with simulations[107]. Nevertheless, hybridised modes in a NW on a substrate are not always guiding modes but can become leaky for lower frequencies or wider nanowires. H_2 mode can serve as an example; most of its power is distributed in the upper part of the metal-air interface, and its effective refractive index is higher than 1. At the same time, n_{eff} of the H_2 mode can be smaller than the refractive index of the substrate. In this case, $Re(k_{\|}) < Re(n_s k_0)$, so the field on the substrate is no longer evanescent and the mode becomes leaky. In the situation described above, H_1 and H_2 are leaky for lower frequencies, and H_0 is a bound guiding mode for a broader frequency range[108]. The radiation leakage introduces additional losses during plasmon waveguiding. However, they can be utilised for plasmon field imaging, and, moreover, the wave vector $k_{\|}$ of leaky mode can be experimentally determined through Fourier imaging[109]. Even though leaky modes have additional factors contributing to the losses during propagation, they usually have a lower attenuation. The Ohmic resistance is the primary factor contributing to losses, and leaky modes have a higher portion of the field localised out of the metal resulting in weaker signal damping.

1.2.6 Influence of wavelength and nanoparticle' size on SPP properties

Metallic nanowires can generally support multiple plasmon modes. These modes exhibit different electric field distributions and, consequently, distinct characteristics. Spatial distribution and operating wavelength are major factors for field distribution in the metallic waveguide. Electric field distributions for two lowest-order modes (numbered by increasing effective refractive index) are presented in Figure 1.21. 1st-

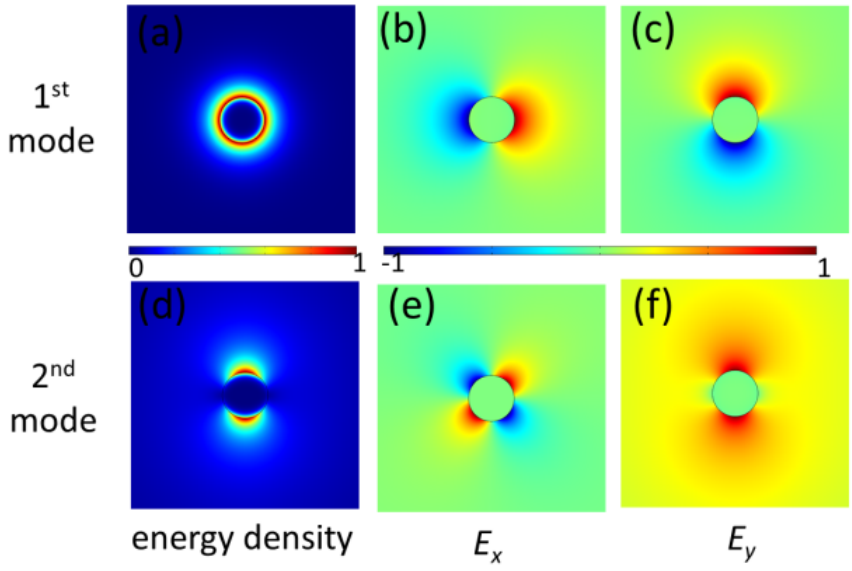

Figure 1.21: Calculated 1st and 2nd SPP mode energy density, electric field E_x and E_Y components distribution at 1000 nm wavelength for a silver nanowire embedded in SiO_2 matrix (r=100 nm)[110].

order is characterized by the E_X and E_Y components being anti-symmetric with respect to the nanowire centere. For the 2nd-order mode, the E_X and E_Y components are perfectly symmetric with respect to the nanowire centere. The behaviour of the effective refractive index n_{eff}, the propagation length L_{SPP}, and the mode area A_{eff} calculated for different wavelengths and radii are plotted in Figure 1.22[110]. The effective refractive index n_{eff} for both modes decreases with increasing wavelength. However, nanowire radii have the opposite influence for 1st and 2nd modes. The 1st-order mode refractive index decreases with increasing diameter, while the 2nd-order mode decreases. As shown in Figure 1.22a, the effective refractive index drops below those of SiO_2 (n=1.45) and diminishes for certain diameter-wavelength combinations. The mode area A_{eff} is defined by its total energy density per unit length divided by its peak energy density[111]. The 1st-order mode has a higher energy fraction localised in metal, and thus a shorter propagation length and mode area. In comparison, in 2nd-order mode much higher portion of the energy portion is localized in the SiO_2 layer, and thus it possesses a longer propagation length and larger

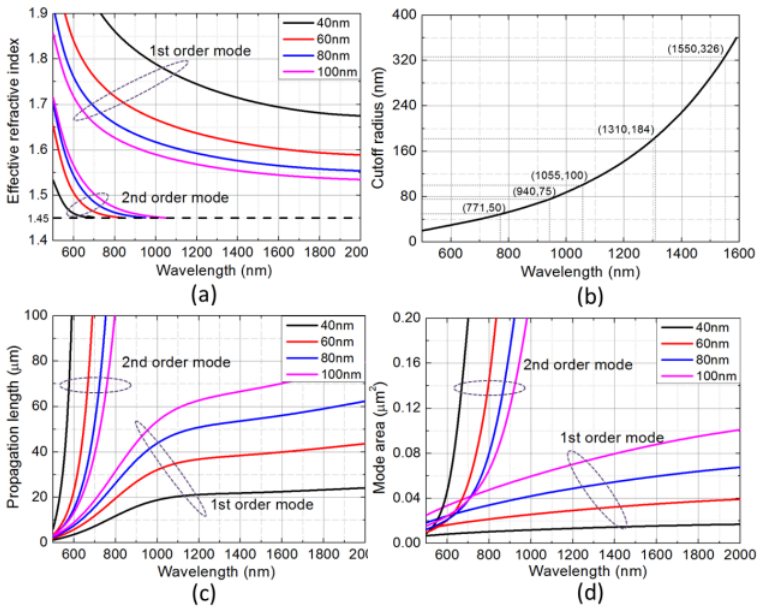

Figure 1.22: Theoretical properties of different SPP modes for a silver nanowire(a) modes effective indices, (b) cutoff wavelength for the 2nd-order mode, (c) modes propagation lengths, and (d) modes areas[110].

mode area.

Propagation modes on a SiO_2 substrate

The introduction of the substrate can result in some plasmonic modes becoming leaky, particularly at longer wavelengths. This behaviour is presented in Figure 1.23, where the energy distribution of two cylinders with different radii is shown.

It can be clearly seen that for a nanowire with radii r= 30 nm 1st-order mode is guiding. This mode originates from the coupling of the surface plasmons from the two opposite Ag/dielectric interfaces (glass and SiO_2). Due to the refractive index mismatch, the electric field is dragged to the Ag/SiO_2 interface. At r = 50 nm, this propagation mode has an effective refractive index lower than that of the substrate. Therefore, with increasing radii guiding mode turns into a leaky one. The energy distribution displayed in Figure 1.23(d) shows that the substrate's large refractive index is responsible for the energy being dragged into the substrate rather than around the nanowire. Further analysis of the effective refractive index, propagation lengths, and mode areas is depicted in Figure 1.24. As the wavelength increases, the effective refractive index decreases. This decrease can be explained by the lower penetration depth of SPP into the metal, and thus weaker coupling of the surface plasmon into the Ag/dielectric interface. Consequently, a larger portion of the energy is dragged into the SiO_2 substrate, leading to a lower refractive index. It is worth noting that there is no cutoff radius below 615 nm wavelength; thus below this wavelength the 1st-order

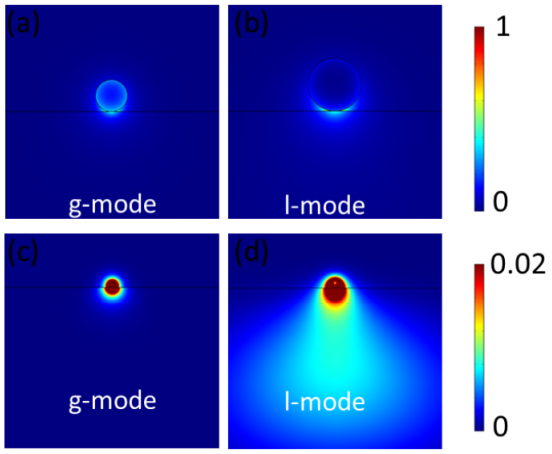

Figure 1.23: Cross section energy distribution of silver nanowires modes at the 1550 nm for (a) g-mode (r=30 nm) and (b) l-mode (r=50 nm). (c) and (d) differs from (a) and (b) in a color bar saturation[110].

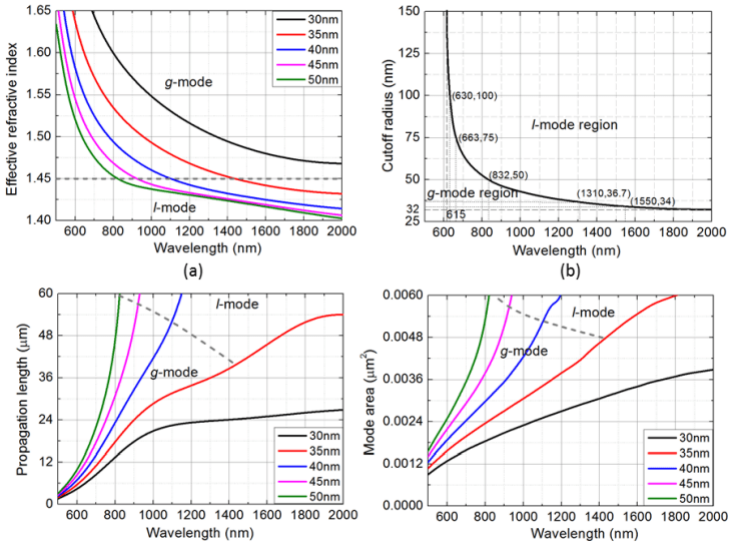

Figure 1.24: Comparision of theoretical properties of guiding and leaky SPP modes. (a) Effective refractive index (b), cutoff wavelength, (c) propagation length (d) mode area versus wavelength calculated for varying nanowire radii. A dashed line denotes boundaries between guiding and leaky modes[110].

mode is always guiding. In contrast to dielectric waveguides, metal nanowires on the substrate can support guiding modes for arbitrarily small non-zero radii. The leaky mode exhibits a larger propagation length and mode area than the guiding mode due to a high fraction of energy localised in the SiO_2 region rather than Ag and air. For both modes, the propagation length increases with increasing diameter as a result of

the low metal losses at long wavelengths.

1.2.7 Remote activation of fluorophores via SPP

Silver nanowires have been extensively utilized in experiments to excite molecules remotely[112]. For example, in the first experiment, Alexa 647 fluorophore was bound to chemically synthesized silver nanowire laying on glass substrate[113]. Then these molecules were excited by surface plasmon polaritons. By avoiding direct optical excitation, they were able to reduce nanowire background emission and molecular photodegradation. Then by combining switching fluorescence microscopy and numerical simulations through molecules point spread functions, they were able to determine the exact position and orientation of a single fluorophore on the nanowire. Exemplary point spread functions of molecules based on the position and orientation of the nanowire and nanowire diameter are presented in Figure 1.25. The

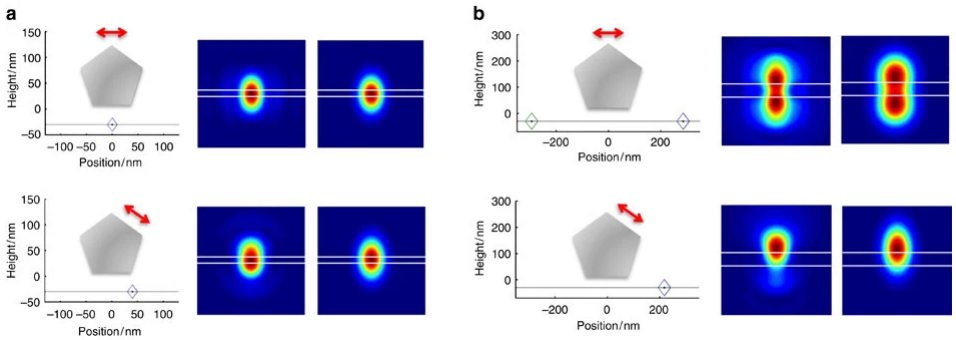

Figure 1.25: Simulations of oscillating dipoles point spread function based on their orientation and position relative to the nanowire[113].

second experiment demonstrates remote activation and detection of up-converting nanocrystals deposited at the end of the nanowire[114]. To prepare a sample for this experiment, droplet containing up-converting nanocrystals was dpeosit at the end of the nanowire using a micropipete. Then the sample was tested on confocal microscope. The scheme of this experiment with a fluorescence map is presented in Figure 1.26. When the sample is scanned with a classic confocal microscope, the end of the nanowire without crystals is illuminated by infrared light; it is possible to observe strong emission from the same end. This emission indicates remote excitation of up-converting nanocrystals and launching surface plasmon polaritons back to the excitation point. Authors of the publication can detect emission characteristics of remotely excited up-converting nanocrystals. However, the spectrum is highly damped in the green region due to higher Ohmic losses of blue-shifted surface plasmon polaritons.

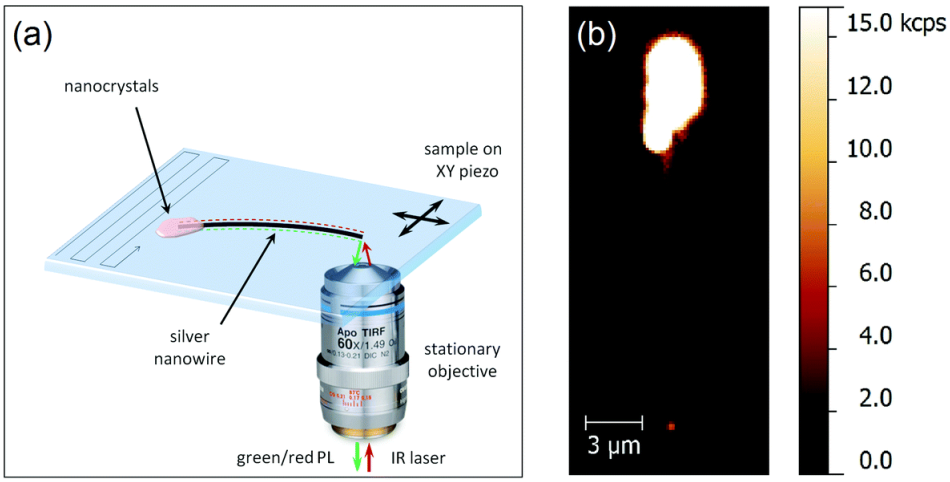

Figure 1.26: Remote excitation of up-converting nanocrystals. (a)Scheme of an experiment, (b) confocal fluorescence intensity map[114].

Chapter 2

Materials and Research Methods

2.1 Experimental techniques, numerical simulations, and sample preparation

This section describes the photochemistry of PCP, experimental and numerical techniques utilised in studies.

This sections begins with characterization of spectral properties of PCP and photophysics of thereof (Section **2.1.1**). Then the following parts of this section describe wide-field (**2.1.2**) and confocal microscopes (**2.1.3**) used for fluorescence enhancement studies. Wide-field microscope gives the ability to study sample response on the excitation wavelength using the same detection path, while a confocal microscope is used to record fluorescence decay curves and emission spectra at the selected spots of the sample. Another type of microscope (**2.1.4**) with confocal-like excitation and wide-field detection is utilised for the excitation of propagation plasmon modes. Subsections (**2.1.5**) and (**2.1.6**) describe the microscope used for the characterisation of the morphology of AgNWs. Subsection (**2.1.7**) provides technical details on the acquisition of scattering, excitation and emission spectra. The next two subsections (**3.4.1** and **3.4.2**) describe the procedure for PCP conjugation with nanowires and sample preparation for fluorescence microscopy studies. The last two sections(**2.1.8** and **2.1.9**) provide procedures of mathematical modelling of light scattering and light waveguiding by AgNWs.

2.1.1 Peridinin-Chlorophyll-Protein Complex

The SAv-PerCP used in this study was bought from $BD-Pharmingen^{TM}$. It is a bioconjugate consisting of two parts: photoactive peridinin–chlorophyll-a protein (PCP) and streptavitin (SAv) that is supposed to bind to biotin moieties. However, in the following parts of the thesis, it is referred simply as PCP.

PCP is a light-harvesting protein produced by marine algae. Its primary role is to absorb light and transmit energy to the reaction centres (in the case of algae, to Photosystem II[115]). PCP is an attractive component of hybrid nanostructures and was chosen as the object to study, due to the following properties:

- is commonly utilized as fluorescent marker in sensing,
- simple structure,
- water solubility,
- high stokes shift (reaching up to 200 nm),
- broad absorption in the visible region.

These properties make PCP ideal structure to study wavelength-dependent properties of nanostructures in a broad spectrum of light.

Excitation and emission spectrum is present in Figure 2.1. The excitation spec-

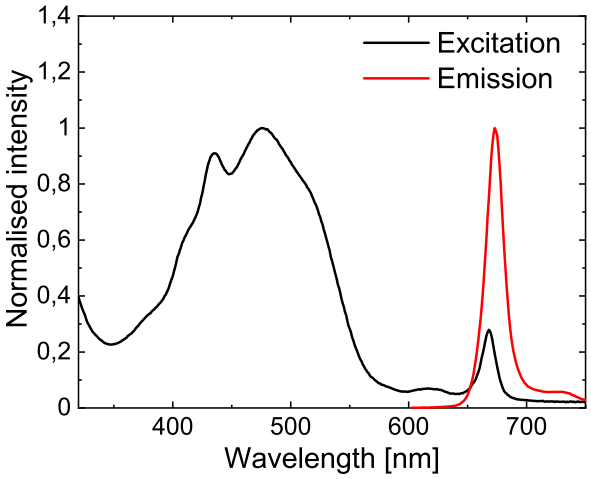

Figure 2.1: Excitation and emission spectra of SAv-PerCP water solution.

trum is dominated by a broad band spanning from 350 to 550 nm with complex structure, and another much weaker band at 660 nm. In the emission spectrum only one band centered at 673 nm is present.

Structure and photo-physics

In water solution, PCP exists in the form of a trimer with 8 peridinins and 2 Chlorophyll *a* moieties in each mer. The pigments in each subunit are organised in groups consisting of four Perdinins (Pers) and Chlorophyll *A* (Chl *A*) molecules, giving in a total 12 Pers and 2 Chl *a* for a mer. Its molecular weight is 123,8 KDa[116]. The distance between peridinin moieties ranges from 4 to 11 Å, and the distance between Mg atoms in chlorophylls is 17,4 Å. The crystal structure of PCP is presented in Figure 2.2.

The electronic excitation of Pers is responsible for absorption in the 400-550 nm region, whereas Chl *a* absorbs around 670 nm. The energy absorbed by Pers is transferred to Chl *a* with an efficiency of approximately 90%[117], which is then emitted as fluorescence. The energy transfer pathways that occur in PCP are summarised in Figure 2.3.

2.1.2 Wide-field fluorescence microscope

Widefield fluorescence microscopy is an imaging technique in which the whole sample is illuminated with light of a specific wavelength, exciting fluorescent molecules within it. Emitted light is visualised through eye pieces or captured by a camera. The scheme of the wide-field fluorescence microscope used in this thesis is presented in Figure 2.4. Excitation light is provided by four LED illuminators (Prizmatix) coupled with excitation filters (405 nm, 480nm, 535 nm, 630 nm) mounted on a rotating wheel

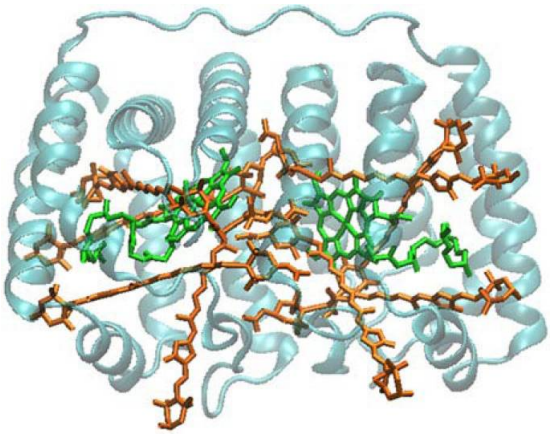

Figure 2.2: Structure of a PCP monomer. Pers are marked orange, and chlorophyll *a* is green[116].

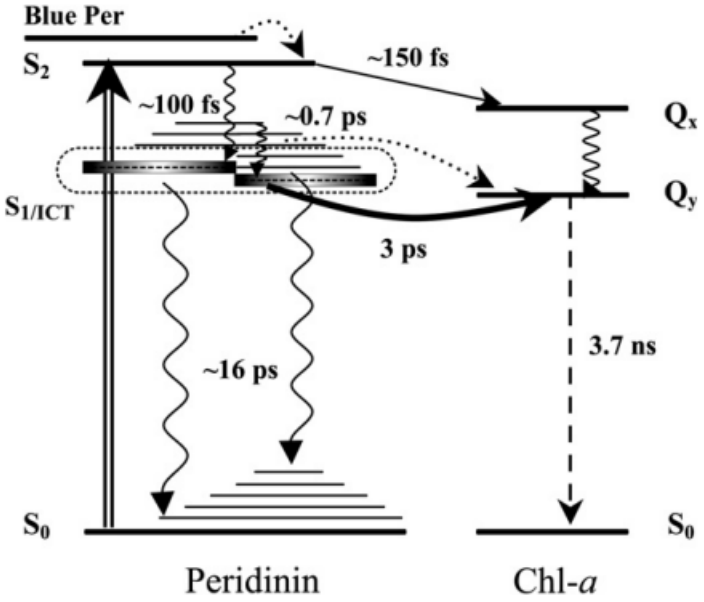

Figure 2.3: Energy levels and transfer pathways in PCP and their time constants. Intramolecular relaxation processes are denoted by wavy arrows, dashed arrows, fluorescence, and solid arrows, main energy transfer channels. Dotted arrows represent possible minor energy transfer channels[118].

which allows a choice of excitation wavelength while utilizing the same unchanged detection path. Using the same detection path ensures that no additional measurement differences are introduced due to the apparatus. Just before each experiment, the LED power was set to 100 µW. The excitation light is reflected off a dichroic mirror (T650 LPXR Chroma) and focused onto the sample through an objective lens (Plan Apo, 100x/1.4 NA oil immersion objective Nikon). Then, the fluorescence is collected

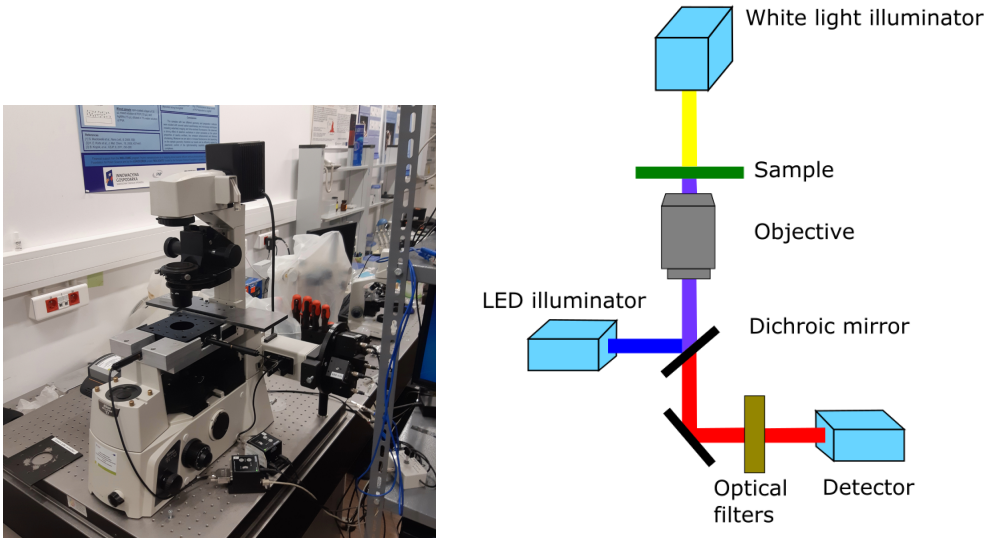

(a) Photo of the wide-field microscope (b) Scheme of the wide-field microscope

Figure 2.4: Photo(a) and scheme(b) of wide-field fluorescence microscope.

by the objective lens and transmitted through the dichroic mirror. The transmitted beam passes emission filters (FEL650, FELH650, FB670-10 Thorlabs). Finally, the signal is gathered by an iXon Du-888 EMCCD camera (Andor). The camera acquisition time was set to 1 s, the binning was set to 2x2, and the electro-magnetic gain to 5. Incandescent lamp at the top was used to localize nanowires on the sample in transmitted light mode.

2.1.3 Confocal fluorescence microscope and time-correlated single photon counting

In a confocal fluorescence microscope, laser light is focused onto the sample, and every spot of the sample is scanned separately and combined into a fluorescence map. In this work, a home-built confocal microscope was used; its scheme is presented in Figure 2.5. It operates on the following principles: The light beam from the 488 nm laser passes through a pair of lenses, between which a 25 µm pinhole is placed. The main role of the pinhole is to filter higher modes of laser light; after filtering, the light beam is parallel with the Gaussian intensity distribution. The laser worked in pulse mode, with a 20 MHz repetition rate and 12 µW power. The filtered beam is then guided into the microscope body, passing through a 50/50 beam splitter, and is focused onto a sample through a high numerical aperture oil immersion objective (NA = 1.4). A sample is placed in a piezoelectric sample holder and scanned point by point. The fluorescence emitted from the fluorophore is then collected by the same objective, and 50% of it passes through the beam splitter. Then out of focus light is removed when passing through another pinhole and goes through a long-pass filter

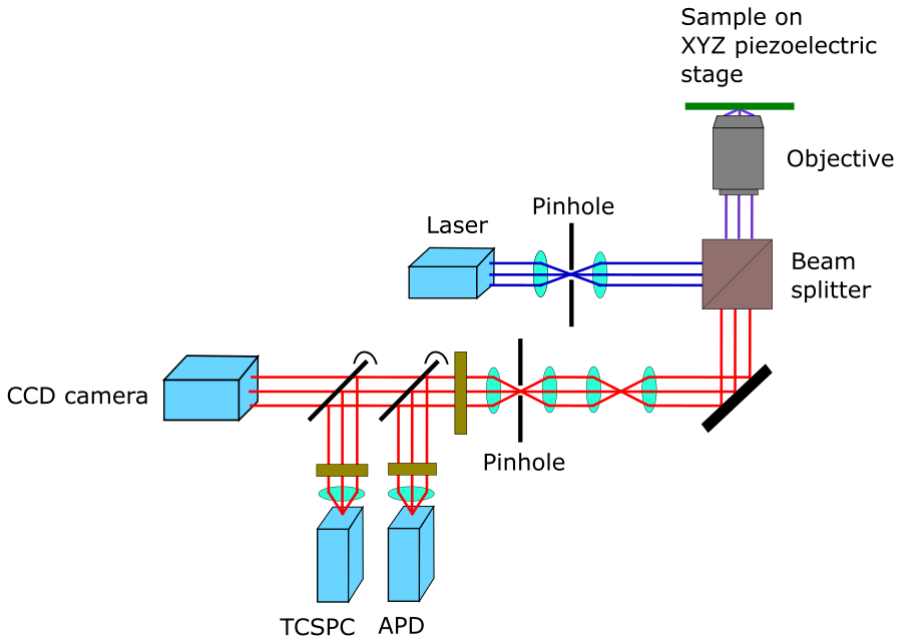

Figure 2.5: Scheme of confocal fluorescence microscope.

(HQ655LP, Chroma). Finally, it is focused on one of the three detectors through a set of mirrors.

- In the first case, the beam passes the bandpass filter (Chroma ET 675/20) and then is focused by a lens onto the detector(avalanche photodiode (APD) Perkin Elmer SPCM-AQRH-16). Finally, a fluorescence intensity map is created by recording the fluorescence signal at each point.

- In the second case light beam coming out of the microscope is separated into monochromatic parallel components by an Amici prism. Each component is gathered by a different detector column (CCD camera Andor iDus DV 420A-BU), and then the signal recorded at each column is summed up to create fluorescence emission spectra.

- In the third case beam passes the bandpass filter (Chroma ET 675/20) and then is focused by the lens onto the detector(Avalanche photodiode idQuantique id100-50). This detector was utilised in time-correlated single-photon counting (TCSPC) experiments, which are based on the following rules: first, the sample is excited with such power that, in most cases, only a single fluorescence photon is emitted. Then the detector setup records the time between sample excitation and the arrival of the fluorescence photon. This procedure is repeated multiple times, and based on measured times, a fluorescence decay curve is created.

In all experiments involving the confocal microscope, the fluorescence map was first gathered with a step of 500 nm per pixel and 10 ms acquisition time. Then, at the selected points, the fluorescence decay curves were measured with an acquisition time of 60 s.

2.1.4 Two-objective fluorescence microscope

The home-built two-objective microscope, which combines features of the wide field and the confocal microscope (it provides confocal excitation and wide-field detection), was utilised for excitation and observation of propagating surface plasmon modes. Scheme and photo of the microscope is presented in Figure 2.6. This setup is

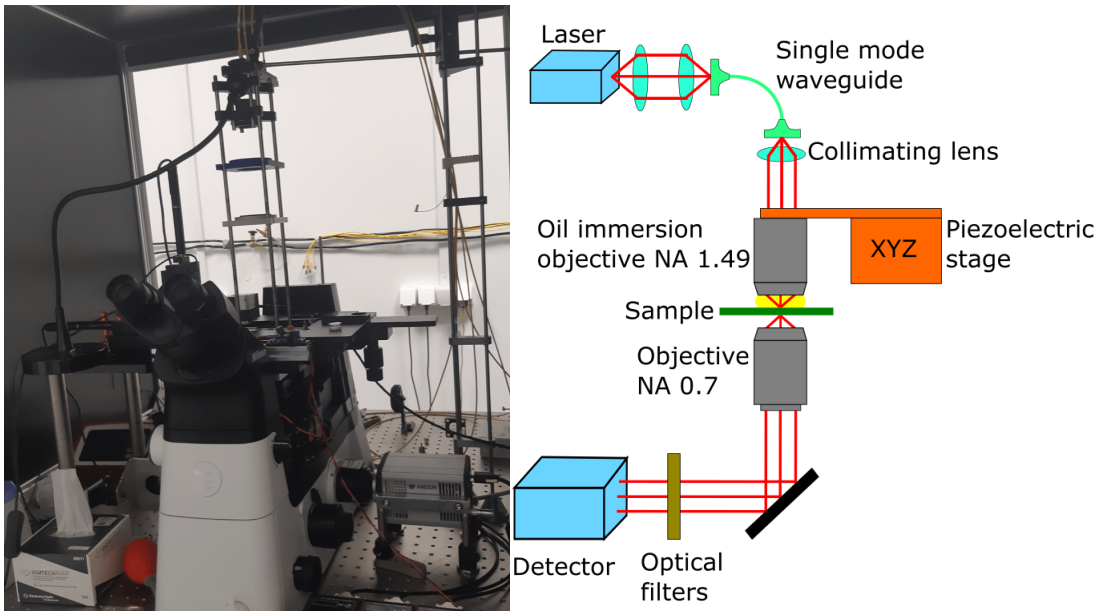

(a) Photo of the two objective fluorescence microscope.

(b) Scheme of the two objective fluorescence microscope

Figure 2.6: Photo (a) and scheme (b) of two objective fluorescence microscope.

based on a Nikon Ti-U2 microscope body. The diode laser (LS635-150, Spectra Laser) is coupled to a single-mode optical fibre through a pair of lenses. Before every experiment, the laser power was set to 5 µW. Upon exiting optical fibre beam passes the collimating lens, then is focused onto the sample by high numerical aperture objective (Apo TIRF 1.49NA/60x oil immersion Nikon). Light from the sample is gathered by the second bottom objective (S Plan Fluor 0.7NA/60x Nikon). Then fluorescence signal is filtered by FELH650 (Thorlabs) and ET675-20m (Chroma) filters. The detector is Zyla 5.5 sCMOS (Andor Technology). The acquisition time of the camera was set to 100 ms and binning to 2x2. To localise nanowires on the sample, a small white light LED was used, illuminating the sample from the side.

2.1.5 Dark-field optical microscope

Dark-field microscopy is a technique utilized in a specimens that are not imaged well under normal illumination conditions (for example weakly absorbing). It provides great contrast for highly scattering objects like metallic nanoparticles, however most of the information is restricted due to diffraction limits. In this mode, only oblique rays interact with the specimen. This is achieved by the Abbe dark-field condenser, which forms an inverted hollow cone of light with the focus centred on the specimen plane. In spots where scattering objects are localised, they diffract and reflect light rays, only such rays can reenter the objective, and these objects are viewed as bright spots in the image. Because of the greater NA of condenser than objective's, in the areas without scattering objects, the light rays cannot enter the objective so they appear dark in the image. In this work LV150 optical microscope (Nikon, 10x objective) with a Fi-color CCD camera (Nikon) was used.

2.1.6 Scanning electron microscope (SEM)

Scanning electron microscopy is a highly versatile technique used to obtain high-resolution images and detailed surface information of samples. It is a type of electron microscopy that uses a focused beam of electrons to scan the surface of a specimen and generate images at a much greater resolution compared to optical microscopy. Energy of electrons, and thus associated with the de Broiglie wavelength, can easily be tuned by accelerating voltage. In typical SEM the corresponding wavelength of electrons is much smaller than the wavelength of light in visible region(400-800 nm), thus they achieve much better resolution limits than optical microscopes. The resolution limit depends on multiple parameters such as: accelerating voltage, working distance, current or conductivity of the specimen. The resolution of SEM instruments can range from 1 nanometer up to several nanometers. Due to the interactions of electrons with the sample, various information can be extracted, notwithstanding the uppermost one is about the sample topography. For high resolution, samples are observed under high vacuum. In this work, Nova NanoSEM 450 microscope with an E-T detector at 10 kV acceleration voltage working in immersion mode was used. All specimens were measured on indium tin oxide (ITO) conducting substrates.

2.1.7 Scattering, excitation and emission spectra

The excitation and emission spectrum of the PCP and PVP polymer after synthesis was collected using a FS5 spectrophotometer (Edinburgh Instruments). This spectrophotometer excitation spectral coverage is 230 nm - 1000 nm and emission spectral coverage is 200 - 870 nm. Ultraviolet-visible (UV-Vis) scattering spectra of AgNWs dispersions were taken using Evolution 300 dual-beam spectrophotometer (Thermo Electron Corporation), which is able to record spectra with a wavelength range 190 to

1100 nm. All solutions were measured in cuvettes made from polymethyl methacrylate with a 1 cm optical path and scan speed 10 nm/s and slit width 1 nm.

2.1.8 Mathematical modelling of light scattering by AgNWs

Simulations of light scattering by AgNWs were performed using COMSOL Multiphysics and its RF module, employing the scattered field formulation. The software is based on the Finite Element Method, as described in detail in[119]. In the simulations, I used a 2D model, assuming that the mode profile remains invariant in the z direction.

The 2D model represented the cross-section of a silver nanowire with a PVP coating, embedded in a PVA matrix (top) and placed on a glass substrate (bottom). This model corresponds to an infinitely long silver nanowire on a glass substrate. The permittivity values were obtained from the following sources: silver from McPeak[120], PVP from König[121], and PVA from Schnepf[122]. The refractive index of glass was set to 1.523, as provided by the manufacturer.

The mesh used in the simulations is shown in Figure 2.7.

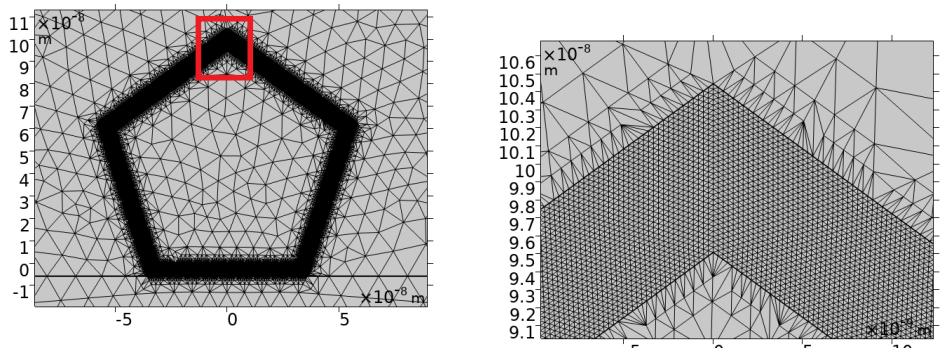

(a) Overview of the mesh and geometry, are of close-up view has been marked with red box

(b) Close-up of nanowire's corner

Figure 2.7: Overview of the mesh used in calculations. The maximum element size is 19 nm. However, the mesh is much denser in the PVP region for better resolution. Boundaries between domains are shown as thick black lines. The PVP-coated Ag nanowire is surrounded by PVA from the top and sides and glass from the bottom.

The maximum mesh element size was set to 19 nm. The PVP coating area was refined by a factor of 5, achieving a spatial resolution below 0.2 nm. The nanowire was illuminated from bottom to top of image(from glass into PVA) by an unpolarized plane wave with an electric field intensity of 1 V/m. This setup allowed the wave to propagate through the glass and then through the PVA region, where it was scattered by the nanowire. A Perfectly Matched Layer (PML) was used to absorb all outgoing wave energy, eliminating impedance mismatches that could cause stray reflections at the boundary. The PML reduced computational costs while maintaining the required accuracy. The scattering cross-section was calculated by integrating the Poynting

vector of the scattered field over a circular region between the nanowire surface and the PML. The absorption cross-section was determined by integrating heat losses over the nanowire volume. A 50 nm-thick PML with a scaling factor of 0.5 was applied to truncate the computational domain, following COMSOL's recommendations[119]. Simulations were conducted for nanowires with diameters ranging from 40 to 200 nm, in 20 nm increments, at operating wavelengths of 405, 480, 535, and 630 nm.

2.1.9 Mathematical modelling of AgNWs waveguiding properties

The simulations were performed using Comsol Multiphysics 5.5 with RF module. The 2D model is used for a varying-width pentagonal nanowire with a 6 nm (PVP) coating. Nanowire is placed on a glass substrate and surrounded by PVA. Triangular mesh is used with a maximum element size of (nanowire diameter/40) for nanowire and coating and 20 nm for the environment. The relative tolerance in successive eigenvalues is 10^{-6}. The permittivity data of silver used in this calculation is taken from McPeak[120]; PVP from König[121]; PVA from Schnepf[122], and the refractive index of glass is set to 1.523 as provided by the manufacturer. Geometry and mesh used in simulations are presented in Figure 2.8. Simulations were done for nanowires with diameters ranging from 40 to 200 nm with a step of 20 nm. The operating wavelength was set to 635 nm.

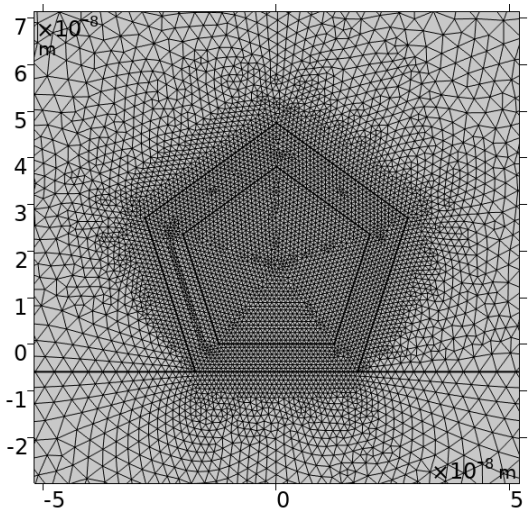

Figure 2.8: Overview of the mesh and geometry used in the waveguiding simulation of 40 nm wide AgNWs. Boundaries between domains are shown as thick black lines. The PVP coated Ag nanowire is surrounded by PVA from the top and sides and glass from the bottom.

Chapter 3

Experimental

3.1 Purpose and scope of work

The objective of this dissertation was to explore the relationship between fluorescence enhancement, plasmon propagation length, and the dimensions of AgNWs. These characteristics of AgNWs were examined in two configurations: 1) AgNWs incorporated within a PCP and PVA layer, and 2) a conjugate of AgNWs and PCP, typically seen in applications such as biosensors, also within a PVA layer. The research process was segmented into progressive phases, which can be outlined as a series of interim objectives:

- Synthesis and characterization of silver nanowires with various morphologies.
- Investigation of PCP fluorescence enhancement and length of plasmon propagation of AgNWs in layer of PCP.
- Investigation of PCP fluorescence enhancement and length of plasmon propagation of AgNWs in conjugate of AgNWs and PCP.
- Theoretical investigation of the main factors influencing fluorescence enhancement and waveguiding properties of AgNWs.
- To investigate the feasibility for remote excitation of fluorophores by AgNWs.

3.2 AgNWs synthesis and characterisation

In the course of studies various synthethic procedures were tested, to obtain AgNWs with different morphologies. AgNWs synthesised in standard polyol method were short, and control of their diameter in reproducible way was problematic. Thus hydrothemal method was chosen. Compared to polyol method, hydrothermal synthesis has two additional features, control over the type and concentration of the reducing agent. In this thesis hydrothermal synthesis with four sets of reducing agents is presented, as the most convincing way to achieve the goal - synthesis of AgNWs with various morphologies. Lengths of silver nanowires were characterized by white-light dark-field microscopy, and their diameters were measured utilizing scanning electron microscopy. Extinction spectra of AgNWs were measured for each synthesis, as it is a critical factor in the efficiency and applicability of nanostructure in MEF. In the course of the studies, a weak fluorescence signal originating from nanowires was observed even without an additional fluorophore present. To discover the origin of this signal, additional characterisation of the AgNW synthesis by-products was conducted.

Chemicals
Silver nitrate ($AgNO_3$, 99.9999%), polyvinylpyrrolidone (PVP, Mw = 40 000), aniline

(99.5%), sodium chloride (NaCl, 99.99%), and poly(vinyl alcohol) ((PVA), Moviol 20-98) were purchased from Sigma-Aldrich. Hydrogen peroxide (H_2O_2, 30%) was purchased from Stanlab. Acetone was purchased from Chem-pur (99.9%). All reagents were used as received without any further modifications or purifications, and their solutions were prepared in deionized (DI) water (Sartorius, Arium Comfort II, > 15MΩ/cm).

Synthesis

The procedure was based on a protocol previously described in literature[32]. However, in this article glucose is used as a reducing agent. The procedure of synthesis performed in this thesis is schematically presented in Figure 3.1.

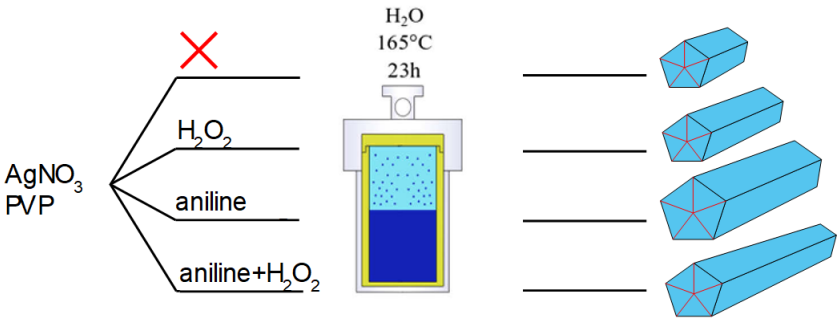

Figure 3.1: Schematic representation of the hydrothermal synthesis with 4 different reducing agents.

First, aqueous solutions of silver nitrate (0.02M, 7.5 mL), PVP (0.5 g, 2.5 ml), and sodium chloride (0.03 M, 7.5 mL) were mixed, and afterward, a “reducing solution” (2.5ml) of either

1. water in the case of AgNWs,
2. 25,2 µl of 30% hydrogen peroxide in the case of AgNWs H_2O_2 ;
3. 20 µl aniline 99,5% aniline in the case of AgNWs aniline;
4. 20 µl of 99,5% aniline+2 µl 30% hydrogen peroxide solution in the case of AgNWs aniline+H_2O_2;

The mixture was added dropwise to the mixture. Afterward, the solution was mixed again and became nontransparent due to the formation of AgCl crystals. Next, each mixture was transferred to a 50 ml Teflon-lined stainless steel autoclave reactor. The reactors were heated to 100°C (4°C/min) in an oven, kept at this temperature for 1 h due to the limitations of autoclave reactors, then heated to 165 ° C (4 ° C / min) and left at this temperature for 23 h.

This step was followed by slow cooling the autoclave to room temperature overnight. The final product in the form of a grey-white precipitate was collected by centrifugation (1000 rpm, 20 min) and was washed three to five times with DI.

To purify the AgNWs and remove nanoparticles, the precipitate was dispersed in 10 ml of 0.5% PVP solution. Afterward, acetone was slowly added up to the point when AgNWs started to precipitate (about 30 ml), while gently mixing. After 10 minutes, the precipitate at the bottom was collected and supernatant was dispersed, and the procedure was repeated twice. Finally, AgNWs were dispersed in 3 ml of DI and stored at 4°C (results partially published in[123]).

As presented in the literature review of this thesis, the synthesis of AgNWs involves reduction of silver cations to metallic silver and formation/growth of silver crystals into desired shapes. The direct impact of each chemical compound utilised in the synthesis was not investigated as it is out of the scope of this thesis. However, it is worth mentioning the motivation for choosing these sets of reducing agents.

In the first sample, the only reducing agent was PVP, which as mentioned in the literature, is capable of reducing silver cations through oxidation of the hydroxyl end groups of PVP[124][125]. However, it was never used as the one and only reducing agent in hydrothermal synthesis.

In the second sample, hydrogen peroxide was introduced. It is reported that due to its oxidative properties it removes less stable crystals of silver[126].

In the third sample, aniline was introduced. Aniline is a weak reducing agent utilized in the slow growth of nanoparticles[127] depending on conditions, can be oxidized to dimers, oligomers, or polyaniline[128][129].

Finally, in the fourth sample aniline and hydrogen peroxide were used altogether.

AgNWs morphology characterization

At first, all 4 samples were characterized with an optical microscope working in a dark-field mode, and scanning electron microscope. Optical microscopy images of each sample are presented in Figure 3.2 and SEM images in Figure 3.3.

In the dark-field images (Figure 3.2) one can see elongated bright shapes associated with presence of AgNWs. Usually, they are accompanied by small points, which indicates that other types of nanoparticles are also created during synthesis. Nanoparticles can be observed among all samples. However the smallest number of nanoparticles can be spotted in the picture d. In SEM images (Figure 3.3), elongated shapes with constant width can be seen (AgNWs). They are covered with about 6 nm thick polymer layer that swells upon contact with an electron beam. The ends of nanowires differ in shape. In some cases they are pointy with clearly seen pentagonal cases (image c), while in other cases they are blunt with more spherical shape. Looking qualitatively at the microscopy images one can observe that, utilizing different reducing agents result in nanowires with varying dimensions.

To determine qualitatively this observation lengths and diameters of about 50

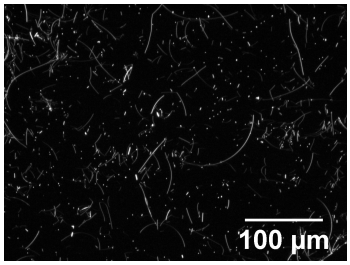

(a) AgNWs PVP

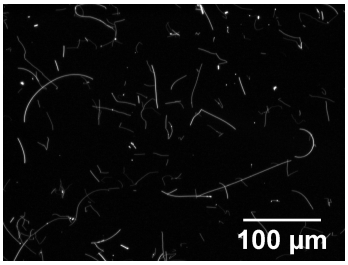

(b) AgNWs H_2O_2

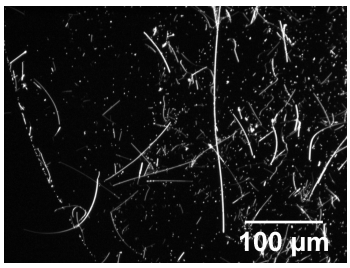

(c) AgNWs aniline

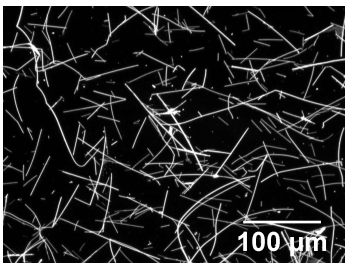

(d) AgNWs aniline+H_2O_2

Figure 3.2: Dark-field microscopy images, showing AgNWs obtained from each synthesis: (a) AgNWs PVP, (b) AgNWs H_2O_2, (c) AgNWs aniline, (d) AgNWs aniline+H_2O_2.

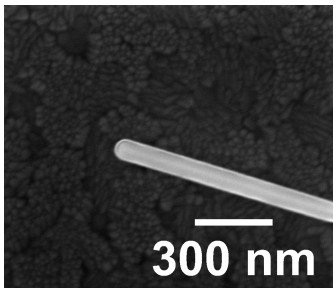

(a) AgNWs PVP

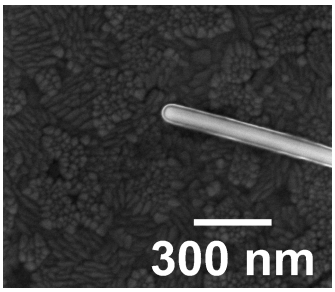

(b) AgNWs H_2O_2

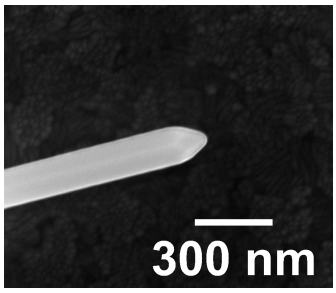

(c) AgNWs aniline

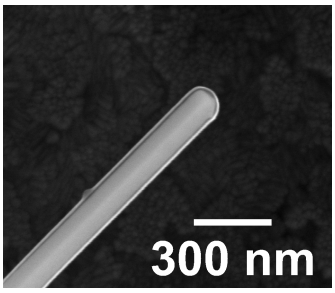

(d) AgNWs aniline+H_2O_2

Figure 3.3: SEM images, showing the end of typical nanowire obtained from each synthesis: (a) AgNWs PVP, (b) AgNWs H_2O_2, (c) AgNWs aniline, (d) AgNWs aniline+H_2O_2. The brighter outline around the nanowires is about 6 nm thick coating of PVP.

nanowires were measured for each sample. AgNWs lengths were obtained from dark-field microscopy images, and AgNWs pentagon diagonal lengths were determined with the scanning electron microscope. In the literature, the diagonal length of the AgNW pentagon is usually referred to as the AgNW diameter, and this concept is also applied in this‘work. The histograms of the lengths and diameters of each sample are presented in Figure 3.4.

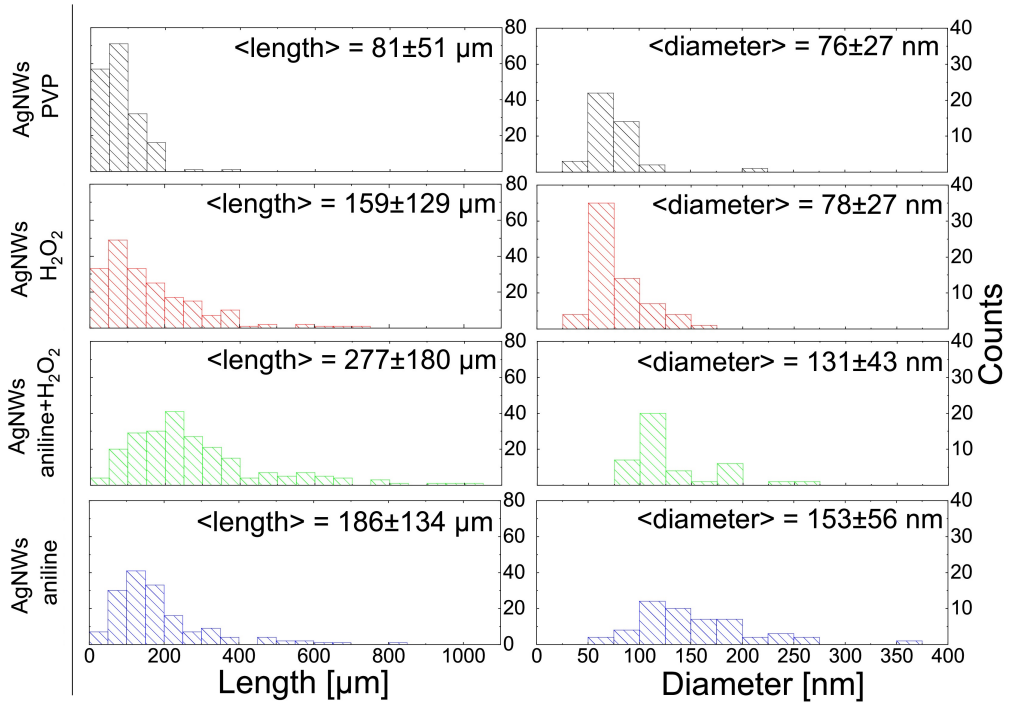

Figure 3.4: Histograms of AgNWs lengths and diameters measured for sample with 4 reducing agents.

The AgNWs synthesized with only PVP as the reducing agent are relatively thin with narrow diameter distribution. Their average diameter is 75 nm, while their mean length is 81 µm. In a few cases, AgNWs reach up to 200 µm.

In the synthesis with the addition of hydrogen peroxide AgNWs mean diameter was equal to 78 nm, the mean length was equal to 159 µm, it is worth noting that nanowires with lengths reaching up to 600 µm were observed.

In the sample where only aniline was used (AgNWs aniline), the diameter ranged from 100 to 300 nm, with a mean of 152 nm. The nanowires were shorter compared to those synthesized with both aniline and hydrogen peroxide, where the mean length was 186 µm.

In the sample synthesized with both aniline and hydrogen peroxide, the AgNWs had a mean diameter of 131 nm and a mean length of 277 µm. Some individual nanowires reached lengths of up to 1 mm.

When oxidative agent (H_2O_2) was introduced into synthesis it resulted in fewer nanoparticles and longer nanowires, compared to sample with only PVP. While aniline (weak reducing agent) was used, it also resulted in longer nanowires with fewer nanoparticles. When aniline and H_2O_2 were used together it resulted with longest nanowires and smallest number of nanoparticles. This indicates that reducing agent used in the synthesis affects dimensions and yield of AgNWs in a statistically significant way.

The shape of the nanoparticle affects its interaction with electromagnetic field. In particular, it influences its optical properties, i.e. enhancement of electromagnetic field and length of plasmon propagation or frequency of localized surface plasmon resonance. Thus nanowires with different dimensions should have different extinction spectra. Extinction spectra of AgNWs water suspensions are displayed in Figure 3.5. The spectrum of each sample has the same general feature. The maxi-

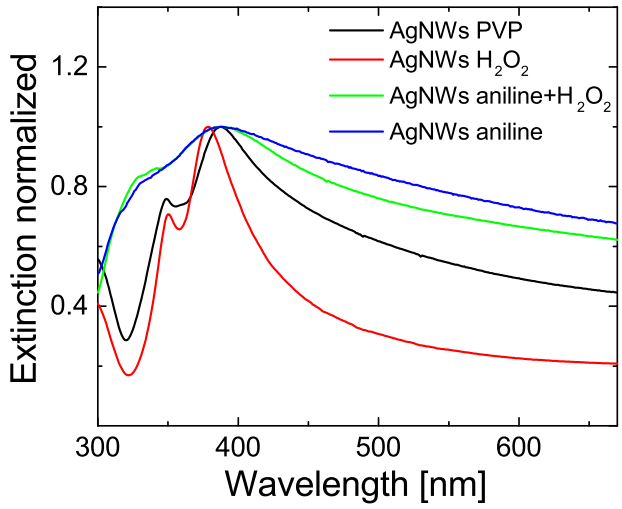

Figure 3.5: Extinction spectra of AgNWs PVP (black), AgNWs H_2O_2 (red), AgNWs aniline+H_2O_2 (green), AgNWs aniline (blue) water suspensions.

mum extinction intensity is visible around 400-390 nm, which can be attributed to the dipole transversal plasmon mode. Another local maximum of the quadrupole transversal plasmon mode can be seen around 360-340 nm. In all cases spectrum extends towards lower energies and spans the whole range of visible radiation, with higher extinction in the red part of the spectrum for samples with wider nanowires. All spectra are similar to those previously reported in the literature[130], which is an additional indicator that AgNWs were obtained. However, even though the spectra have similar shapes, they vary in relative peak intensity. AgNWs with smaller diameter have a much more distinguishable dipole and quadrupole plasmon mode and a much weaker extinction in the green-red region. This is another indication that these

samples consist of AgNWs with statistically different morphologies.

Moreover, in the course of studies, it was observed that upon strong illumination AgNWs emit a weak fluorescence signal. This behaviour has never been described in the literature. The example of such behaviour is presented in Figure 3.6, where

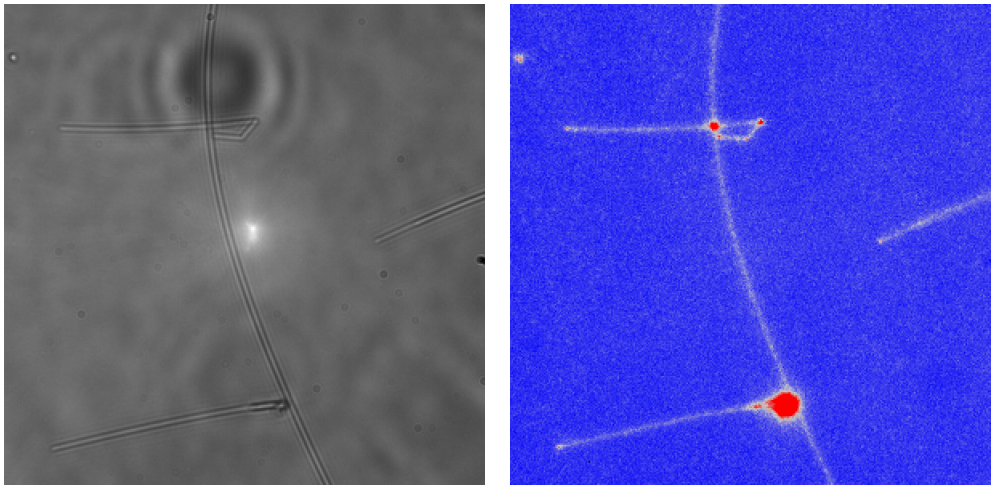

(a) (b)

Figure 3.6: Example of AgNWs autofluorescence. Images were obtained with wide-field fluorescence microscope. (a) Transmission image of AgNWs, (b) Fluorescence intensity map of AgNWs when $\lambda_{exc} = 480$ nm collected at $\lambda_{em} = 535$ nm.

nanowire excited at 480 nm with no additional fluorophores is studied utilizing wide-field fluorescence microscope. To explain this, investigations of polymer residues after the synthesis of AgNWs were carried out.

The brownish supernatant (which should be mainly composed of water and PVP) was collected after the first step of centrifugation and transferred to a glass vial. Then it was heated to 60 ° C to slowly evaporate the water. Next, the fluorescence excitation-emission map of this polymer was measured and the result is presented in Figure 3.7. For the polymer the highest fluorescence intensity is observed for 300-400 nm of excitation wavelength, with a relatively low Stokes shift. While shifting towards longer wavelengths fluorescence intensity drops significantly. For 675 nm emission (which corresponds to the maximum wavelength emission of the PCP - the only fluorophore studied in this thesis) the fluorescence intensity is nearly at a non-measurable level for all excitation wavelengths. This might indicate that previously observed AgNWs autofluorescence is caused by oxidized PVP present at the surface of AgNWs. Which might lead to high background signal, while studying fluorophores emitting in blue-green region (e.g., green fluorescent protein). However, in this thesis only PCP emitting in 673 nm was utilized, for this wavelength AgNWs autofluorescence is negligible, thus this effect can be omitted in all analyses.

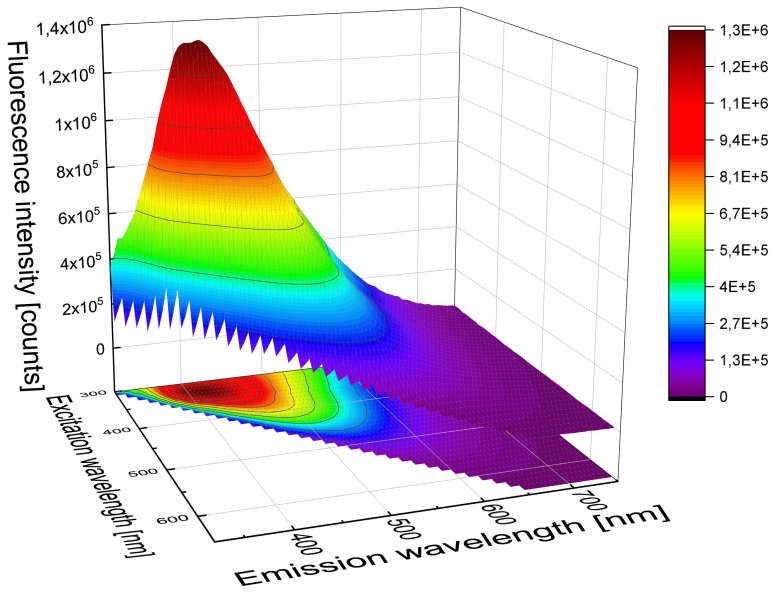

Figure 3.7: Three-dimensional excitation-emission map of residues of PVP after AgNWs synthesis with two-dimensional projection.

3.2.1 Summary

This chapter describes the hydrothermal synthesis of silver nanowires, in which four sets of reducing agents were used. Statistical analysis of microscope images revealed that when solely PVP was used as a reducing agent, AgNWs were the shortest with the smallest diameters. The introduction of hydrogen peroxide into the reaction didn't influence AgNWs diameters; nonetheless, it elongated nanowires. The introduction of an additional reducing agent - aniline, resulted in even longer nanowires with much bigger diameters. The longest nanowires were synthesized when hydrogen peroxide was used altogether with aniline, with a mean diameter between formerly mentioned syntheses. Differences in AgNWs diameters between samples resulted in differences in their extinction spectra. A well-distinguished quadrupolar resonance peak and lower scattering in the red part of the spectrum can be observed for thin nanowires. In contrast, for thick nanowires, quadrupolar and dipole peaks have similar intensity. During the synthesis shape directing polymer - PVP is oxidized; as a consequence, a weak fluorescence signal is observed when the UV-blue light illuminates the nanowire. Part of the results regarding the synthesis of AgNWs described in this chapter has been published in reference[123].

3.3 Plasmonic properties of AgNWs in PVA layer cotaining PCP

The following sections of this chapter focus on the plasmonic properties of AgNWs in which they are surrounded by a polymer matrix and randomly localised PCP molecules within PVA layer.

Samples were prepared by spin-coating (1000 rpm) 20 µl droplet of solution containing: 50x diluted suspension of AgNWs, PCP (4µg/ml) and PVA (0,04% w/w) on a glass coverslip. This procedure results in about 20-25 nm thick PVA layer (Figure 3.48) in which AgNWs and PCP molecules are randomly distributed. Thus the distance between AgNWs and PCP is different for each nanowire - fluorophore pair and is ranging from 6 to 20-25 nm; the lower distance is determined by the thickness of AgNWs coating which is unaccasable for PCP molecules, and the upper bound is determined by the thickness of PVA layer. This is schematically presented in Figure 3.8.

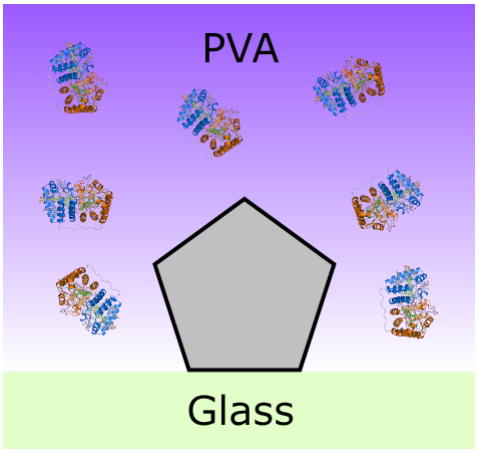

Figure 3.8: Schematic representation of sample configuration obtained by spin-coating the mixture of AgNWs, PVA, and PCP on a glass coverslip. The relative size between AgNW and PVP(red-blue protein structure) is up to scale for a 10 nm wide nanowire. The streptavidin part of the protein is not shown.

3.3.1 PCP fluorescence enhancement by AgNWs

Samples were prepared by spincoating a 20 µl mixture of AgNWs, PVA and PCP onto a glass substrate. Then nanowires were localised onto the sample utilizing transmitted light mode of wide-field fluorescence microscope, then fluorescence intensity maps were measured for 4 excitation wavelengths (630, 535, 480 and 405 nm). The chosen wavelengths cover the entire absorption spectrum of PCP. Such measurements were repeated for 30 randomly selected nanowires.

Typical fluorescence intensity maps upon wide-field illumination for each AgNWs sample are presented in Figure 3.9.

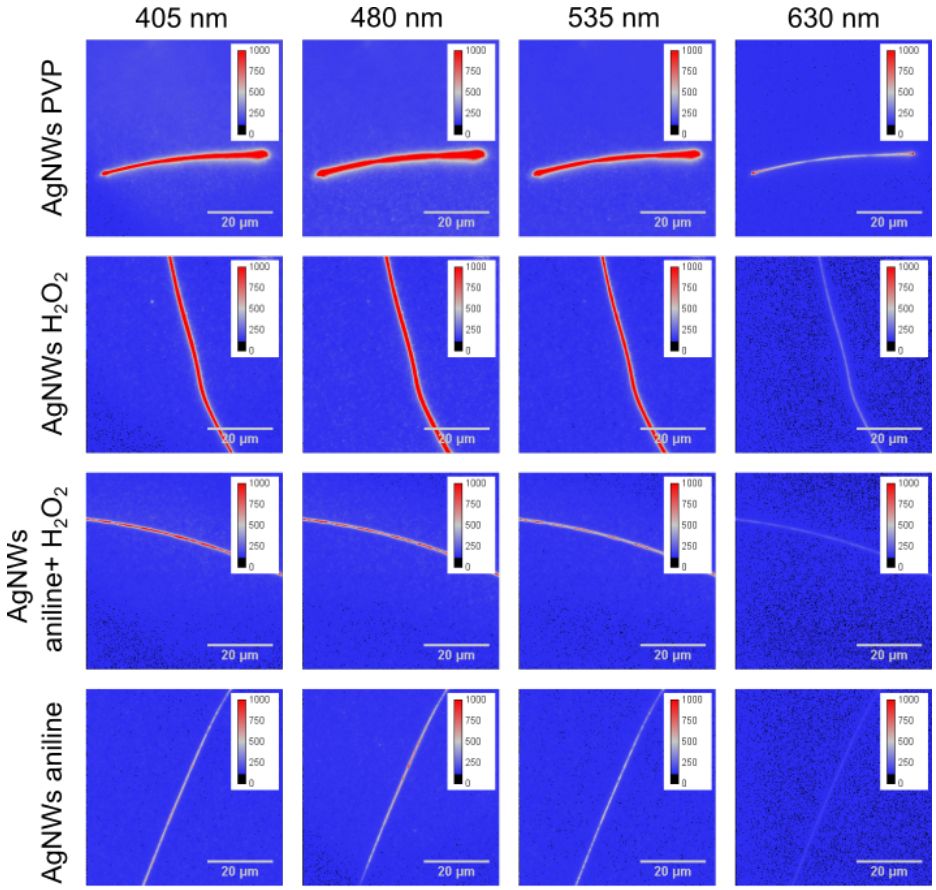

Figure 3.9: Wide-field fluorescence intensity maps of PCP. Samples were prepared by a spin-coating mixture of PCP, PVA, and AgNWs onto glass coverslips. Figures present a single nanowire from each sample excited with four different wavelengths. The colour scale bar is fixed in all maps for clarity.

In the fluorescence map, a single bright line is seen. The position of that line correlates with the position of the nanowire seen in the transmitted light. Moreover, PCP fluorescence signals can be detected in the whole observed area. Higher fluorescence intensity in the areas where nanowires are present might indicate fluorescence intensity enhancement by AgNWs or higher concentration of PCP molecules. In areas with no nanowires present, the highest fluorescence intensity is observed for 480 nm excitation wavelength while the lowest values are observed for 630 nm excitation wavelength as expected from the absorption spectrum of PCP(Figure 2.1). In contrast in the spots with nanowires, the highest fluorescence intensity is observed for 405 and 480 nm excitation wavelengths. This spectral dependence indicates that metal-enhanced fluorescence is responsible for this higher fluorescence intensity, rather than higher concentration of PCP molecules. In most of the fluorescence maps, the

ends of the nanowire are not visible as their lengths exceed the dimensions of maps collected by a detector. When the end of nanowires is imaged by the detector, they provide higher intensity of fluorescence signal compared to the rest of the sample. Three factors may contribute to that: 1) higher fluorescence enhancement due to the sharp pointy end of the nanowire; 2) fluorophores along the nanowires may couple with SPP modes, which are then scattered at the end of the nanowire; 3) non uniform PCP distribution resulting in more PCP molecules near nanowire tip. When comparing the fluorescence intensity maps sample-wise, one can spot lower fluorescence intensity for AgNWs aniline+H_2O_2 and AgNWs aniline samples. These results might indicate that for AgNWs aniline+H_2O_2 and AgNWs aniline samples fluorescence enhancement is lower than for AgNWs PVP and AgNWs H_2O_2 samples, most likely due to disparities in their diameters[123].

To further investigate into this phenomenon, fluorescence intensity maps of 30 arbitrary nanowires per sample were collected, showing the same consistent pattern. For each nanowire, fluorescence intensity was recorded at four distinct wavelengths, totalling 120 maps per sample. Comparative analysis of fluorescence enhancement across samples was then performed.

The first and most essential step of the analysis is to define the data acquisition area. Due to the limits of resolution of the microscope, even a single light emitting point appears as a few hundred nanometers wide object (the size depends on the wavelength and numerical aperture of the objective), which corresponds to a few pixels on the detector. Vice versa, on the single pixel on the detector, molecules from a few hundred nanometers wide area are being imaged. The objective is to maximize the fluorescence signal from PCP molecules interacting with nanowire while minimizing the signal from non-interacting PCP. In order to do so, the fluorescence intensity in the direction perpendicular to the nanowire was measured. The fluorescence intensity map with an area of measurement and corresponding intensity profiles are presented in Figure 3.10.

The intensity profiles were fitted with a Lorentzian function, and the resulting full widths at half maximum (FWHM) ranged between 661 nm and 720 nm. In these measurements, the spatial resolution is not continuous but is defined by the distance covered by a single camera pixel. This pixel distance limits the measurement resolution to discrete steps. Specifically, there are two selections of number of pixels: 3 pixels, corresponding to 562.5 nm on the sample, or 4 pixels, corresponding to 750 nm on the sample. To match the observed FWHM values as closely as possible, the 4-pixel setting, corresponding to 750 nm, was selected.

The previously determined width of 4 pixels was used to collect information referring to fluorescence intensity in the vicinity of the nanowire. From every fluorescence intensity map, two 4-pixel wide profiles were collected: 1) from areas where AgNWs are localized; 2) from areas with no nanowires. The intensity profiles were about 25 μm (chosen arbitrarily as distance sufficient to cover statistically significant number of points along the nanowire) in length and were omitting ends of nanowires. Fluo-

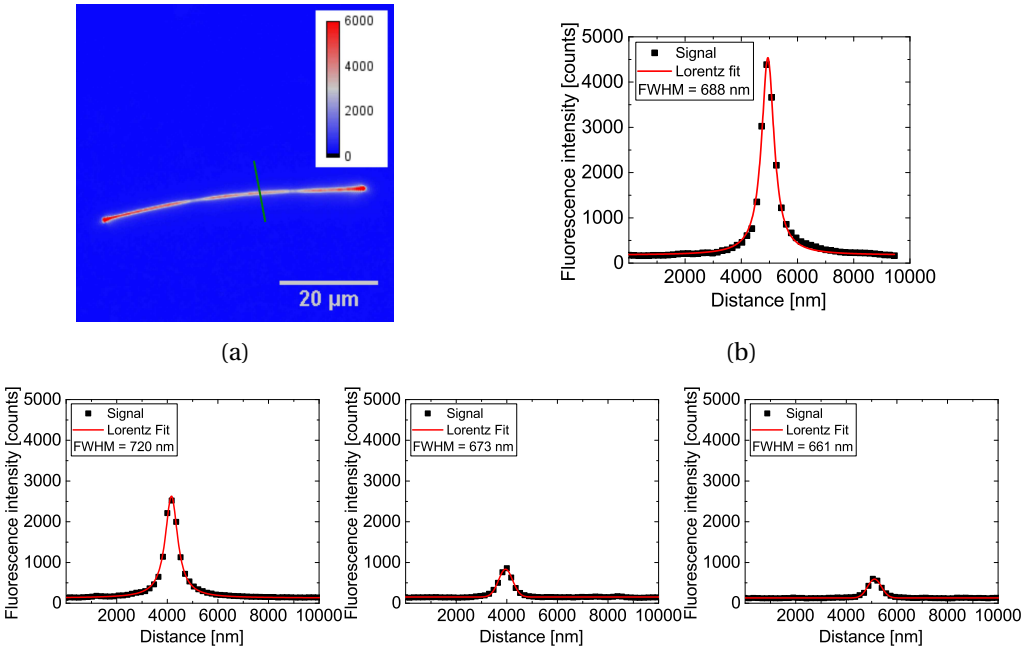

Figure 3.10: Measurements of the width of the area of the PCP fluorescence enhancement by AgNWs. (a) Fluorescence intensity map with profile perpendicular to the nanowire - green line and fluorescence intensity profiles for (a) AgNWs PVP, (b) AgNWs H_2O_2, (c) AgNWs aniline+H_2O_2, (d) AgNWs aniline. Black dots represent measured signal and red line represents fitted Lorentz function.

rescence intensity maps with marked areas (profiles) of data acquisition have been shown in Figure 3.11.

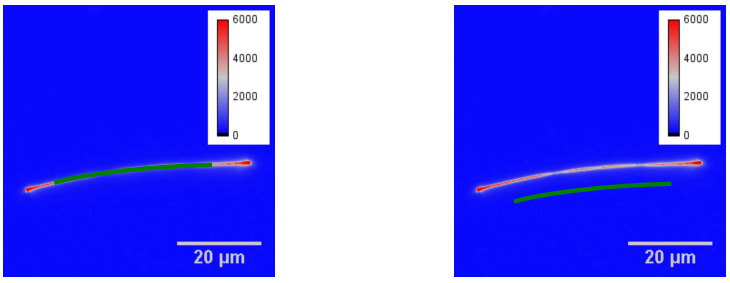

Figure 3.11: Fluorescence intensity maps with marked profiles used to collect fluorescence intensity data.(a) Area of fluorescence intensity acquisition on the nanowire marked with green line and (b) off the nanowire.

The fluorescence intensity profiles obtained from the above procedure were extracted from each fluorescence intensity map are shown in Figure 3.12.

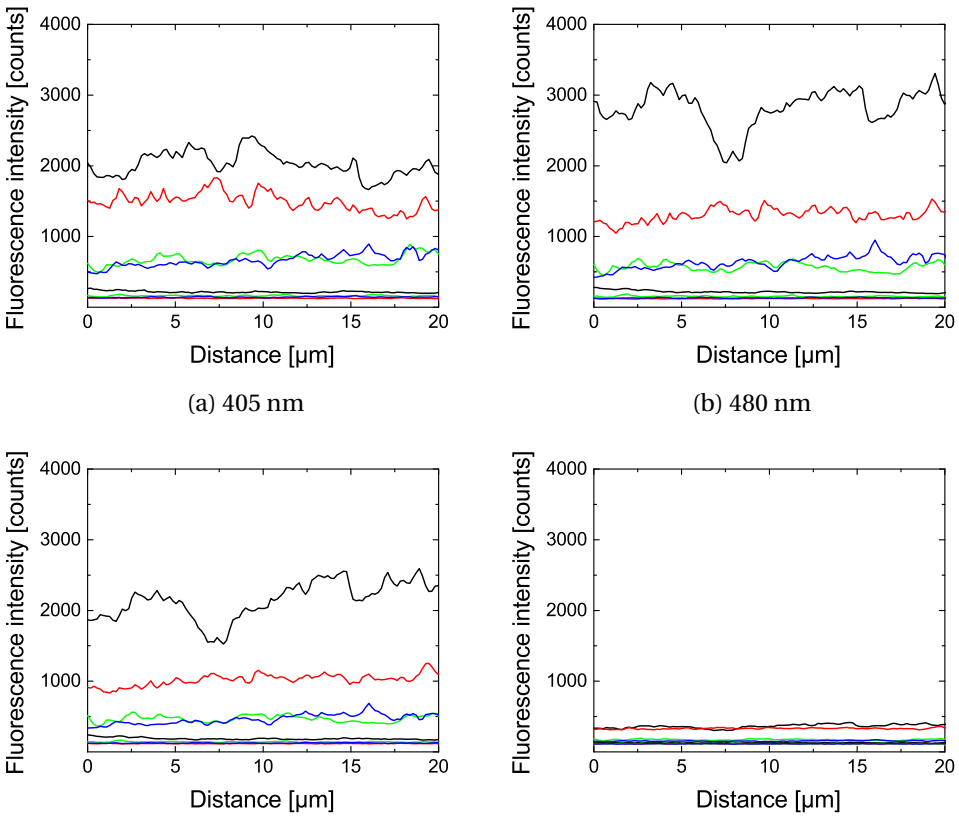

(a) 405 nm

(b) 480 nm

(c) 535 nm

(d) 630 nm

Figure 3.12: Typical fluorescence intensity profile along of AgNWs PVP(black),AgNWs H_2O_2(red), AgNWs AgNWs aniline+H_2O_2(green) and AgNWs aniline(blue) for excitation wavelength (a) 405nm, (b) 480 nm, (c) 535nm, (d) 630 nm and corresponding reference values off nanowire (lower intensity).

In correlation with fluorescence intensity maps, a higher number of counts is observed in profiles collected on nanowires comparing them to positions off the nanowires. The highest fluorescence intensity among all samples is observed for AgNWs PVP and AgNWs H_2O_2 samples. Moreover, for the 630 nm excitation wavelength, the ratio between fluorescence intensity measured on the positions of nanowires is much lower than for the other excitation wavelengths. The fluorescence intensity along the nanowire is not homogeneous, which leads to conclusion that single point is not the best estimate of fluorescence intensity observed on the nanowire, thus for further analysis whole fluorescence intensity profiles were utilized.

Finally, fluorescence enhancement factors for each nanowire were calculated by dividing the mean fluorescence intensity of the profile collected on and off the nanowire. Figure 3.13 shows histograms of fluorescence enhancement factors.

When comparing results by excitation wavelength, always the highest fluores-

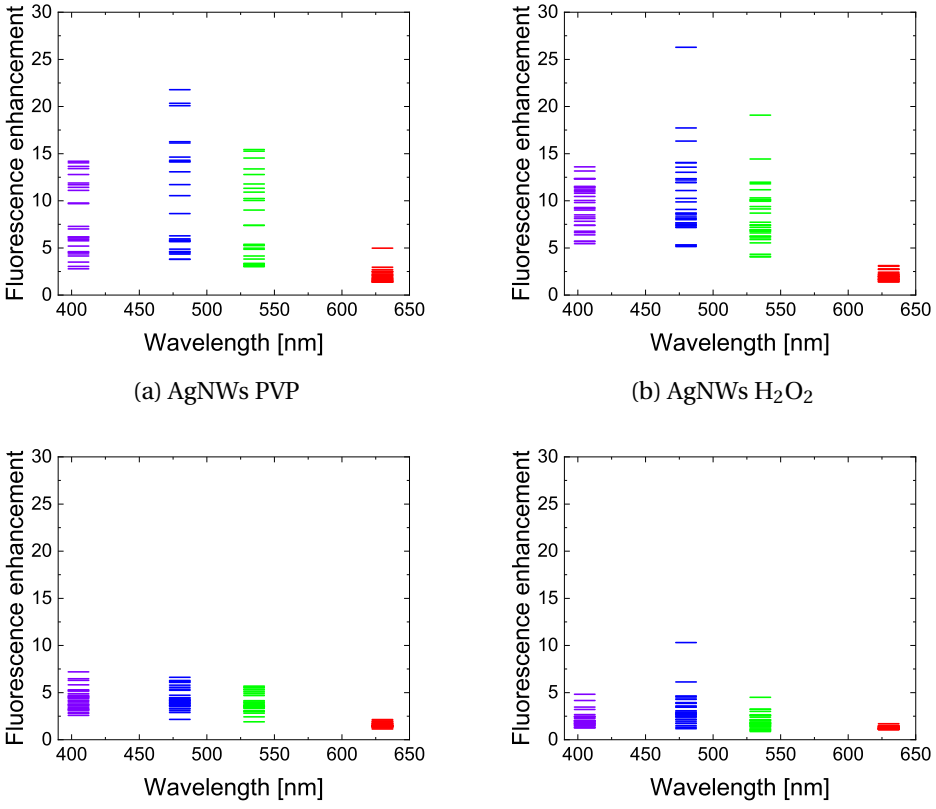

(a) AgNWs PVP

(b) AgNWs H_2O_2

(c) AgNWs aniline+H_2O_2

(d) AgNWs aniline

Figure 3.13: Histograms of fluorescence enhancements factors determined for single nanowires from each sample: (a) AgNWs PVP, (b) AgNWs H_2O_2, (c) AgNWs aniline+H_2O_2, (d) AgNWs aniline.

cence enhancement was observed for 480 nm extrication wavelength, and the lowest enhancement factor was observed for 630 nm excitation wavelength. While comparing mean fluorescence enhancement factors (EF) by samples, for AgNWs PVP (d = 76 nm) PCP fluorescence enhancement factor was from 2.0 up to 10.0 (correspondingly 630 nm and 480 nm excitation wavelength), and for AgNWs H_2O_2 (d = 78 nm) - EF from 2.0 up to 10.5. Enhancements for AgNWs aniline+H_2O_2 (d = 131 nm) were lower from 1.6 to 4.3, while for the AgNWs aniline (d = 153 nm) enhancements were the smallest among all samples from 1.3 to 3.2. Moreover, standard deviations in the samples AgNWs PVP and AgNWs H_2O_2 are much bigger from 0.7 up to 5.8 compared to AgNWs aniline+H_2O_2 and AgNWs aniline from 0.2 to 1.8, indicating that for thin nanowires, fluorescence enhancement strongly depends on their diameter. The lowest enhancement among all samples is observed at the 630 nm excitation wavelength. Higher fluorescence enhancement has been observed for the 535 nm excitation wavelength, while the highest values of fluorescence enhancement are mea-

sured for the 405 and 480 nm excitation wavelength. Mean fluorescence enhancement for all samples is presented in Table 3.1.

Sample \ excitation wavelength	405 nm	480 nm	535 nm	630 nm
AgNWs PVP	8.1± 3.8	10.0± 5.8	7.8± 4.3	2.0± 0.7
AgNWs H_2O_2	9.5± 4.4	10.5± 4.4	8.4± 3.2	2.0± 0.5
AgNWs aniline+H_2O_2	4.3± 1.2	4.3± 1.1	4.0± 1.0	1.6± 0.2
AgNWs aniline	2.2± 0.8	3.2± 1.8	2.0± 0.8	1.3± 0.2

Table 3.1: Table of mean fluorescence enhancement with standard deviation obtained from 30 AgNWs measurements, for each sample measured in a layer of PVA.

To compare the influence of excitation wavelength on fluorescence enhancement between the samples, they were normalized (divided) by the mean fluorescence enhancement determined for 630 nm excitation wavelength. Such mean relative fluorescence enhancement factors are presented in Figure 3.14.

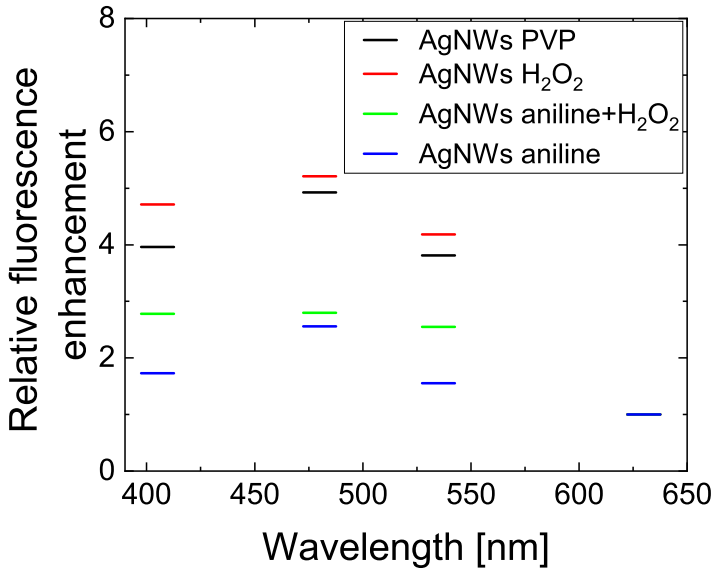

Figure 3.14: Mean relative fluorescence of PCP enhancement measured for each sample in a layer of PVA.

The highest relative fluorescence enhancements were observed for 480 nm excitation wavelength with slightly lower values for 405 excitation wavelength and once again lower values for 535 nm excitation wavelength. As one may predict, these values follow the extinction spectrum of AgNWs. The only difference is the highest relative fluorescence enhancement observed for 480 nm excitation wavelength, while the highest extinction coefficient for recorded spectrum (Figure 3.5) of AgNWs is present

for 400 nm wavelength. That redshift is most likely caused by higher refractive indices of AgNWs in sample (glass and PVA) than in water, resulting in a redshift of the frequency of AgNWs LSPR. As one may expect, the graph of relative fluorescence enhancement follows the shape of the extinction spectrum of AgNWs, with the highest values in the blue region of spectrum and lowest in the red region of spectrum. For AgNWs aniline and AgNWs aniline+H_2O_2 samples, relative fluorescence enhancement reaches values up to 3, while for AgNWs PVP and AgNWs H_2O_2 these values are almost two times higher. These are similar features as seen in their extinction spectra, where AgNWs PVP and AgNWs H_2O_2 have much lower scattering cross sections in the red region compared to the blue region. This indicates that AgNWs with smaller diameters have stronger dependency between enhancement factor and excitation wavelength. This shpws the highest fluorescence enhancement for nanowires with small diameters and the lowest fluorescence enhancement for nanowires with big diameters[131].

3.3.2 Computer modelling of light scattering by AgNWs

COMSOL Multiphysics and its RF module have been used to solve Maxwell equations in the frequency domain with the finite elements method (FEM) (Described in detail in Section **2.1.8**). The primary purpose was to simulate the scattering of electromagnetic waves by silver nanowire. The simulations were conducted for varying diameters of nanowires and excitation wavelengths corresponding to the ones used in experiments (405 nm, 480 nm, 535 nm, 630 nm). The result of such simulations is electric field distribution in the computational domain. Examples of electric field distribution in logarithmic scale around 40 nm and 200 nm wide nanowires are presented in Figures 3.15 and 3.16. In all cases, the electric field is highly localized in the corners of nanowires for all excitation wavelengths. The field distribution strongly depends on the diameter of the nanowire and is weakly influenced by the excitation wavelength. However, the excitation wavelength affects the absolute values of the electric field. The highest electric field intensity of about 300 V/m is observed for 405 nm illumination, and the lowest for 635 nm illumination (about 10 V/m). For 40 nm diameter nanowire electric field deeply penetrates into the nanostructure, especially upon 405 nm excitation wavelength. However, for a much bigger nanowire(diameter = 200 nm), electric field penetration into the nanostructure is much weaker.

The strongest electric field and, thus field enhancement are present at the corners of the nanowires. In all diameter cases reaching about 300 V/m translating into $|E|^2/|E|_0^2 = 300^2 = 90000$ times field enhancement for 405 nm illumination. Nevertheless, such high values are only observed in the close vicinity of the corners, while much lower values are observed around the flat edges of the nanowires. As one may expect, shifting towards longer wavelengths and thus moving away from the localized plasmon frequency leads toward weaker field enhancement. For a 40 nm wide nanowire and 630 nm excitation wavelength maximum field value is 8 V/m which

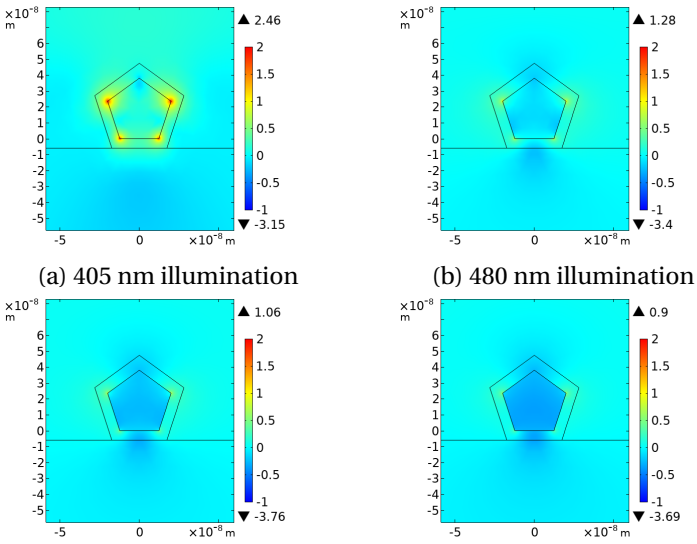

(a) 405 nm illumination (b) 480 nm illumination

(c) 535 nm illumination (d) 630 nm illumination

Figure 3.15: Logarithmic electric field distribution around 40 nm wide silver nanowire, color range has been limited for clarity (maximum values present in simulated are marked with an arrow above color scale) for (a) 405 nm illumination, (b) 480 nm illumination, (c) 535 nm illumination, (d) 630 nm illumination.

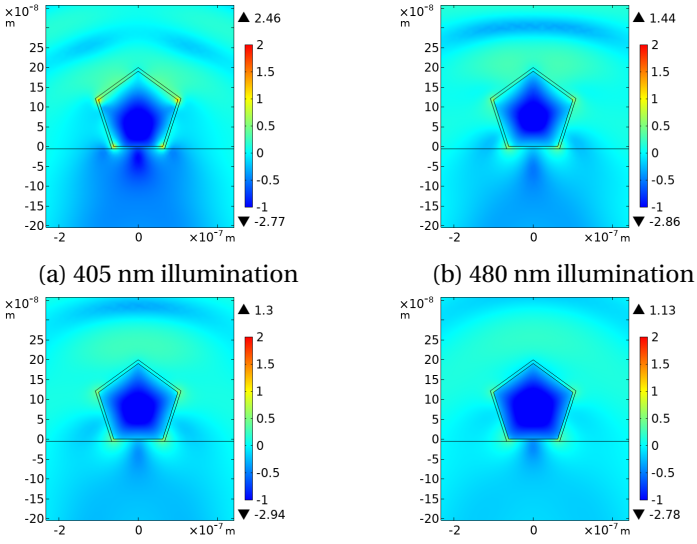

(a) 405 nm illumination (b) 480 nm illumination

(c) 535 nm illumination (d) 630 nm illumination

Figure 3.16: Logarithmic electric field distribution around 200 nm wide silver nanowire, color range has been limited for clarity (maximum values present in simulated are marked with an arrow above color scale) for (a) 405 nm illumination, (b) 480 nm illumination, (c) 535 nm illumination, (d) 630 nm illumination.

translates into 64 times field enhancement. For wider nanowires, slightly stronger fields are observed; for a 200 nm wide nanowire, it is 13.7 V/m, so the field enhancement is around 190. Therefore molecules near corners of nanowires should be exposed to much stronger electric field than molecules elsewhere. Moreover, this electric field enhancement depends on excitation wavelength reaching maximum for 405 nm excitation. The diameter of the nanowire has elatively small impact on the electric field intensity around its corner.

PCP is a big fluorophore (4 nm) with a complicated structure. Its size is not negligible at this scale and thus cannot be approximated as a point. Moreover, the fluorophores have spatial distribution inside the protein structure, meaning that each one can experience order of magnitude differences in electric field strength. To make it even more complicated, there is no data available about the structure of PCP conjugated with streptavidin, making it even harder to determine its direct orientation and distance relative to the nanostructure. On the other hand size of PCP and averaging of the electric field should effectively disregard the rapidly fluctuating electric field around the nanostructure, where field enhancement varies sharply in space[132]. Thus it is not essential to concentrate on direct calculations of electric field enhancement experienced by fluorophores in the vicinity of the nanostructures but instead on the trends of the mean electric field around the nanostructure, which should correlate with experimental observations of excitation wavelength-dependent fluorescence enhancement.

For mean electric field calculations, only the area of PVP coating has been used in calculations as presented in Figure 3.17. This area consists of all points up to 6

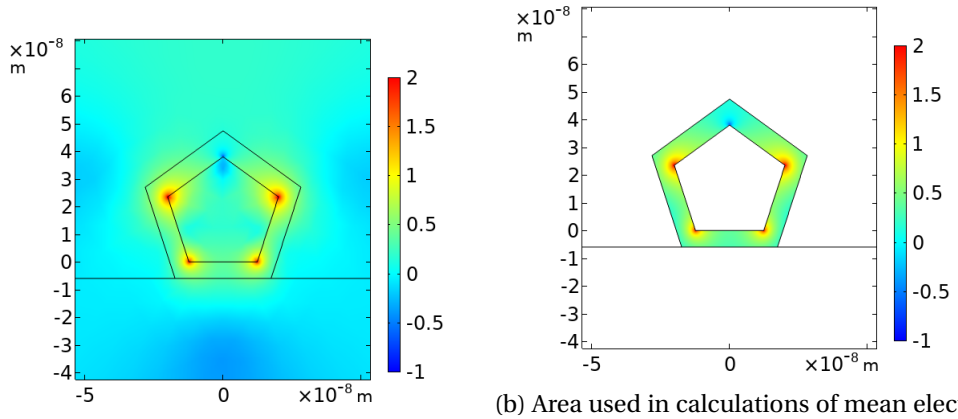

(a) Overview of the computational domain.

(b) Area used in calculations of mean electric field enhancement.

Figure 3.17: Logarithmic electric field distribution around the silver nanowire, with the area used in calculations for mean electric field enhancement of the nanowire, Showing (a) overwiev of the computational domain and (b) area used in calculations of mean electric field enhancement.

nm apart from the surface of the nanowire. It is slightly more than the size of PCP; notwithstanding, it has to be noted that in this study, the conjugate of PCP and strep-

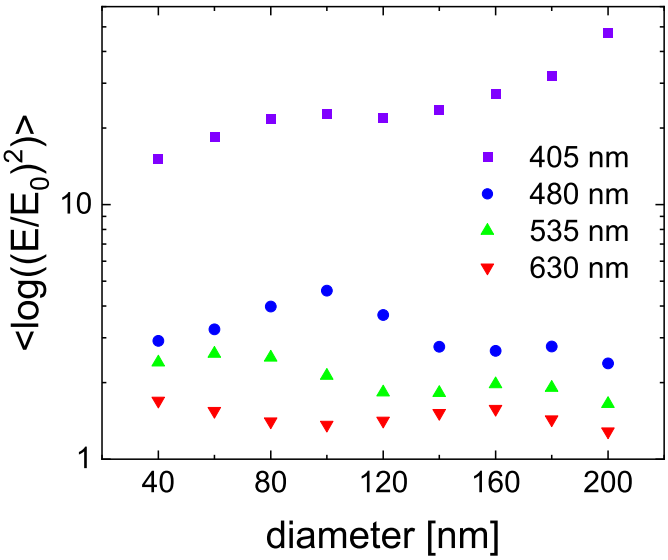

Figure 3.18: Calculated mean electric field enhancement around the silver nanowire.

tavidin has been used. Streptavidin's size itself is similar to the size of PCP. To conclude, such selection of area should correspond localisation of PCP in its conjugate with AgNWs. To quantitatively estimate field enhancement around the nanowire, mean-field enhancement around the nanowire was calculated. Mean-field enhancement was obtained by averaging field enhancement from each of the mesh points of the PVP layer. Results are presented in Figure 3.18. As one may expect, the highest field enhancements are observed at the excitation of wavelengths corresponding to the frequencies of LSPR. For 635 nm, excitation enhancements are around 1.5; for 535 nm around 2; and for 480 nm around 3. For 405 nm excitation wavelength enhancements are an order of magnitude higher, ranging from 10 to 50 fold. Finally, there is no linear relation between field enhancement and nanowire size. There are some diameters for which maximum enhancement is observed, nonetheless, these maxima occur at a different diameter depending on the excitation wavelength. Nevertheless, they shift with the change of wavelengths, and the differences are not big.

From the results of such simulations, it is possible to calculate the extinction cross-section by integrating the Poynting vector over the surface of the nanowire and the absorption cross-section by integrating heat losses over the volume of the nanoparticle. The scattering, absorption, and extinction cross-section of a 100 nm wide silver nanowire are presented in Figure 3.19. In simulated scattering cross-sections, there are three distinct plasmon resonances(Corresponding field distributions are presented in Appendix Figure 3.49):

- Associated with dipole plasmon resonance around 450 nm.

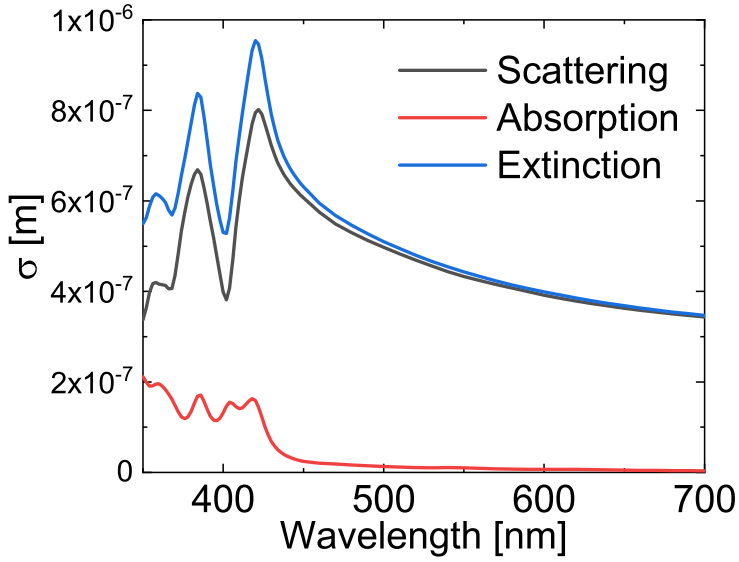

Figure 3.19: Simulated spectrum of 100 nm wide silver nanowire fully embedded in water.

- Associated with quadrupole plasmon resonance around 400 nm.
- Almost indistinguishable, around 360 nm associated with octupole resonance.

It is worth noting that theoretical scattering spectra are red-shifted relative to experimental ones (Figure 3.19). Many factors might cause this, but the most probable is a mismatch between the literature refractive index of silver and the refractive index of silver nanowires. Also, experimental extinction spectra of silver nanowires are measured in water dispersion, in which nanowires are randomly oriented and illuminated, contributing nanowires with varying diameters, which do not fully correspond to situations in simulations.

Despite these discrepancies, such simulations might give insight into spectra. The spectra of 50 nm, 100 nm, and 150 nm wide nanowires have been calculated and are presented in Figure 3.20. Both experimental and theoretical spectra have the same qualitative properties. A redshift of the spectrum is observed for bigger diameter nanowires and their spectrum is more "flat" compared to smaller diameter nanowires; also, quadrupole resonance is better pronounced in the spectra of thinner nanowires. As may be expected for such big nanostructures, scattering has a major contribution to the extinction spectrum. In the blue region of the spectrum (350-500 nm) so in the region of the strongest LSPR absorption contributes to about 25% of the whole extinction spectrum. In the red part of the spectrum absorption contribution is negligible, and the spectrum's shape is fully determined by scattering. At the same time values of absorption cross section are higher for nanowires with bigger diameters. This agrees with experimental observations. Increasing the

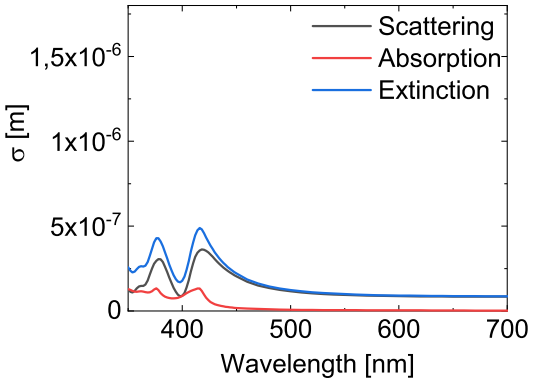

(a) 50 nm

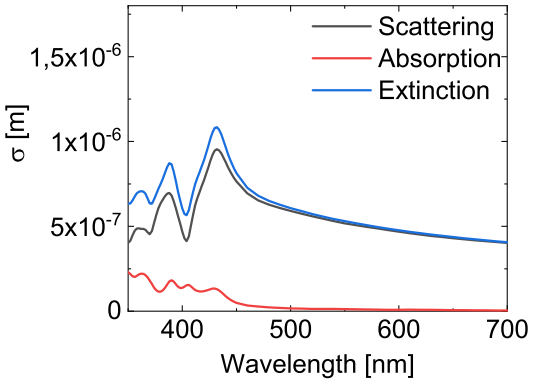

(b) 100 nm

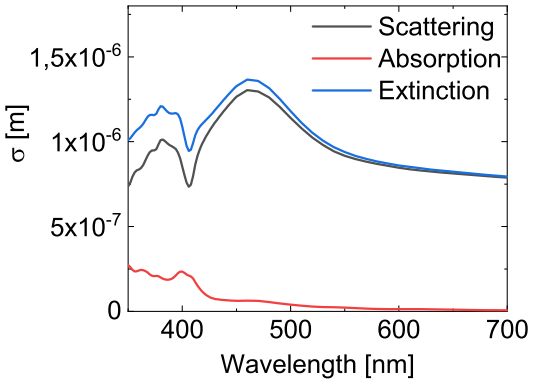

(c) 150 nm

Figure 3.20: Simulated scattering cross sections of nanowires in the PVA layer on the glass substrate with varying diameter, for (a) 50 nm, (b) 100 nm, (c) 150 nm wide silver nanowire.

diameter of nanowires shift relative intensity of dipole and quadrupole resonance. For nanowires with bigger diameters dipole resonance is more intense, and characterized with a much stronger scattering in the red part of the spectrum.

3.3.3 SPP propagation in AgNWs

Although SPPs can be excited in a wide range of electromagnetic spectrum, in this work only 635 nm excitation wavelength is used due to the following reasons. When blue light is utilized for excitation, then high SPP damping is observed, resulting in small values of L_{SPP}[131] and high uncertainties in the determination of their values. On the other hand, in the infrared red L_{SPP} reaches much greater values at the cost of much more complicated and expensive equipment. Additionally, the selected 635 nm wavelength has the advantage that PCP might be used again as a probe of electric field intensity.

For nanowires waveguiding properties studies two-objective microscope was used (Section **2.1.4**). Firstly, the nanowire of interest was localized using a reflection image of the sample. In the second step tightly focused laser beam was aimed at one of the nanowires' ends as shown in Figure 3.21, then fluorescence intensity maps were recorded (Figure 3.22). Determination if laser is focused at the end of the nanowire is

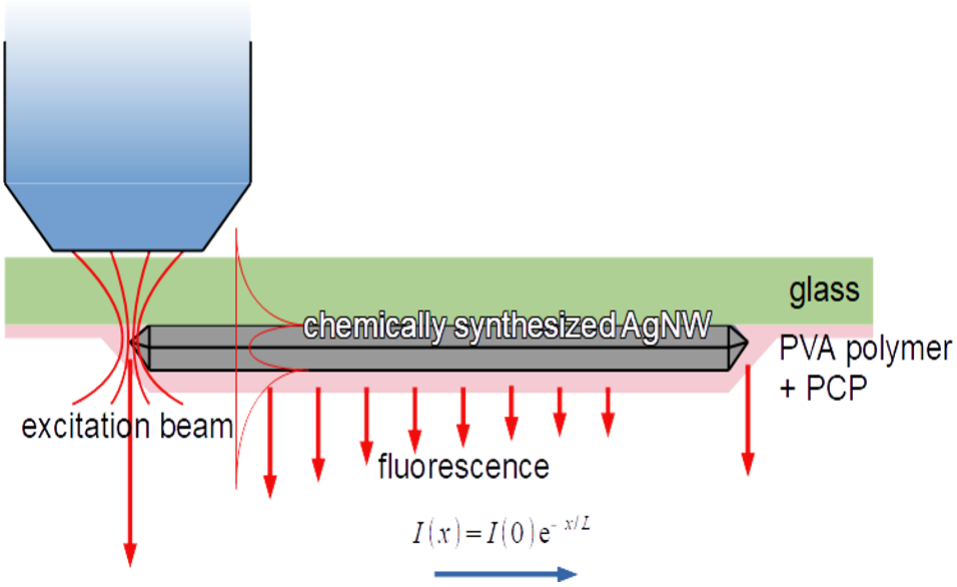

Figure 3.21: Scheme of experiment where propagating SPP modes are excited in silver nanowire. Reprinted with permission from[131]. Copyright 2025 American Chemical Society.

straightforward, as even slight movement of the laser results in a significant decrease in fluorescence intensity along the nanowire. In the typical map, a bright elongated shape which position correlates with AgNWs is seen. The nanowire's end illuminated

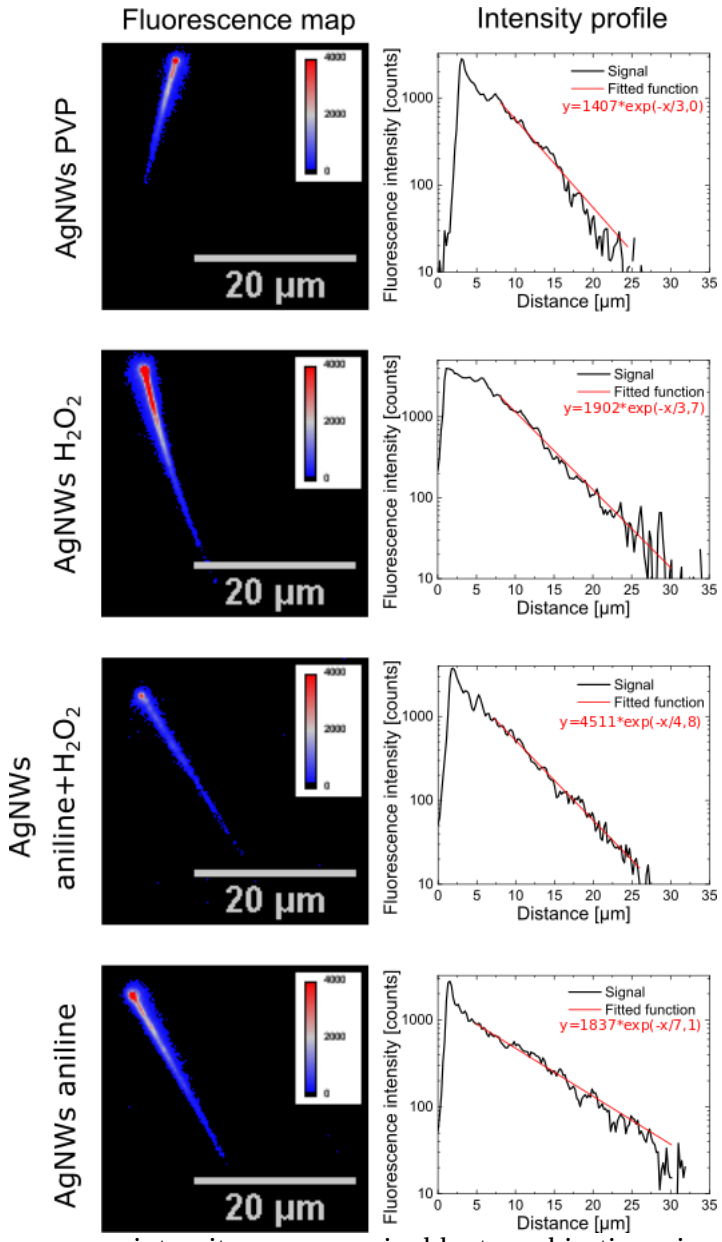

Figure 3.22: Fluorescence intensity maps acquired by two objective microscope when the laser was focused on the end of the nanowire, with corresponding fluorescence intensity profiles along the nanowire and fit function.

by the laser is the brightest point, and the fluorescence intensity is fading away along the nanowire. Furthermore, a weak fluorescence signal is observed in areas close to the nanowire end illuminated by laser to 1 µm apart from the nanowire. The emergence of such bright lines, which correlate with the positions of nanowires, indicates that SPP in AgNWs can efficiently excite the emission of PCP complexes in their close

vicinity. The decrease in the fluorescence intensity of PCP further apart from the illuminated nanowire's end indicates a decrease in electric field intensity along the nanowire. This effect was observed in all four types of samples studied.

The origin of fluorescence around the nanowire end illuminated by laser has two possible explanations:

- electric field around the nanowire is so strong that even though it is decaying exponentially from the surface of the nanowire, electric field is still sufficient to induce fluorescence of PCP in a measurable way.
- energy is transferred between PCP molecules in the layer by the Förster Resonance Energy Transfer(dipole-dipole coupling between two chromophores).

To quantitatively determine L_{SPP} in nanowires 25 fluorescence intensity maps were measured for each sample. Then from each fluorescence intensity map intensity profile along the nanowire was extracted and fitted with monoexponential decay function in the form:

$$I(x) = I_0 e^{\frac{-x}{L_{SPP}}} \tag{3.1}$$

where x stands for position along the NW and L_{SPP} is a parameter associated with the damping of the SPP[107].

The histograms of determined L_{SPP} for each sample are presented in Figure 3.23. The shortest plasmon propagation lengths were observed for AgNWs PVP and AgNWs H_2O_2 samples (4.1 and 3.2 µm respectively). For the sample with wider nanowire - AgNWs aniline+H_2O_2 mean L_{SPP} was equal to 5.1 µm, and the highest mean length of plasmon propagation = 6.2 µm was recorded for the sample with the highest mean diameter. These results show weaker SPP damping in nanowires with bigger diameters, thus greater LSPP propagation lengths.

3.3.4 Numerical simulations of AgNWs waveguiding properties

Comsol Multiphysics and its RF module have been used to solve Maxwell equations in the frequency domain with the finite elements method (FEM) (Section **2.1.9**). The primary purpose was to simulate possible modes of light propagation in the selected configuration. Mathematically speaking, it is assumed that the solutions of the Maxwell equations for light propagating in the z-direction have the form:

$$\vec{E}(x,y,z) = \vec{A}(x,y)e^{\gamma z} \tag{3.2}$$

where $\vec{A}(x,y)$ is cross-section amplitude profile (mode shape) and complex propagation constant $\gamma = \alpha + i\beta$; $\alpha < 0$ describes losses in the waveguide, and β describes phase[119]. The additional assumption here is that waveguide is uniform in the z direction, which reduces it to a two-dimensional problem. This finally leads to a standard eigenvalue problem where eigenfunctions are cross-section amplitude profiles

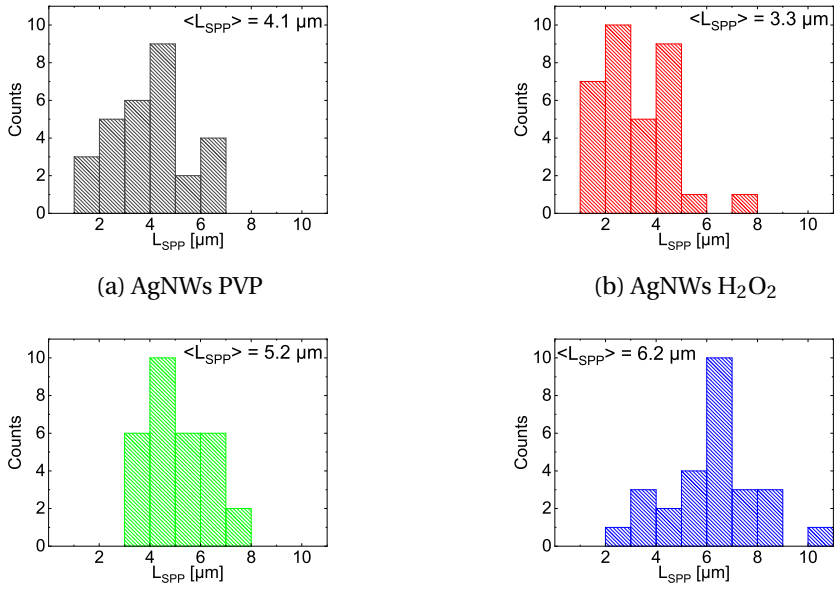

Figure 3.23: Histograms and mean values of determined L_{SPP} for 635 nm excitation measured in a spin-coated layer of PVA and PCP, for (a) AgNWs PVP,(b) AgNWs H_2O_2, (c) AgNWs AgNWs aniline+H_2O_2 and (d) AgNWs aniline.

(modes) and corresponding eigenvalues are effective refractive indices[133]. The operating wavelength of 635 nm (the same as used in experiments) was used in all simulations.

The electric field distribution of the 1st order mode (mode with the highest real value of the effective refractive index) for 40, 100, and 200 nm wide AgNW is presented in Figure 3.24. It can be seen that most of the energy is localized at the edges of the pentagon. The electric field is nearly evenly distributed around the nanowire rather than dragged into the glass substrate due to the similarity of refractive indices of PVA and glass. To get a better view of electric field distribution, the maximum electric field intensity has been fixed to 7 V/m for all nanowires, and such oversaturated field distributions are presented in Figure 3.25. It can be seen that modes have nearly cylindrical field distribution - similar to the ones observed in cylindrical waveguides; thus, they should behave similarly. Indeed with increasing nanowire diameter higher portion of the energy is dragged from the metal itself into its surroundings. From that, we should expect a lower effective refractive index and longer propagation lengths in wider nanowires.

Moreover, analysis of x and y electric field components confirms cylindrical-like mode behaviour (Figure 3.26). Discrepancies can be observed in E_x and E_y field distribution. E_x field component is entirely symmetrical to x=0 axis. However, in both cases, it can be spotted that a higher portion of the electric field is dragged into the

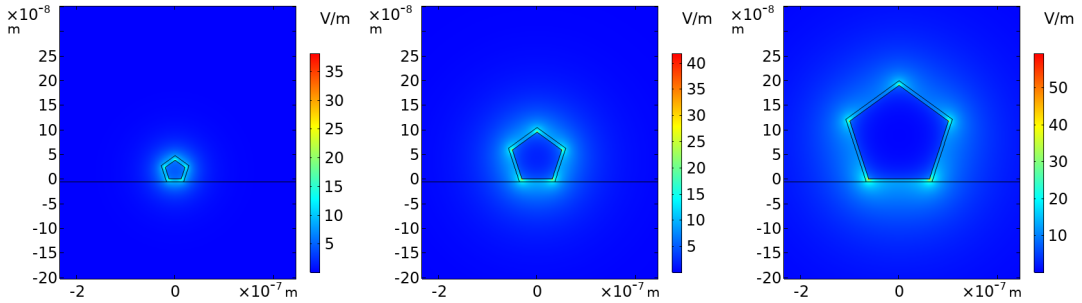

(a) 40 nm (b) 100 nm (c) 200 nm

Figure 3.24: Electric field distribution of 1st order mode for nanowires with varying diameters, for (a) 40 nm, (b) 100 nm, (c) 200 nm wide silver nanowire.

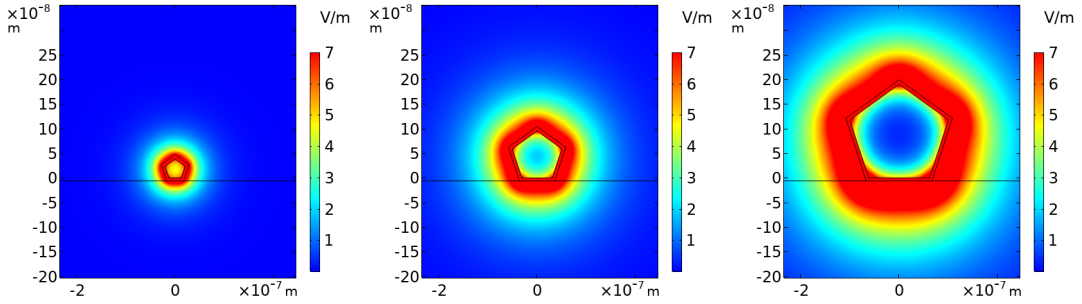

(a) 40 nm (b) 100 nm (c) 200 nm

Figure 3.25: Electric field distribution of 1st order mode for (a) 40 nm, (b) 100 nm, (c) 200 nm wide silver nanowire, while maximum value on the color bar was set to 7V/m for clarity.

glass substrate.

For this morphology and wavelength, 3 modes associated with nanowires are present. Their electric field distribution shape is similar for all diameters of nanowires. For example, the electric field distribution for a 200 nm diameter nanowire is presented in Figure 3.27. The electric field distribution follows the shape similar to the first real spherical harmonics. The 1 st order mode has nearly spherical symmetry (corresponding to spherical harmonic of l=0); 2nd and 3rd order modes have similar field distributions although rotated by 90° (corresponding to spherical harmonic of l=1). Once again they are not completely symmetrical due to a slight mismatch of the refractive index of glass and PVA.

Analysis of modes' effective refractive indices allows to determine the character of the mode (guiding or leaky). The modes' effective refractive indices as a function of nanowire diameter are presented in Figure 3.28. For the 1st order mode, the effective refractive index increases as its diameter decreases. This effect is opposite for 2nd and 3rd order modes, also the effective refractive index of 2nd a 3rd order modes is lower compared to 1st order mode. The effective refractive index of 1st order mode is always higher than glass, meaning that this mode is always guiding independently

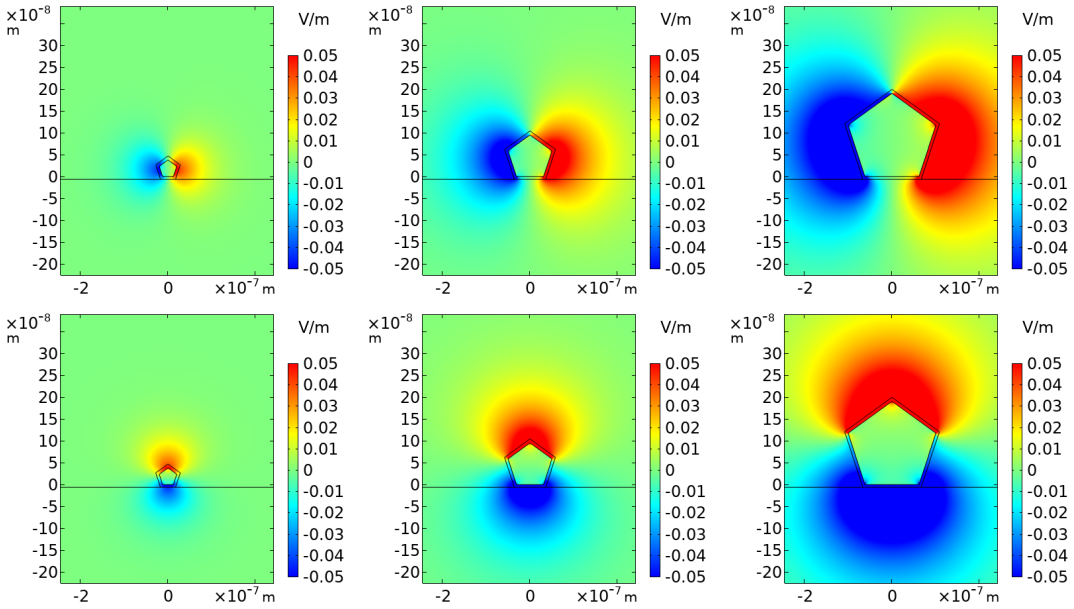

(a) 40 nm (b) 100 nm (c) 200 nm

Figure 3.26: E_x (top row) and E_y (bottom row) electric field component distribution of the 1st order mode for (a) 40 nm, (b) 100 nm, (c) 200 nm wide silver nanowire.

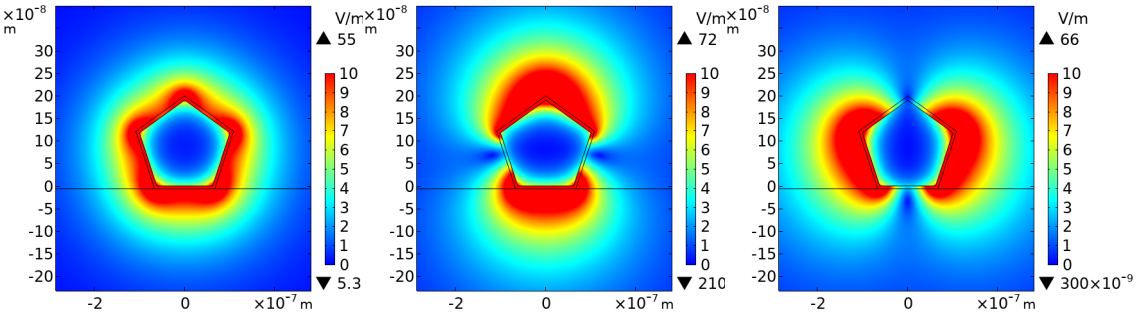

(a) 1st mode (b) 2nd mode (c) 3rd mode

Figure 3.27: Electric field distribution of SPP modes in 200 nm AgNW of (a) 1st mode, (b) 2nd mode, (c) 3rd mode, maximum value on the color bar was set to 10 V/m for clarity.

of nanowire diameter. However, the effective refractive index of 2nd and 3rd-order modes drops below a refractive index of the substrate (n=1.523) around 100 nm diameter, meaning that these modes become leaky or diminish completely for nanowires below 100 nm in diameter.

It is possible to calculate L_{SPP} from the complex propagation constant as these two values are related by dependency: $L_{SPP} = -1/2\alpha$. The L_{SPP} as a function of mode and nanowire diameter is presented in Figure 3.29.

The relationship between the electric field localized inside the metal and the ef-

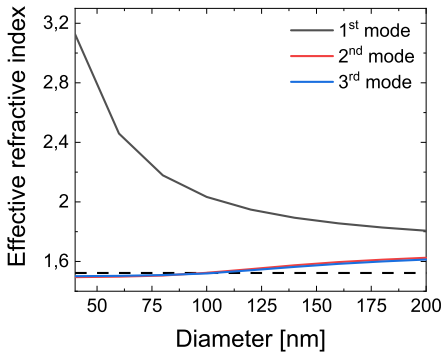

Figure 3.28: Calculated modes effective refractive index versus nanowire width. The black dashed line denotes the glass refractive index (n=1.523).

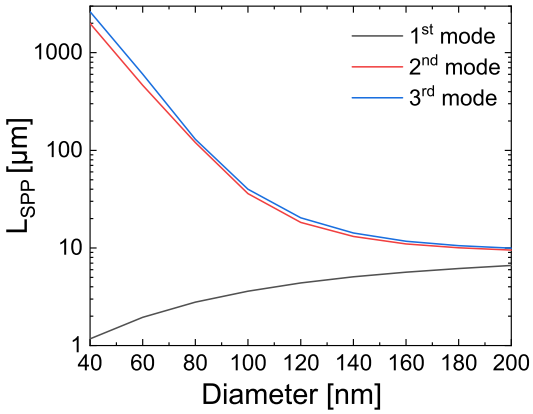

Figure 3.29: Theoretical length of plasmon propagation of different SPP modes versus nanowire diameter.

fective refractive index is transferred into predicted plasmon propagation lengths. The 1st order mode possesses much shorter plasmon propagation lengths, and it increases with increasing nanowire diameter. Conversely, the 2nd and 3rd order modes have much greater propagation lengths, increasing with decreasing diameter. The analysis of electric field distribution and L_{SPP} leads to conclusion that while increasing AgNWs diameter smaller portion of SPP electric field is dragged into metal, as a result greater L_{SPP} are observed for wider nanowires. The comparison of numerical and experimental results in which usually $L_{SPP} < 10$ µm leads to the conclusion that in the experimental setup used in this work, only 1st order mode is excited.

3.3.5 Summary

Fluorescence enhancement of four AgNWs samples was tested in a layer of PCP. In this configuration, PCP is placed at random distances and random orientations relative to the nanowires and fluorescence enhancement depends on the nanowire diameter. The highest fluorescence enhancement is observed for thin nanowires (samples AgNWs PVP and AgNWs H2O2; diameters around 75 nm) and the lowest for wide nanowires (samples AgNWs aniline+H2O2 and AgNWs aniline; mean diameters 130 and 150 nm). Moreover, the highest fluorescence enhancement was observed for excitation wavelengths matching LSPR of AgNWs (480 and 405 nm), while 630 nm exaction resulted in the lowest fluorescence enhancement. As expected, the normalized fluorescence enhancement factors reproduce the scattering spectrum observed for each AgNWs sample.

To get more insight into electric field enhancement by excitation wavelength, mathematical modelling of light scattering by AgNWs has been conducted. The simulations revealed that most of the electric field enhancement is localized in the corners of the pentagonal nanowires. Moreover, the mean electric field enhancement is the highest for 405 nm excitation wavelength and does not behave monotonically with increasing AgNWs diameter. The simulations confirmed two peaks visible extinction spectrum of AgNWs are indeed dipole and quadrupolar LSPR, and a change in AgNWs diameter shifts their relative intensity.

A home-built two-objective microscope with confocal excitation and wide-field detection was utilized to quantify SPP propagation in AgNWs in a lyaer of PCP. Statistical analysis of experiments showed that longer L_{SPP} are observed in the samples with wider nanowires. Mathematical modeling showed that propagating plasmon modes in pentagonal nanowires behave similarly to those observed in spherical nanowires. In experimental geometry at 635 nm wavelength, 3 modes are present. 2nd and 3rd modes have similar properties and the mismatch between them results from their relative orientation to the polymer/glass interface. Mode analysis shows that the first-order mode is always guiding, while the second and third-order mode becomes leaky as the nanowire diameter decreases. L_{SPP} of first-order mode increases while nanowire diameter increases, while the opposite effect is observed for second and third-order mode. Moreover the 2nd and 3rd order mode L_{SPP} is greater than for the 1st order mode. Comparison of experimental and theoretical L_{SPP} leads to the conclusion that primarily first order mode is excited in such experimental configuration.

3.4 AgNWs plasmonic properties in conjugate with PCP

The previous section describes the PCP fluorescence enhancement for PCP embedded in a layer of polymer and AgNWs. In such a configuration, inevitably, the fluorophores are placed at non-controllable, random distances from the nanostructure. Moreover, due to the about 6 nm thick polymer coating of nanowires, areas of the high electric field are unavailable for the fluorophores. These issues can be addressed by creating chemical bonds between the nanowire's surface and the fluorophore. In this work, AgNWs were first functionalized with cysteamine, forming a self-assembling thiol monolayer on their surface. Then amide bond between the cysteamine amine group and the biotin carboxylic group was created. Finally, the conjugate was formed by creating a non-covalent bond between the biotin and streptavidin part of PCP. This procedure should result in a monolayer of PCP covering silver nanowires[134]. A schematic representation of the sample configuration is presented in Figure 3.30.

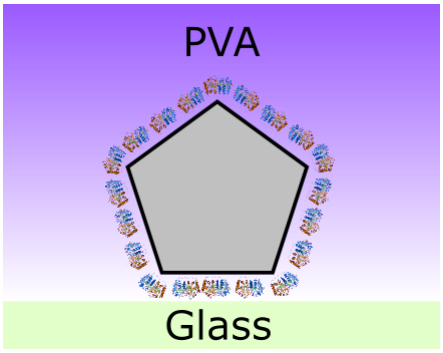

Figure 3.30: Schematic representation of sample configuration obtained by spin coating the mixture of AgNWs conjugated with PCP and PVA on a glass coverslip. The relative size between AgNW and PVP is up to scale for a 20 nm wide nanowire. The streptavidin part of the protein is not shown.

3.4.1 Conjugation of AgNWs with PCP

Chemicals

Cysteamine (97%), biotin (99%), phosphate buffer saline (PBS), TWEEN 20 (>40%) were purchased from Sigma-Aldrich. EDC (99%) was purchased from Thermo-scientific. Ethanol (96%) was purchased from Chem-pur.

PCP conjugation with AgNWs

Firstly, 0.5ml AgNWs suspension was centrifuged (2000 rpm) to remove water, then AgNWs were diluted in a 0.25 mM solution of cysteamine in ethanol. The suspension was then incubated for 2 h to efficiently cover the surface of AgNWs with cys-

teamine, which forms a self-assembling monolayer on the surface of AgNWs by creating a bond between silver and sulphur. Subsequently, both ethanol and unbound cysteamine molecules were removed by centrifugation (2000 rpm), and AgNW covered with cysteamine was diluted in 1 mM biotin and 4 mM EDC solution in PBS. The resulting suspension was kept overnight to facilitate the reaction between the amine group of cysteamine and the carboxylic group of biotin. The sample was then centrifuged again and redispersed in 0.04 mg / ml of SAv-PCP PBS solution. During this time, streptavidin conjugated with PCP created a strong noncovalent bond with biotin. After 30 minutes sample was centrifuged once again and washed with 0.05% TWEEN 20 solution to remove unspecifically bound SAv-PCP. Finally, the sample was centrifuged three times to remove TWEEN completely. Finally, AgNWs were resuspended in 0.5 ml of water and stored.

3.4.2 Sample preparation for fluorescence microscopy studies

Samples were prepared by spin-coating (1000 rpm) 20 µl droplet of solution containing: 50x diluted suspension of PCP conjugates with AgNWs, and PVA (0,04% w/w) on a glass coverslip. This procedure results in about 20-25 nm thick PVA layer (Figure 3.48) in which PCP molecules are assembled around nanowires. The distance between AgNWs and PCP is constant and the same for each fluorophore-nanoparticle pair.

3.4.3 Enhancement of PCP fluorescence by AgNWs

Typical wide-field fluorescence maps are presented in Figure 3.31. Once again, the fluorescence intensity maps were measured for 30 nanowires from each sample for 4 excitation wavelengths (630 nm, 535 nm, 480 nm, 405 nm). On the maps, there are usually bright lines (blue and red colours) that correspond to the position of AgNWs seen in the microscope in the transmitted light mode. There is no fluorescence signal in the background (areas with no nanowires visible as black), except a few single points, which occurrence can be assigned to impurities in the sample. The fluorescence intensity along the nanowire is not uniform, with a high deviance in the fluorescence intensity between the spots of the same nanowire. The highest fluorescence intensity is observed for 405 and 480 nm excitation wavelengths. Slightly lower values are observed for the 535 nm excitation wavelength and much lower values for the 630 nm excitation wavelength.

The previously described procedure for calculating the fluorescence enhancement factor cannot be applied here, as in PCP conjugate with AgNWs there is no meaningful reference to non-interacting PCP fluorescence intensity. Thus, the previously described procedure of fluorescence enhancement has been modified in the following manner: once again, 4 pixels wide fluorescence intensity profile has been acquired along the nanowire. The chosen fluorescence intensity profile along the

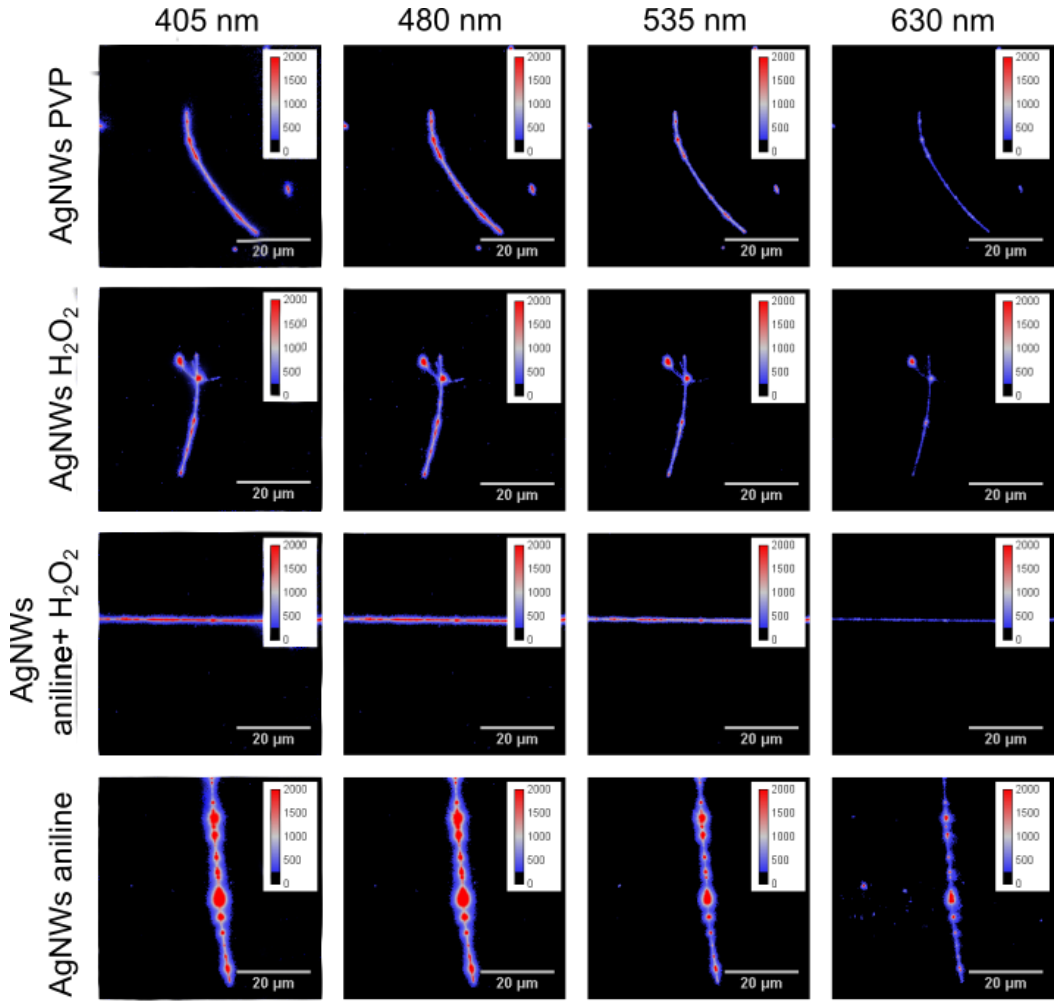

Figure 3.31: Wide-field fluorescence intensity maps of PCP. Samples were prepared by a spin-coating mixture of AgNWs conjugated with PCP and PVA onto glass coverslips. Figures present a single nanowire from each sample excited with four different wavelengths. The Colour scale bar has been fixed in all maps for clarity.

nanowire at 480 nm excitation wavelength for each sample is presented in Figure 3.32, as this wavelength yielded the highest fluorescence intensity but was selected without any particular rationale beyond that. In the intensity profile, there are signif-

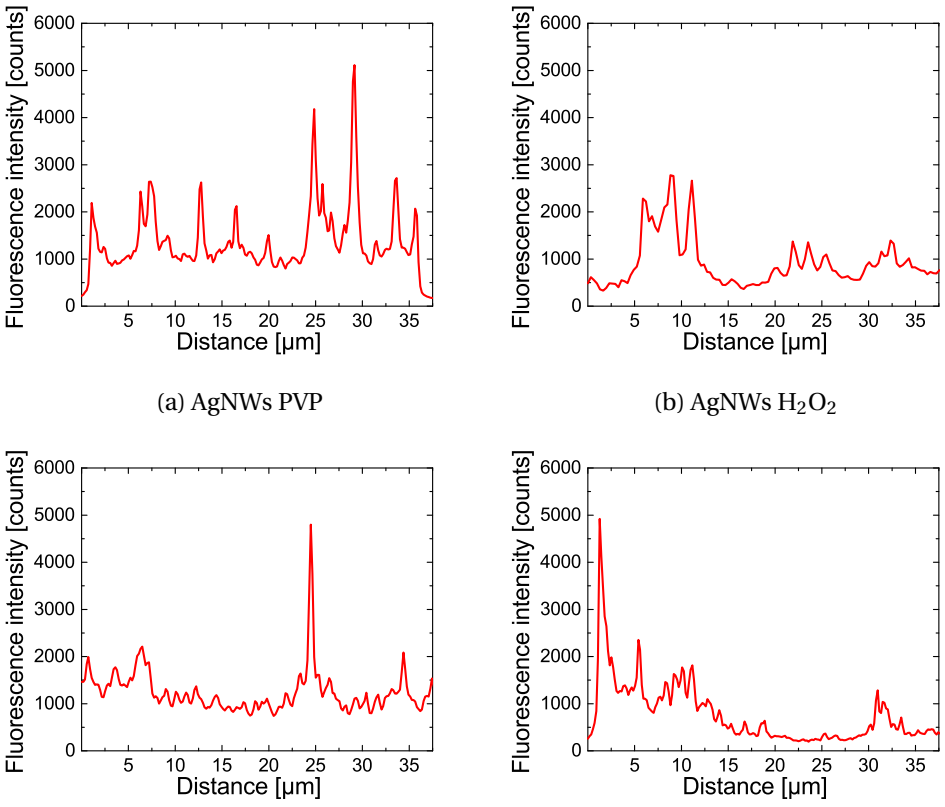

(a) AgNWs PVP

(b) AgNWs H_2O_2

(c) AgNWs aniline+H_2O_2

(d) AgNWs aniline

Figure 3.32: Fluorescence intensity profile of PCP conjugate with AgNWs acquired along the nanowire at excitation wavelength 480 nm, for (a) AgNWs PVP, (b) AgNWs H_2O_2, (c) AgNWs AgNWs aniline+H_2O_2 and (d) AgNWs aniline.

icant deviations (2-6 times the intensities larger than the mean) in the fluorescence intensity along the nanowire, and areas of high and low fluorescence intensity can be spotted. The areas of high fluorescence intensity can be attributed to unspecifically bound PCP molecules (aggregates). Nevertheless, spots with relatively low fluorescence intensity (fluorescence intensity ≈500 to 1000 counts in Figure 3.32) can also be observed along the nanowire. These spots have similar fluorescence intensity values over the length of the nanowire, which indicates formation of PCP monolayer in these spots. The agglomerates of PCP are most likely responsible for the areas of high fluorescence intensity. This claim is supported by an analysis of the fluorescence lifetimes of such areas. A typical fluorescence map of PCP at AgNWs recorded on a confocal microscope for excitation at 480 nm with fluorescence decay curves

measured for marked spots is presented in Figure 3.33.

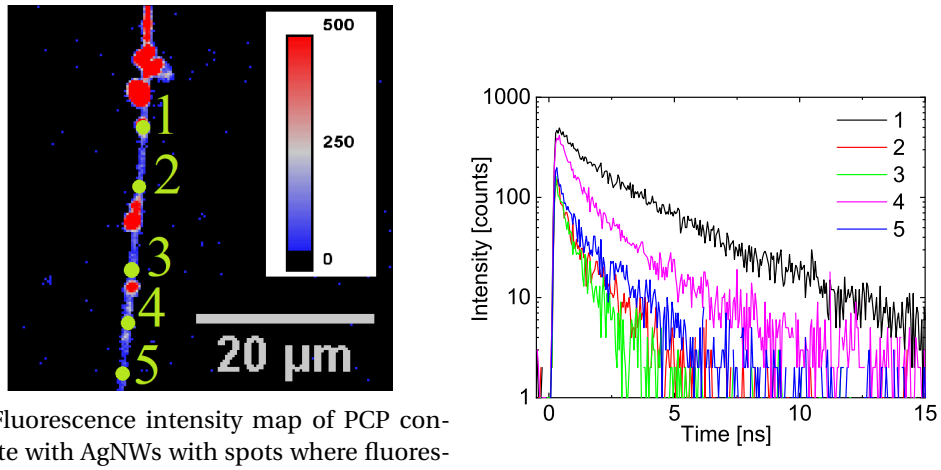

(a) Fluorescence intensity map of PCP conjugate with AgNWs with spots where fluorescence decay were measured (green spots)

(b) Corresponding fluorescence decay curves

Figure 3.33: Fluorescence intensity map of PCP conjugates with AgNWs measured on confocal microscope with fluorescence decay curves acquired for marked spots. (a) Fluorescence intensity map of PCP conjugate with AgNWs with spots where fluorescence decay were measured (green spots), (b) Corresponding fluorescence decay curves.

In the areas of low fluorescence intensity of PCP at AgNWs, much shorter lifetimes are observed than in the spots of high fluorescence intensity. The fluorescence lifetime measured in spots of high fluorescence intensity is around 4.1 ns. This value is close to the value measured for PCP in solution [135], which indicates them as spots where most PCP molecules are not plasmonically interacting with nanowires. In the spots of low fluorescence intensity, fluorescence lifetime is an order of magnitude shorter (≈0.4 ns). This significant shortening of fluorescence lifetimes and similar fluorescence intensity values observed over the nanowire, indicates that these are the spots where PCP monolayer is present and PCP molecules are strongly interacting with nanowires. This indicates that in areas of high fluorescence intensity creation of monolayer was unsuccessfull, and they can't be used in the analysis. Therefore only single point with the lowest fluorescence intensity along each nanowire has been chosen for further analysis of fluorescence intensity.

Another factor that must be considered in the analysis of fluorescence enhancement is that AgNWs diameters differ between measurements of different samples. This naturally leads to variances in the number of PCP molecules on the surface, as presented in Figure 3.34. As consequence this leads to variations in fluorescence intensity, and these absolute intensities cannot be used straightforward to calculate fluorescence enhancement factors.

Therefore, the following procedure was used to estimate fluorescence enhancement factors. Firstly, for each pair: nanowire - excitation wavelength fluorescence intensity profile was extracted. Then from each intensity profile point, the lowest

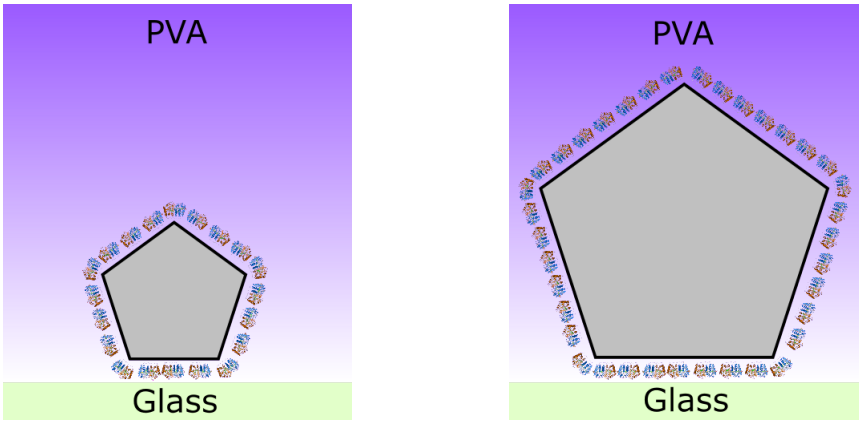

(a) 20 nm wide nanowire (b) 40 nm wide nanowire

Figure 3.34: Scheme of (a) 20 nm and (b) 40 nm wide nanowires with a varying number of PCP molecules on their surface. The schemes are up to scale for 20 and 40 nm wide nanowires.

fluorescence intensity was selected. The reason for choosing a single point is that it is problematic to choose a longer section, avoiding areas with high fluorescence intensity, and the areas where a monolayer was found have similar fluorescence intensities. The results of the measurements of the lowest fluorescence intensity for each excitation wavelength coming from 30 AgNWs of each sample are presented as histograms in Figure 3.35.

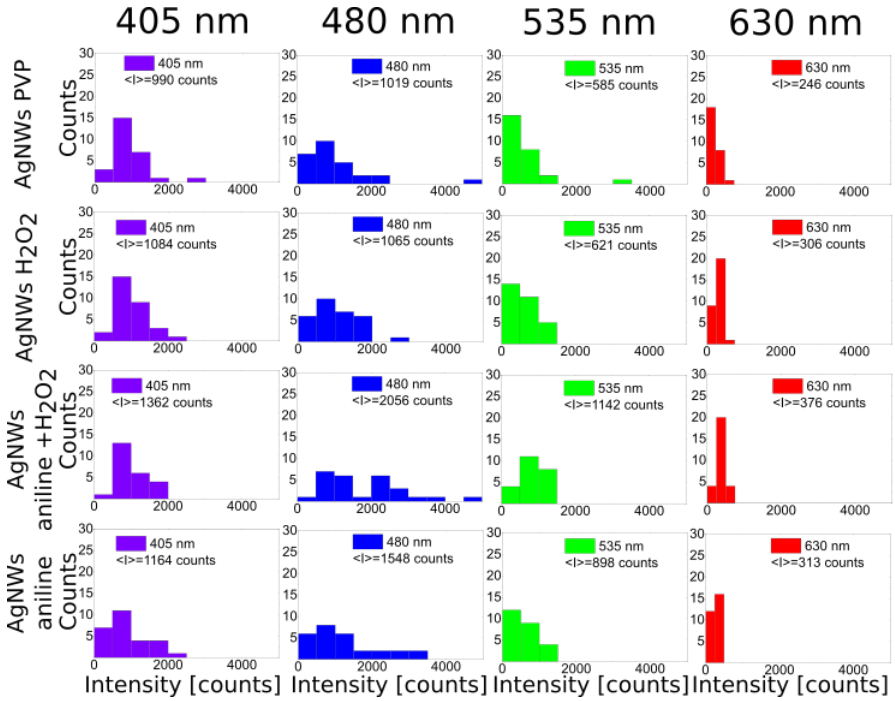

Figure 3.35: Histograms of the lowest observed fluorescence intensity for all samples.

The highest fluorescence intensity values are observed for AgNWs aniline+H_2O_2 sample followed by AgNWs aniline, AgNWs H_2O_2 and AgNWs PVP. This trend does not reflect the trend of increasing diameters, indicating that the number of PCP molecules on the surface is not the sole factor influencing fluorescence intensity. Moreover, comparing these results to ones obtained for measurements where PCP was embedded in the PVA layer, the mean fluorescence intensity between samples in the case of conjugates does not alter so much. For measurements in the layer, mean fluorescence intensity varied up to 4-5 times. In the case of the conjugate, variations in mean fluorescence intensity between samples are usually smaller than 2, which may indicate that for this type of sample, AgNWs diameter does not impact fluorescence enhancement as greatly. Moreover, it indicates that the differences in fluorescence enhancement between samples are smaller in the case of conjugate than in the case of layer.

As a first step of the analysis, the excitation-dependent fluorescence enhancement was estimated relative to 630 nm excitation wavelength, as suggested in the literature[136]. Firstly, average fluorescence intensity counts were divided by the fluorescence intensity counts at 630 nm excitation wavelength for each sample (column Relative intensity in Table 3.2). Secondly, fluorescence intensity was normalized by the respective absorption coefficient of PCP for each wavelength. Namely, it was assumed that the PCP absorption coefficient for 630 nm wavelength equals 1. It corresponds to scattering cross-sections at 405 nm $c = 9,3$, 480 nm $c = 16,9$, and 535 nm $c = 8,9$. Lastly, as the excitation power was controlled during the experiments, these values must be normalized to the number of photons incident on the sample, so 0.64 for 405 nm, 0.76 for 480, 0.85 for 535 nm excitation wavelength, and finally 1 for 630 nm excitation wavelength. Then values from the column Relative intensity were divided by corresponding absorption coefficient and number of incident photons; results are presented in the column: Relative fluorescence enhancement of Table 3.2. As a comparison, the previously obtained fluorescence intensity maps have been normalised by the same procedure (Figure 3.36).

The lowest fluorescence enhancement is observed in all samples at 535 and 480 nm excitation wavelengths. Much higher enhancement is observed at 405 nm excitation wavelength, and unexpectedly the highest fluorescence enhancement is observed at 630 nm excitation wavelength. The effect observed at 405 nm is explained by the strongest electric field enhancement for this wavelength. For the 630 nm excitation wavelength, one should expect the lowest fluorescence enhancement. However, such an effect was previously observed[137] and was assigned to the internal structure and photophysics of PCP. Upon 405, 480, and 535 nm excitation wavelength, mostly peridinin moieties are excited. On the contrary, upon 630 nm excitation wavelength, mainly $Chlorophyll\ a$ moieties are excited. They are localized in a different part of the protein than peridinin, thus experiencing different electric fields in the presence of metallic nanostructures. Electric field decays very fast(exponentially) from the surface of metallic nanostructures. So if a protein is placed very close to the

AgNWs PVP

Excitation wavelength	Average intensity	Relative intensity	Relative fluorescence enhancement
405 nm	990	4.02	0.67
480 nm	1019	4.14	0.32
535 nm	585	2.37	0.31
630 nm	246	1	1

AgNWs H_2O_2

Excitation wavelength	Average intensity	Relative intensity	Relative fluorescence enhancement
405 nm	1084	3.54	0.59
480 nm	1065	3.48	0.26
535 nm	621	2.03	0.25
630 nm	306	1	1

AgNWs aniline+H_2O_2

Excitation wavelength	Average intensity	Relative intensity	Relative fluorescence enhancement
405 nm	1362	3.62	0.60
480 nm	2056	5.46	0.42
535 nm	1142	3.03	0.39
630 nm	376	1	1

AgNWs aniline

Excitation wavelength	Average intensity	Relative intensity	Relative fluorescence enhancement
405 nm	1164	3.71	0.61
480 nm	1548	4.95	0.38
535 nm	898	2.86	0.37
630 nm	313	1	1

Table 3.2: Average fluorescence intensity, relative average fluorescence intensity, and relative average fluorescence enhancement for all samples and excitation wavelengths, measured for 30 nanowires for each sample.

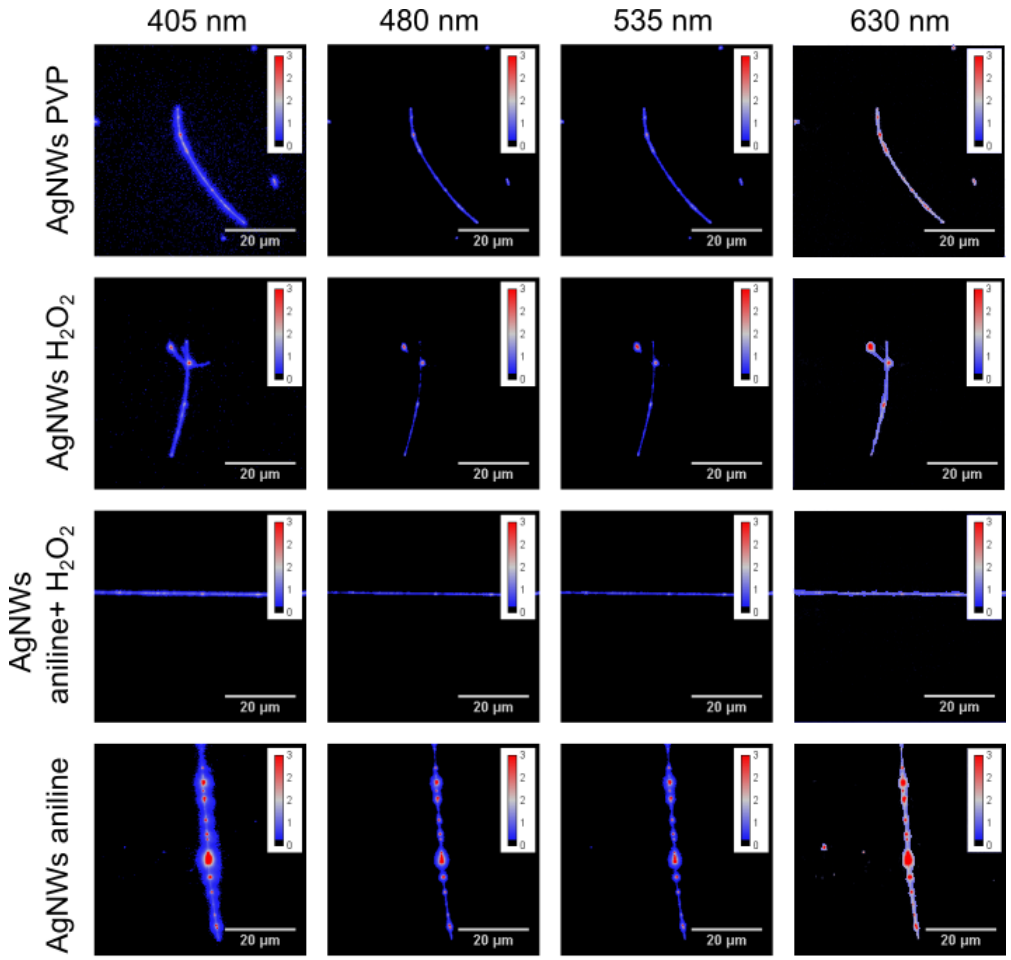

Figure 3.36: Normalised wide-field fluorescence intensity maps of PCP. Samples were prepared by a spin-coating mixture of AgNWs conjugated with PCP and PVA onto glass coverslips. Figures present a single nanowire from each sample excited with four different wavelengths. The colour scale bar has been fixed in all maps for clarity.

surface of a nanowire, then electric field can differ by the orders of magnitude in the volume of a single protein. Moreover, photo-physics processes change at 630 nm excitation wavelength as energy transfer from peridinin to $Chlorophyll\,a$ is no longer present. Results of the analogous analysis conducted in a single nanowire manner are presented in Figure 3.37. Values of relative fluorescence enhancement factors for single nanowires follow the trends observed for the whole sample. For the 630 nm excitation wavelength mean relative fluorescence was 1, for 405 nm were approximately 0.5. For 480 and 535 nm excitation wavelengths mean relative fluorescence were around 0.3. It is worth to point out that in some cases relative fluorescence enhancement for 405 nm excitation wavelength was higher than relative fluorescence

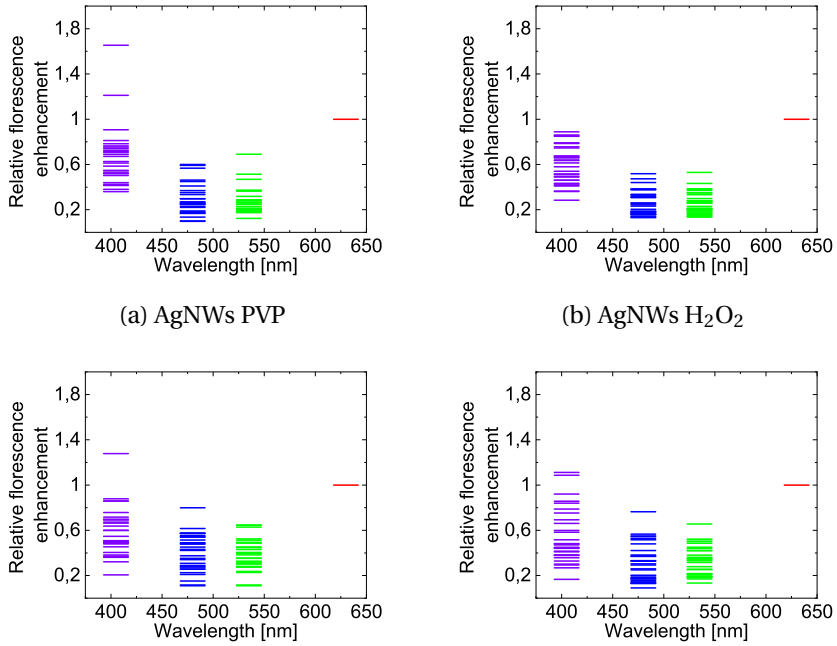

(a) AgNWs PVP

(b) AgNWs H_2O_2

(c) AgNWs aniline+H_2O_2

(d) AgNWs aniline

Figure 3.37: Histograms of relative fluorescence enhancement factors conducted for a PCP conjugates with AgNWs from each sample, for (a) AgNWs PVP, (b) AgNWs H_2O_2, (c) AgNWs AgNWs aniline+H_2O_2 and (d) AgNWs aniline.

enhancement for 630 nm excitation wavelength.

Up to this point of analysis, the only precise conclusion is that the AgNWs aniline sample shows lower fluorescence enhancement than AgNWs aniline+H_2O_2 because even if there should be more PCP molecules present in the AgNW aniline sample, the absolute fluorescence intensity is lower than for AgNWs aniline+H_2O_2 sample.

To gain more insight into fluorescence enhancement between samples, fluorescence lifetimes were measured. Figure 3.38 presents typical fluorescence decay curves for each sample. All decay curves are not linear in logarithmic scale which indicates more than one decay component. The mean intensity of decay curves can be arranged in descending order: AgNWs PVP, AgNWs H_2O_2, AgNWs aniline+H_2O_2 and AgNWs aniline, while the shortest fluorescence lifetimes are observed for AgNWs PVP and AgNWs aniline samples. Then measured fluorescence lifetimes were fitted with a bi-exponential decay function. The resulting histogram of fluorescence decay curves fitting with fitted lifetimes is presented in Figure 3.39. This resulted in two decay components: the first decay component was around 0.2 ns and a second component of around 1 ns. It is worth to be noted that the time of the shorter decay component is close to the instrument response function and to estimate its value correctly; signal deconvolution has to be conducted. Nevertheless, this study aims not to get the exact

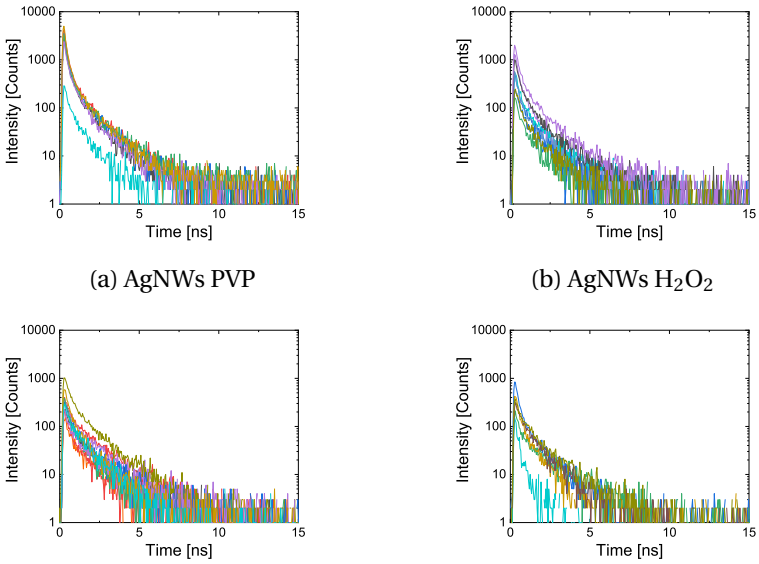

(a) AgNWs PVP

(b) AgNWs H_2O_2

(c) AgNWs aniline+H_2O_2

(d) AgNWs aniline

Figure 3.38: Fluorescence decay curves measured for PCP conjugates with AgNWs, for (a) AgNWs PVP, (b) AgNWs H_2O_2, (c) AgNWs AgNWs aniline+H_2O_2 and (d) AgNWs aniline.

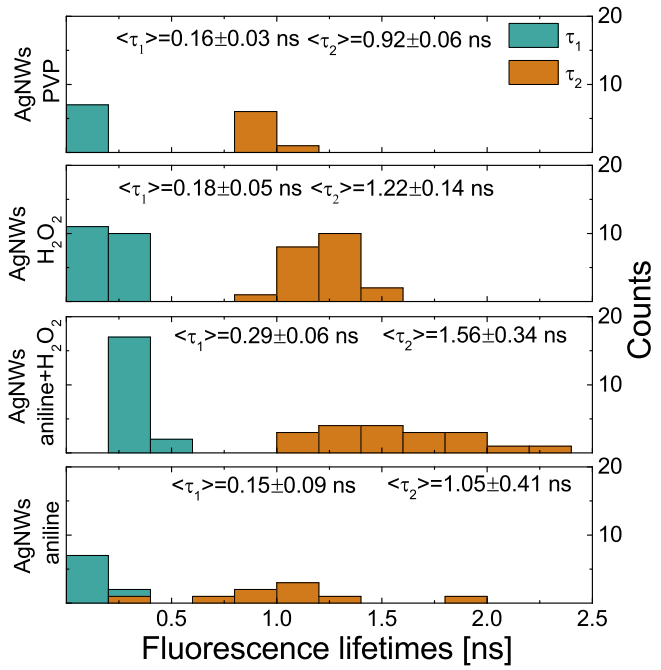

Figure 3.39: Histograms of bi-exponential fluorescence lifetimes fitted to decay curves for all samples.

value but rather to observe the trends between the samples for which such a simple analysis is sufficient. The shortest fluorescence lifetimes are obtained for AgNWs PVP and AgNWs aniline samples.

Analysis for each sample with mean fluorescence decay curves and fit functions is presented in Figure 3.40. It can be seen that there are more than two decay com-

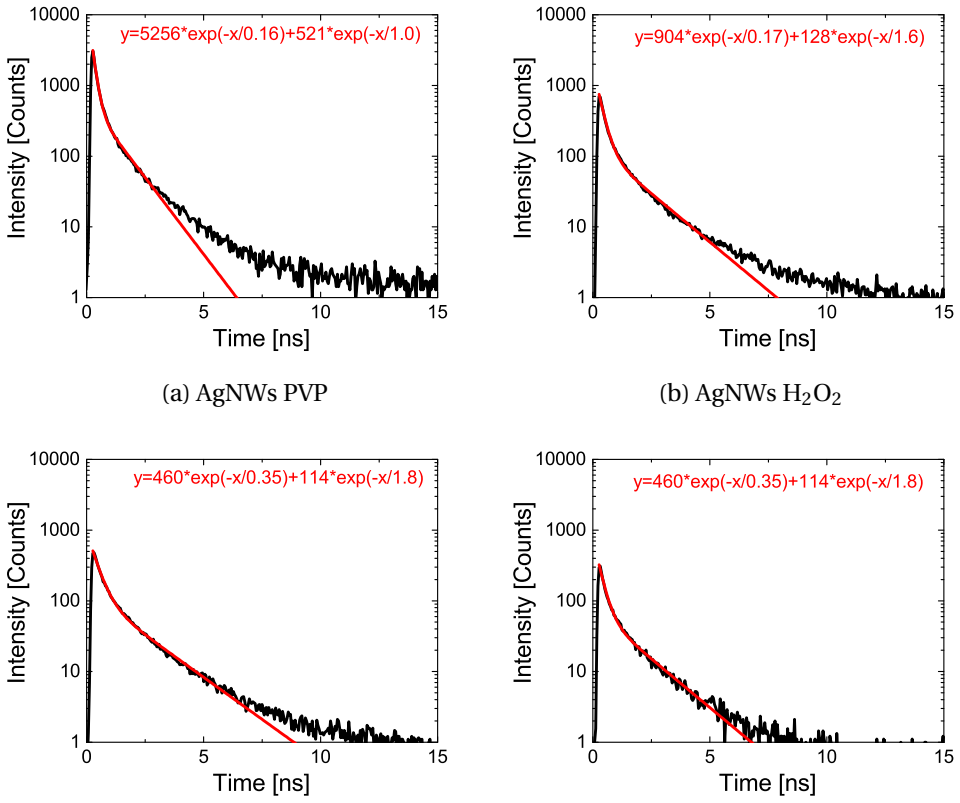

(a) AgNWs PVP

(b) AgNWs H_2O_2

(c) AgNWs aniline+H_2O_2

(d) AgNWs aniline

Figure 3.40: Mean fluorescence decay curves with fit functions measured for PCP conjugates with AgNWs, for (a) AgNWs PVP, (b) AgNWs H_2O_2, (c) AgNWs AgNWs aniline+H_2O_2 and (d) AgNWs aniline.

ponents. However, the initial intensity of these additional decay components is low. Ranging from about 30 counts for AgNWs PVP sample to 3-4 counts for AgNWs aniline. These values are too low for statistically significant fit, thus each curve was fitted with only 2 decay components. For AgNWs PVP $\tau_1 = 0.16$ and $\tau_2 = 1.0$, for AgNWs H_2O_2 $\tau_1 = 0.17$ and $\tau_2 = 1.6$, for AgNWs aniline+H_2O_2 $\tau_1 = 0.35$ and $\tau_2 = 1.8$ and for AgNWs aniline $\tau_1 = 0.25$ and $\tau_2 = 1.6$. Fluorescence decay times for mean decay curves follow the trends observed for single nanowires.

However, more than this analysis is required to estimate fluorescence enhancement between samples. Metal-fluorophore interactions have an ambiguous influ-

ence on fluorescence. On the one hand, they may lead to fluorescence enhancement. However, they may lead to fluorescence quenching. Both of these processes are associated with the shortening of the fluorescence lifetime. To solve this issue comparison of times after which fluorescence intensity value drops by a factor of 1/e and integrated areas of intensities below transient curves has been done for semi-qualitative analysis. The results are plotted in Figure 3.41. The shortest lifetimes

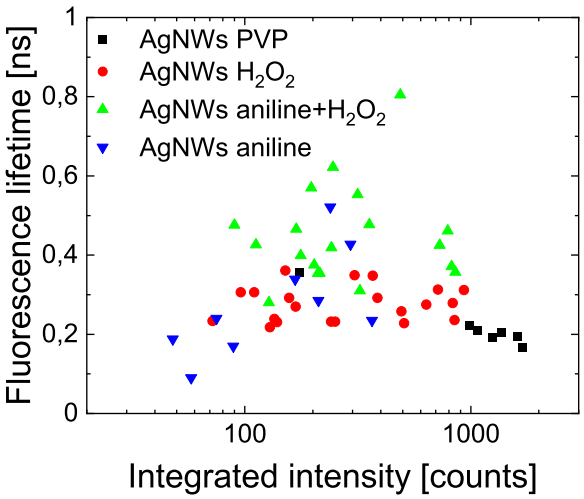

Figure 3.41: Scatter plot of times after which fluorescence intensity drops to 1/e of its initial value versus integrated intensity of fluorescence decay curve.

are observed in curves with the highest and lowest integrated fluorescence intensity, whereas the longest lifetimes are observed in curves with medium integrated intensity values. The high span of observed values for integrated intensity suggests dramatic changes in the nature of metal-fluorophore interactions. For AgNWs PVP sample radiative processes dominate, and for AgNWs aniline non-radiative processes dominate. For AgNWs aniline+H_2O_2 radiative processes have smaller contributions, and non-radiative processes are yet not dominating. Such dependencies are more straightforward to observe in TCSPC(Time correlated Single Photon Counting) experiments than in typical wide-field. In TCSPC experiments, fluorescence quantum yield is one of the dominating factors in the integrated intensity. At the same time, more factors contribute to observed fluorescence intensity in wide-field experiments (e.g., fluorescence lifetime). From such analysis, one may conclude that the highest fluorescence enhancement should be observed for AgNWs PVP sample; however, it only correlates with the results of wide-field experiments. To conclude these considerations, up to some nanowire's diameter, diameter does not affect fluorescence intensity of PCP conjugate with nanowire, and other factors have a much higher impact. After exceeding this nanowire diameter value, fluorescence intensity drops due to the strong influence of quenching, most likely due to the coupling between excited

PCP and SPP modes in the nanowire, which results in a decrease in fluorescence enhancement.

3.4.4 AgNWs waveguiding properties

This section studied whether or not the chemical modification of AgNWs surface influences their waveguiding properties. In general, PVP replacement with another organic molecule should not significantly affect their waveguiding properties, as this only shifts the refractive index of the surrounding medium. Nevertheless, chemical reactions at the surface usually lead to the surface atoms' rearrangement. Change in surface morphology may lead to serious concerns regarding AgNWs waveguiding properties after surface modification. This effect length of plasmon propagation of PCP conjugates with AgNWs was studied. Fluorescence intensity maps of SPP propagation of such conjugates and corresponding intensity profiles are presented in Figure 3.42.

The fluorescence intensity maps of PCP conjugates with AgNWs look similar to ones obtained in a layer of PVA and PCP (Figure 3.22) although few disparities can be spotted. In the case of PCP conjugates with AgNWs fluorescence intensities were lower, with higher variance in intensity along nanowires due to PCP aggregates. Nevertheless, it was still feasible to determine L_{SPP} in PCP conjugates with AgNWs. The same measurements as described in **3.3.3 SPP propagation in AgNWs** were done for 25 nanowires from each sample and gathered as histograms in Figure 3.43. Additionally for convenience, the results from measurements in the layer (Figure 3.23) were plotted on the histograms as purple bars. Among 3 samples (AgNWs H_2O_2, AgNWs aniline+H_2O_2 and AgNWs aniline), there was no significant difference between conjugated and nonconjugated nanowires. The only significant difference is for AgNWs PVP sample and is somewhat explained by the random choice of nanowires for analysis and error in fitting function rather than the influence of surface modification.

3.4.5 Summary

This section investigates the plasmonic properties of PCP conjugates with AgNWs. Among the samples, the one with the largest diameter (AgNWs aniline) showed the lowest fluorescence enhancement. For the other samples, no significant differences in fluorescence enhancement were observed.

Unlike the layer measurements, where the highest fluorescence enhancement occurred under 480 nm excitation, the PCP–AgNW conjugates exhibited the greatest enhancement under 630 nm excitation. This shift is attributed to two factors: a significantly stronger electric field enhancement near the nanowires at 630 nm, and changes in the photophysical properties of the protein when excited at this wavelength.

Finally, the influence of conjugation on the SPP damping in AgNWs was studied. The experiments showed that even though the fluorescence for PCP conjugated with

AgNWs is weaker compared to layer of PCP, the process of conjugation doesn't affect L_{SPP} of AgNWs in a statistically significant way.

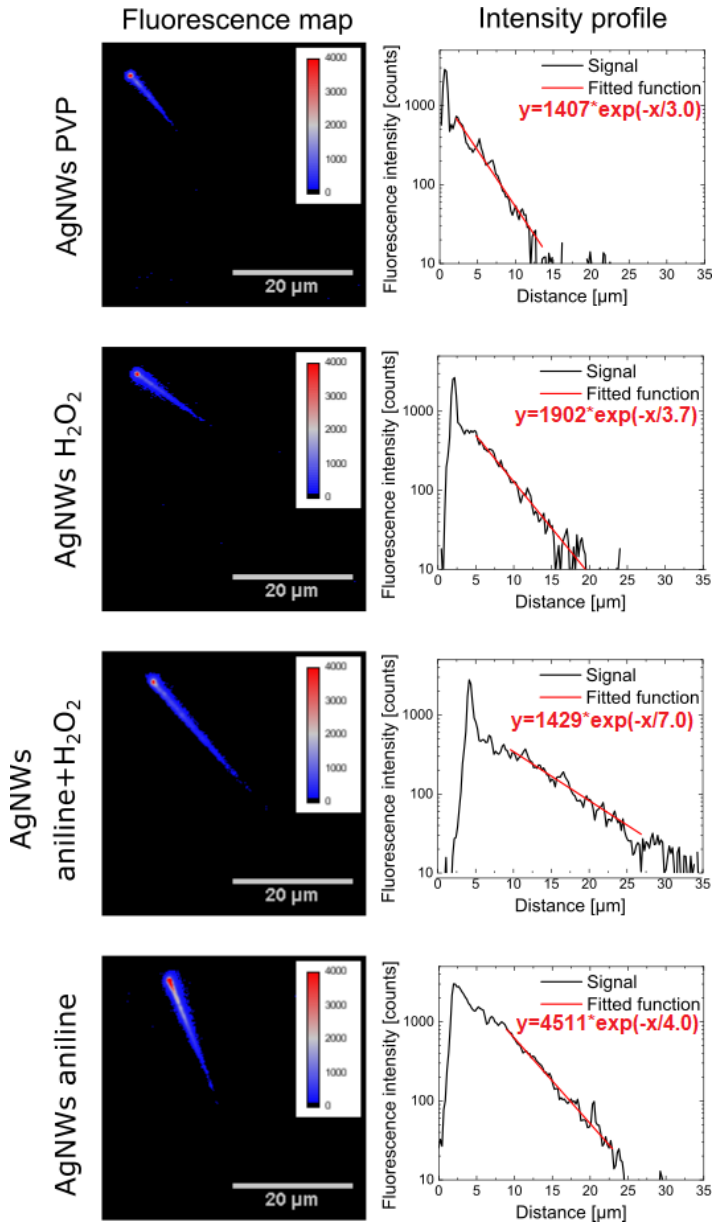

Figure 3.42: Fluorescence intensity maps acquired by two objective microscope for PCP conjugates with AgNWs, with corresponding fluorescence intensity profiles along the nanowire and fit function.

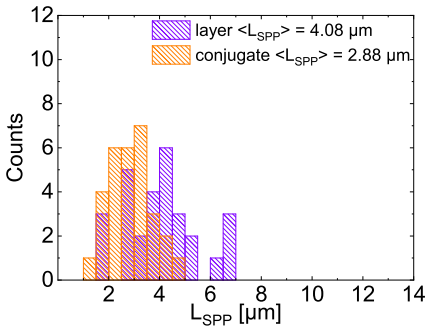

(a) L_{SPP} for AgNWs PVP before and after conjugation with PCP

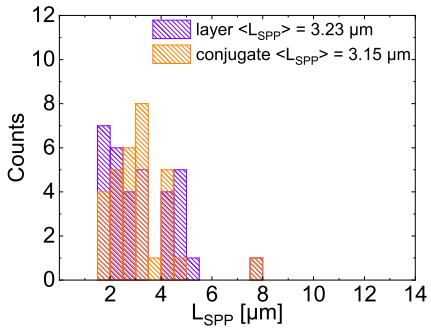

(b) L_{SPP} for AgNWs H_2O_2 before and after conjugation with PCP

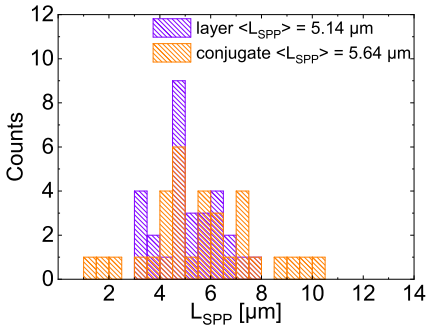

(c) L_{SPP} for AgNWs aniline+H_2O_2 before and after conjugation with PCP

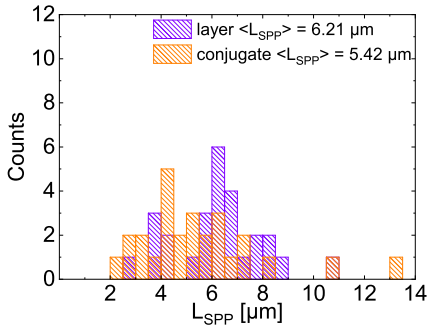

(d) L_{SPP} for AgNWs aniline before and after conjugation with PCP

Figure 3.43: Measured L_{SPP} for each sample before and after conjugation with PCP, for (a) AgNWs PVP, (b) AgNWs H_2O_2, (c) AgNWs AgNWs aniline+H_2O_2 and (d) AgNWs aniline.

3.5 Long-range remote excitation

This section describes a proof-of-concept experiment. This experiment is intended to show that SPPs propagating in a AgNW might be used to efficiently excite the fluorescence of molecules over a macroscopic distance (>100 µm) from the excitation spot. The scheme of the experiment is presented in Figure 3.44. Section **3.5.1** describes the experiment itself.

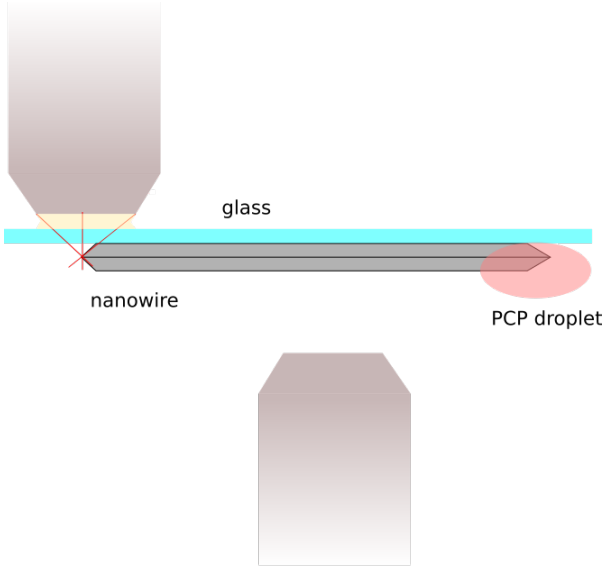

Figure 3.44: Scheme of remote excitation of PCP droplet placed at the end of nanowire.

Sample preparation

Chemicals

Toluene (99.8%, anhydrous) was purchased from Sigma-Aldrich. Acetone (99.5%), ammonium hydroxide solution ($NH_3 \cdot H_2O$, 25%), 1,2-dichloroethane (AR) were bought from Chempur. N-Octyltrimethoxysilane (OTMS, 97%) was obtained from abcr GmbH. Hydrogen peroxide (30%) was bought from Stanlab.

Hydrophobization of glass surface

The coverslips were cleaned by sonification first in acetone (10 minutes), then in 1,2-dichloroethylene (10 minutes), and finally in DI water (2 minutes, three times). Afterward, slides were placed in a vial at 70°C with 5:1:1 mixture of H_2O, H_2O_2 and $NH_3 \cdot H_2O$ for one hour. Then coverslips were washed with DI water and dried at 100 °C for 4 hours. After the drying step, the glass was placed in a vessel with 4% solution of OTMS diluted in toluene and left for 7 days in a desiccator. After the silanization

step, coverslips were cleaned by sonication first in toluene (20 minutes) and then in 1,2-dichloroethene (30 minutes). The hydrophobic glass was dried using compressed inert gas and stored in the desiccator for further use. The glass coverslip was modified with a self-assembly OTMS monolayer to prevent PCP droplets from spreading.

Manufacturing of micropipettes

Desired-sized micropipettes were obtained from borosilicate glass capillaries with filament (GB120F-10, Science product) using a laser puller (P-2000, Sutter Instruments). The inner diameter of the tip was around 10 µm. To modify micropipettes, they were put in a plugged vial with a few droplets of OTMS at the bottom and kept in the oven at 150 °C for 2 hours[138]. The glass microcapillaries were hydrophobized to prevent PCP droplet from spreading out.

Deposition of PCP at the end of a nanowire

Firstly, 2 µl droplet of AgNWs aniline suspension was deposited on a hydrophobic glass and let water to evaporate. Afterward, the sample was transferred to the inverted optical microscope for further preparation. To deposit PCP droplets, a hydrophobized micropipette was filled with 2 µl of 0.4 mg/ml PCP water solution. Then, the micropipette was connected by a silicon tube to a syringe pump. By increasing air pressure, the PCP solution was pushed to the tip of the micropipette, creating a convex meniscus at the outlet. To deposit the droplet of PCP onto the coverslip surface, the microcapillary was mounted onto a micromanipulator (MT3-Z8, Thorlabs) connected to the piezoelectric stage (E-727 Digital Piezo Controller, Physical Instruments) and gradually lowered until the meniscus touched the end of the nanowire. During the micropipette retracting from the surface, the micrometer droplet containing emitter settled onto the coverslip. It is worth to point that PCP has been deposit at only one end of nanowire. The whole microscope setup used for PCP deposition is presented in Figure 3.45.

3.5.1 Results

The sample was prepared as follows. Firstly on the glass slide water dispersion fo AgNWs was deposited onto glass coverslip and left to evaporate. Then single nanowires was localised on the sample. Then a microcapillary filled with PCP solution was connected to a silicone tube that generated pressure to push the solution toward the tip. The microcapillary was then lowered until the solution made contact with the glass coverslip at the desired location. This deposition process, from lowering the microcapillary to the point where the suspension touched the surface, was carefully monitored and controlled in real-time using an optical microscope in darkfield mode. Finally, the microcapillary was raised, leaving a microdroplet at the contact point on the glass surface. For fluorescence experiments microscope described in Section

Figure 3.45: Microscope setup with microcontrollers used to deposit PCP onto the sample.

2.1.4 was used. The only difference is the adjustment of the parameters - laser excitation power to 20 μW and camera acquisition time to 500 ms. Maps of scattered light and fluorescence intensity are presented in Figure 3.46. On the scattered light map (Figure 3.46a), on the left end of the nanowire is visible spot of PCP droplet contact with the glass surface. The droplet is not uniform with higher intensity of scattered light is visible at edges of droplet. Most likely, it is caused by the coffee ring effect[139]; thus higher amount of PCP is deposited at the edges. The circular shape at the right side of the map is a light scattered by the microscope objective hanging above the nanowire.

In fluorescence mode, when the laser is focused 1 μm away from the unmodified end of the nanowire, the signal becomes visible at two locations (Figure 3.46b). On the right side of the map, the laser appears as a circular spot, while on the left, fluorescence is detected at the site where the PCP droplet was deposited. However, the fluorescence signal is weak and is likely caused by laser light scattering on the glass surface. This scattered light excites the concentrated PCP droplet, resulting in the observed fluorescence emission.

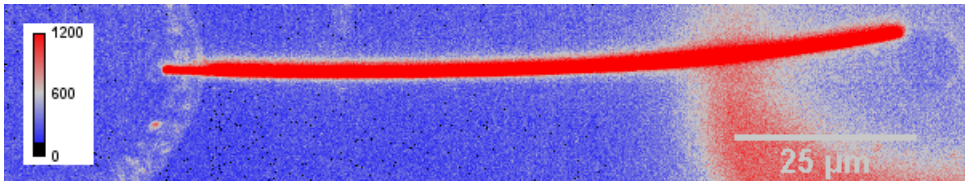

(a) scattered light image

(b) fluorescence map when the laser is focused next to nanowire

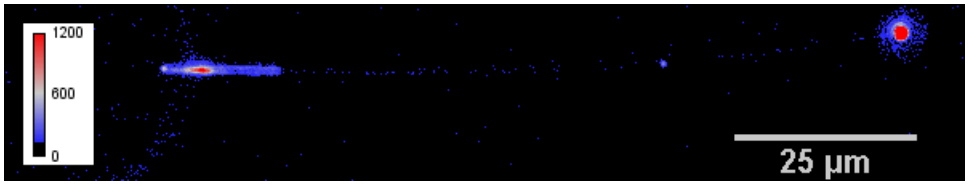

(c) fluorescence map when the laser is focused on the nanowire

Figure 3.46: Microscope images of AgNW with PCP droplet deposited at its end, (a) scattered light map, (b) fluorescence map when the laser is focused next to nanowire, (c) fluorescence map when the laser is focused on the nanowire.

When the laser is focused on the unmodified end of nanowire fluorescence map is significantly different. Signal is observed at three spots (Figure 3.46c). As these two point appear on the map only when laser is focused on the end of nanowire, they can be associated by SPPs propagation in nanowires laser excitation. These three points include laser light on the right side, a small point in the middle of the nanowire, and area on the left modified end of the nanowire. The small spot in the middle of the nanowire is most likely a small nanoparticle scattering SPPs. The bright area on the left is a strong fluorescence signal from the spot of contact between AgNW and PCP droplet. There is also fluoresce signal extending from the PCP droplet into the direction of another nanowire end. They were probably caused by capillary forces of highly hydrophilic polymer dragging water solution. This experiment proves that this optical setup and nanowires can be utilized for remote excitation over 100 µm.

3.6 Summary and conclusions

This work describes hydrothermal synthesis of silver nanowires with four sets of reactants in which polyvinylpyrrolidone, hydrogen peroxide, and aniline, were used. Depending on the reducing agent, each sample possesses distinct diameter and length distribution.

Metal enhanced fluorescence enhancement of model protein - Peridinin-Chlorophyll-Protein Complex was studied in two configurations. In the first configuration, nanowires were embedded in a thin polymer matrix (dozens of nanometers, appendix Figure 3.48) containing fluorophores. The highest fluorescence enhancement was observed for samples with thin nanowires (AgNWs PVP and AgNWs aniline samples, mean diameter 76-78 nm) and excitation frequency close to the frequency of localized plasmon resonance of silver nanowires. In the second configuration, fluorophore was conjugated with AgNWs at a close distance from nanowires' surface. Once again, fluorescence enhancement values followed the spectrum of AgNWs scattering, except for excitation at 630 nm, for which the highest enhancement was observed. This phenomenon was attributed to the excitation of different chemical moieties present in protein and thus the change of photo-physics of this hybrid structure. Finite element method simulations unveiled that mean electric field enhancement does not depend on the nanowire diameter; thus, radiative and non-radiative processes between fluorophore and silver nanowire have a crucial impact on fluorescence enhancement.

Home built double objective microscope was used for silver nanowires' waveguiding properties. Longer surface plasmon polaritons propagation lengths were observed for samples with bigger nanowires' diameters (mean diameter 153 nm). Experiments proved that chemical modification of the surface of silver nanowires does not influence their waveguiding properties. Finite elements method simulations showed that the length of propagation of surface plasmon polaritons in silver nanowires highly depends on their diameter. Comparison of theoretical and experimental lengths of surface plasmon propagation proved that only the first guiding mode is excited in an experimental configuration.

Finally, a proof-of-concept experiment demonstrated that the nanowires synthesized using the previously described method were capable of exciting molecules located over 100 μm away from the excitation point.

I anticipate that the AgNW synthesis method presented in this work could serve as a viable alternative to the commonly used polyol method. This approach offers better control over the dimensions of nanowires and relies on a more environmentally friendly hydrothermal process. In addition, longer AgNWs, which are easily obtained through this method, are beneficial for various applications such as the fabrication of transparent conductive layers. Exploring the plasmonic properties of AgNWs may also contribute to the development of advanced photonic devices, including optical logic gates and biosensors.

Bibliography

[1] Richard P. Feynman. “There’s Plenty of Room at the Bottom”. In: 1959.

[2] Michel Vert et al. “Terminology for biorelated polymers and applications (IUPAC Recommendations 2012):” in: *Pure and Applied Chemistry* 84.2 (2012), pp. 377–410. DOI: doi:10.1351/PAC-REC-10-12-04.

[3] Erik C. Dreaden et al. “The golden age: gold nanoparticles for biomedicine”. In: *Chem. Soc. Rev.* 41 (7 2012), pp. 2740–2779. DOI: 10.1039/C1CS15237H.

[4] Ibrahim Khan, Khalid Saeed, and Idrees Khan. “Nanoparticles: Properties, applications and toxicities”. In: *Arabian Journal of Chemistry* 12.7 (Nov. 2019), pp. 908–931. DOI: 10.1016/j.arabjc.2017.05.011.

[5] Gayan Priyadarshana et al. “Synthesis of Magnetite Nanoparticles by Top-Down Approach from a High Purity Ore”. In: *Journal of Nanomaterials* 2015 (Sept. 2015), pp. 312–317. ISSN: 1687-4110. DOI: 10.1155/2015/317312.

[6] Xiao Zhang et al. “A Facile and Universal Top-Down Method for Preparation of Monodisperse Transition-Metal Dichalcogenide Nanodots”. In: *Angewandte Chemie International Edition* 54.18 (2015), pp. 5425–5428. DOI: https://doi.org/10.1002/anie.201501071.

[7] A. K. Geim and K. S. Novoselov. “The rise of graphene”. In: *Nature Materials* 6.3 (Mar. 2007), pp. 183–191. DOI: 10.1038/nmat1849.

[8] Younan Xia et al. “Shape-Controlled Synthesis of Metal Nanocrystals: Simple Chemistry Meets Complex Physics?” In: *Angewandte Chemie International Edition* 48.1 (2009), pp. 60–103. DOI: https://doi.org/10.1002/anie.200802248.

[9] Victor K. LaMer and Robert H. Dinegar. “Theory, Production and Mechanism of Formation of Monodispersed Hydrosols”. In: *Journal of the American Chemical Society* 72.11 (Nov. 1950), pp. 4847–4854. ISSN: 0002-7863. DOI: 10.1021/ja01167a001.

[10] Benjamin Wiley et al. “Shape-Controlled Synthesis of Metal Nanostructures: The Case of Silver”. In: *Chemistry – A European Journal* 11.2 (2005), pp. 454–463. DOI: https://doi.org/10.1002/chem.200400927.

[11] Catherine J. Murphy et al. “Anisotropic Metal Nanoparticles: Synthesis, Assembly, and Optical Applications”. In: *The Journal of Physical Chemistry B* 109.29 (July 2005), pp. 13857–13870. ISSN: 1520-6106. DOI: 10.1021/jp0516846.

[12] Y. Xiong and Y. Xia. “Shape-Controlled Synthesis of Metal Nanostructures: The Case of Palladium”. In: *Advanced Materials* 19.20 (2007), pp. 3385–3391. DOI: https://doi.org/10.1002/adma.200701301.

[13] P. W. (Peter William) Atkins and Julio. De Paula. *Atkins' Physical chemistry*. eng. 10th ed. Oxford: Oxford University Press, 2014. ISBN: 9780199697403.

[14] Wikipedia. *Truncated octahedron — Wikipedia, The Free Encyclopedia*. http://en.wikipedia.org/w/index.php?title=Truncated\%20octahedron&oldid=1084420221. [Online; accessed 11-July-2022]. 2022.

[15] Sumio Iijima and Toshinari Ichihashi. “Structural instability of ultrafine particles of metals”. In: *Phys. Rev. Lett.* 56 (6 Feb. 1986), pp. 616–619. DOI: 10.1103/PhysRevLett.56.616.

[16] F. Baletto et al. “Crossover among structural motifs in transition and noble-metal clusters”. In: *The Journal of Chemical Physics* 116.9 (2002), pp. 3856–3863. DOI: 10.1063/1.1448484.

[17] Charles L. Cleveland and Uzi Landman. “The energetics and structure of nickel clusters: Size dependence”. In: *The Journal of Chemical Physics* 94.11 (1991), pp. 7376–7396. DOI: 10.1063/1.460169.

[18] V. Germain et al. “Stacking Faults in Formation of Silver Nanodisks”. In: *The Journal of Physical Chemistry B* 107.34 (Aug. 2003), pp. 8717–8720. ISSN: 1520-6106. DOI: 10.1021/jp0303826.

[19] Pei-Feng Ho and Kai-Ming Chi. “Size-controlled synthesis of Pd nanoparticles from -diketonato complexes of palladium”. In: *Nanotechnology* 15.8 (June 2004), pp. 1059–1064. DOI: 10.1088/0957-4484/15/8/035.

[20] I. Washio et al. “Reduction by the End Groups of Poly(vinyl pyrrolidone): A New and Versatile Route to the Kinetically Controlled Synthesis of Ag Triangular Nanoplates”. In: *Advanced Materials* 18.13 (2006), pp. 1745–1749. DOI: https://doi.org/10.1002/adma.200600675.

[21] Yujie Xiong et al. “Kinetically Controlled Synthesis of Triangular and Hexagonal Nanoplates of Palladium and Their SPR/SERS Properties”. In: *Journal of the American Chemical Society* 127.48 (Dec. 2005), pp. 17118–17127. ISSN: 0002-7863. DOI: 10.1021/ja056498s.

[22] Y. Sun and Y. Xia. “Triangular Nanoplates of Silver: Synthesis, Characterization, and Use as Sacrificial Templates For Generating Triangular Nanorings of Gold”. In: *Advanced Materials* 15.9 (2003), pp. 695–699. DOI: https://doi.org/10.1002/adma.200304652.

[23] Jinhwan Lee et al. “Very long Ag nanowire synthesis and its application in a highly transparent, conductive and flexible metal electrode touch panel”. In: *Nanoscale* 4.20 (2012), p. 6408. DOI: 10.1039/c2nr31254a.

[24] Pei Zhang et al. “Silver nanowires: Synthesis technologies, growth mechanism and multifunctional applications”. In: *Materials Science and Engineering: B* 223 (2017), pp. 1–23. ISSN: 0921-5107. DOI: https://doi.org/10.1016/j.mseb.2017.05.002.

[25] Heebo Ha et al. “Mini review of synthesis strategies of silver nanowires and their applications”. In: *Colloid and Interface Science Communications* 50 (2022), p. 100663. ISSN: 2215-0382. DOI: https://doi.org/10.1016/j.colcom.2022.100663.

[26] S.V. Kalinin et al. “Ferroelectric Lithography of Multicomponent Nanostructures”. In: *Advanced Materials* 16.9-10 (2004), pp. 795–799. DOI: https://doi.org/10.1002/adma.200305702.

[27] Rui-Long Zong et al. “Synthesis and Optical Properties of Silver Nanowire Arrays Embedded in Anodic Alumina Membrane”. In: *The Journal of Physical Chemistry B* 108.43 (Oct. 2004), pp. 16713–16716. ISSN: 1520-6106. DOI: 10.1021/jp0474172.

[28] D. Ugarte, A. Châtelain, and W. A. de Heer. “Nanocapillarity and Chemistry in Carbon Nanotubes”. In: *Science* 274.5294 (1996), pp. 1897–1899. DOI: 10.1126/science.274.5294.1897.

[29] Nikhil R. Jana, Latha Gearheart, and Catherine J. Murphy. “Wet chemical synthesis of silver nanorods and nanowires of controllable aspect ratio”. In: *Chem. Commun.* (7 2001), pp. 617–618. DOI: 10.1039/B100521I.

[30] Linfeng Gou, Mircea Chipara, and Jeffrey M. Zaleski. “Convenient, Rapid Synthesis of Ag Nanowires”. In: *Chemistry of Materials* 19.7 (Apr. 2007), pp. 1755–1760. ISSN: 0897-4756. DOI: 10.1021/cm070160a.

[31] Zhifeng Chen et al. “Anisotropic Growth of Silver Nanoparticles Is Kinetically Controlled by Polyvinylpyrrolidone Binding”. In: *Journal of the American Chemical Society* 141.10 (Mar. 2019), pp. 4328–4337. ISSN: 0002-7863. DOI: 10.1021/jacs.8b11295.

[32] Bushra Bari et al. “Simple hydrothermal synthesis of very-long and thin silver nanowires and their application in high quality transparent electrodes”. In: *J. Mater. Chem. A* 4 (29 2016), pp. 11365–11371. DOI: 10.1039/C6TA03308C.

[33] Sang Hyuk Im et al. “Large-Scale Synthesis of Silver Nanocubes: The Role of HCl in Promoting Cube Perfection and Monodispersity”. In: *Angewandte Chemie International Edition* 44.14 (Mar. 2005), pp. 2154–2157. DOI: 10.1002/anie.200462208.

[34] Yugang Sun et al. “Uniform Silver Nanowires Synthesis by Reducing AgNO3 with Ethylene Glycol in the Presence of Seeds and Poly(Vinyl Pyrrolidone)”. In: *Chemistry of Materials* 14.11 (Oct. 2002), pp. 4736–4745. DOI: 10.1021/cm020587b.

[35] Yugang Sun et al. “Crystalline Silver Nanowires by Soft Solution Processing”. In: *Nano Letters* 2.2 (Jan. 2002), pp. 165–168. DOI: 10.1021/nl010093y.

[36] Kylee E. Korte, Sara E. Skrabalak, and Younan Xia. “Rapid synthesis of silver nanowires through a CuCl- or CuCl2-mediated polyol process”. In: *Journal of Materials Chemistry* 18.4 (2008), pp. 437–441. DOI: 10.1039/b714072j.

[37] Stephen M. Bergin et al. “The effect of nanowire length and diameter on the properties of transparent, conducting nanowire films”. In: *Nanoscale* 4.6 (2012), p. 1996. DOI: 10.1039/c2nr30126a.

[38] Sahin Coskun, Burcu Aksoy, and Husnu Emrah Unalan. “Polyol Synthesis of Silver Nanowires: An Extensive Parametric Study”. In: *Crystal Growth and Design* 11.11 (Sept. 2011), pp. 4963–4969. DOI: 10.1021/cg200874g.

[39] Yunxia Ran et al. “A one-step route to Ag nanowires with a diameter below 40 nm and an aspect ratio above 1000”. In: *Chem. Commun.* 50 (94 2014), pp. 14877–14880. DOI: 10.1039/C4CC04698F.

[40] Jingjing Ma and Maosheng Zhan. “Rapid production of silver nanowires based on high concentration of AgNO3 precursor and use of FeCl3 as reaction promoter”. In: *RSC Adv.* 4 (40 2014), pp. 21060–21071. DOI: 10.1039/C4RA00711E.

[41] Benjamin Wiley et al. “Polyol Synthesis of Silver Nanoparticles: Use of Chloride and Oxygen to Promote the Formation of Single-Crystal, Truncated Cubes and Tetrahedrons”. In: *Nano Letters* 4.9 (Aug. 2004), pp. 1733–1739. DOI: 10.1021/nl048912c.

[42] Benjamin Wiley, Yugang Sun, and Younan Xia. “Polyol Synthesis of Silver Nanostructures: Control of Product Morphology with Fe(II) or Fe(III) Species”. In: *Langmuir* 21.18 (Aug. 2005), pp. 8077–8080. DOI: 10.1021/la050887i.

[43] Dirk L. Van Hyning and Charles F. Zukoski. “Formation Mechanisms and Aggregation Behavior of Borohydride Reduced Silver Particles”. In: *Langmuir* 14.24 (Oct. 1998), pp. 7034–7046. DOI: 10.1021/la980325h.

[44] Waynie M. Schuette and William E. Buhro. “Silver Chloride as a Heterogeneous Nucleant for the Growth of Silver Nanowires”. In: *ACS Nano* 7.5 (Apr. 2013), pp. 3844–3853. DOI: 10.1021/nn400414h.

[45] Waynie M. Schuette and William E. Buhro. “Polyol Synthesis of Silver Nanowires by Heterogeneous Nucleation Mechanistic Aspects Influencing Nanowire Diameter and Length”. In: *Chemistry of Materials* 26.22 (Nov. 2014), pp. 6410–6417. DOI: 10.1021/cm502827b.

[46] Yurui Fang et al. “Branched Silver Nanowires as Controllable Plasmon Routers”. In: *Nano Letters* 10.5 (Apr. 2010), pp. 1950–1954. DOI: 10.1021/nl101168u.

[47] Liangbing Hu et al. “Scalable Coating and Properties of Transparent, Flexible, Silver Nanowire Electrodes”. In: *ACS Nano* 4.5 (Apr. 2010), pp. 2955–2963. DOI: 10.1021/nn1005232.

[48] C. V. Mary Vijila et al. “Synthesis of silver nanowires using hydrothermal technique for flexible transparent electrode application”. In: *AIP Conference Proceedings* 1731.1 (May 2016), p. 080073. ISSN: 0094-243X. DOI: 10.1063/1.4947951. eprint: https://pubs.aip.org/aip/acp/article-pdf/doi/10.1063/1.4947951/13092594/080073_1_online.pdf.

[49] Zhiqiang Yang et al. “One-pot hydrothermal synthesis of silver nanowires via citrate reduction”. en. In: *J. Colloid Interface Sci.* 352.2 (Dec. 2010), pp. 285–291.

[50] Wlad Kusnezow and Jorg D. Hoheisel. “Solid supports for microarray immunoassays”. In: *Journal of Molecular Recognition* 16.4 (2003), pp. 165–176. DOI: 10.1002/jmr.625.

[51] Neus G. Bastús et al. “Synthesis of Highly Monodisperse Citrate-Stabilized Silver Nanoparticles of up to 200 nm: Kinetic Control and Catalytic Properties”. In: *Chemistry of Materials* 26.9 (Apr. 2014), pp. 2836–2846. DOI: 10.1021/cm500316k.

[52] Iulia Pinzaru et al. “Stable PEG-coated silver nanoparticles – A comprehensive toxicological profile”. In: *Food and Chemical Toxicology* 111 (Jan. 2018), pp. 546–556. DOI: 10.1016/j.fct.2017.11.051.

[53] Kazuhiro Nakanishi et al. “Recent advances in controlled immobilization of proteins onto the surface of the solid substrate and its possible application to proteomics”. English. In: *Current Proteomics* 5.3 (Oct. 2008), pp. 161–175. ISSN: 1570-1646. DOI: 10.2174/157016408785909622.

[54] Federica Rusmini, Zhiyuan Zhong, and Jan Feijen. “Protein Immobilization Strategies for Protein Biochips”. In: *Biomacromolecules* 8.6 (Apr. 2007), pp. 1775–1789. DOI: 10.1021/bm061197b.

[55] Alexandra Golikova et al. “Excess enthalpies and heat of esterification reaction in ethanolacetic acid ethyl acetate water system at 313.15 K”. In: *Journal of Thermal Analysis and Calorimetry* 139.2 (June 2019), pp. 1301–1307. DOI: 10.1007/s10973-019-08488-y.

[56] Jeremy M. Fowler, Margaret C. Stuart, and Danny K. Y. Wong. “Self-Assembled Layer of Thiolated Protein G as an Immunosensor Scaffold”. In: *Analytical Chemistry* 79.1 (Nov. 2006), pp. 350–354. DOI: 10.1021/ac061175f.

[57] E. Mauriz, M.C. García-Fernández, and L.M. Lechuga. “Towards the design of universal immunosurfaces for SPR-based assays: A review”. In: *TrAC Trends in Analytical Chemistry* 79 (May 2016), pp. 191–198. DOI: 10.1016/j.trac.2016.02.006.

[58] Harsh Sharma and Raj Mutharasan. “Half Antibody Fragments Improve Biosensor Sensitivity without Loss of Selectivity”. In: *Analytical Chemistry* 85.4 (Feb. 2013), pp. 2472–2477. DOI: 10.1021/ac3035426.

[59] Jaroslava Turková. “Oriented immobilization of biologically active proteins as a tool for revealing protein interactions and function”. In: *Journal of Chromatography B: Biomedical Sciences and Applications* 722.1-2 (Feb. 1999), pp. 11–31. DOI: 10.1016/s0378-4347(98)00434-4.

[60] Rosaria P. Haugland and Wendy W. You. “Coupling of Antibodies With Biotin”. In: *Methods in molecular biology*. Humana Press, 2008, pp. 13–23. DOI: 10.1007/978-1-59745-579-4_2.

[61] Claire E. Chivers et al. “How the biotin–streptavidin interaction was made even stronger: investigation via crystallography and a chimaeric tetramer”. In: *The Biochemical journal* 435.1 (Mar. 2011), pp. 55–63. DOI: 10.1042/bj20101593.

[62] Hadi Shafiee et al. “Nanostructured Optical Photonic Crystal Biosensor for HIV Viral Load Measurement”. In: *Scientific Reports* 4.1 (Feb. 2014). DOI: 10.1038/srep04116.

[63] Greta J. Wegner et al. “Fabrication of Histidine-Tagged Fusion Protein Arrays for Surface Plasmon Resonance Imaging Studies of Protein-Protein and Protein-DNA Interactions”. In: *Analytical Chemistry* 75.18 (Aug. 2003), pp. 4740–4746. DOI: 10.1021/ac0344438.

[64] R.M. Mayall et al. “An electrochemical lipopolysaccharide sensor based on an immobilized Toll-Like Receptor-4”. In: *Biosensors and Bioelectronics* 87 (Jan. 2017), pp. 794–801. DOI: 10.1016/j.bios.2016.09.009.

[65] Ewa Brzozowska et al. “Recognition of bacterial lipopolysaccharide using bacteriophage-adhesin-coated long-period gratings”. In: *Biosensors and Bioelectronics* 67 (May 2015), pp. 93–99. DOI: 10.1016/j.bios.2014.07.027.

[66] K. Lance Kelly et al. “The Optical Properties of Metal Nanoparticles: The Influence of Size, Shape, and Dielectric Environment”. In: *The Journal of Physical Chemistry B* 107.3 (Dec. 2002), pp. 668–677. DOI: 10.1021/jp026731y.

[67] Gustav Mie. “Beitrage zur Optik truber Medien, speziell kolloidaler Metallosungen”. In: *Annalen der Physik* 330.3 (1908), pp. 377–445. DOI: 10.1002/andp.19083300302.

[68] Stephan Link and Mostafa A. El-Sayed. “Spectral Properties and Relaxation Dynamics of Surface Plasmon Electronic Oscillations in Gold and Silver Nanodots and Nanorods”. In: *The Journal of Physical Chemistry B* 103.40 (Sept. 1999), pp. 8410–8426. DOI: 10.1021/jp9917648.

[69] Lukas Novotny and Niek van Hulst. “Antennas for light”. In: *Nature Photonics* 5.2 (Feb. 2011), pp. 83–90. DOI: 10.1038/nphoton.2010.237.

[70] Lukas Novotny and Bert Hecht. *Principles of Nano-Optics*. Cambridge University Press, 2006. DOI: 10.1017/cbo9780511813535.

[71] Alberto Sinibaldi et al. “Direct comparison of the performance of Bloch surface wave and surface plasmon polariton sensors”. In: *Sensors and Actuators B: Chemical* 174 (2012), pp. 292–298. ISSN: 0925-4005. DOI: https://doi.org/10.1016/j.snb.2012.07.015.

[72] Ha Minh Hiep et al. “A localized surface plasmon resonance based immunosensor for the detection of casein in milk”. In: *Science and Technology of Advanced Materials* 8.4 (2007), pp. 331–338. DOI: 10.1016/j.stam.2006.12.010. eprint: https://doi.org/10.1016/j.stam.2006.12.010.

[73] William L. Barnes, Alain Dereux, and Thomas W. Ebbesen. “Surface plasmon subwavelength optics”. In: *Nature* 424.6950 (Aug. 2003), pp. 824–830. DOI: 10.1038/nature01937.

[74] Barbara Wild et al. “Propagation Lengths and Group Velocities of Plasmons in Chemically Synthesized Gold and Silver Nanowires”. In: *ACS Nano* 6.1 (Jan. 2012), pp. 472–482. DOI: 10.1021/nn203802e.

[75] Wei Deng et al. “Metal-enhanced fluorescence in the life sciences: here, now and beyond”. In: *Phys. Chem. Chem. Phys.* 15 (38 2013), pp. 15695–15708. DOI: 10.1039/C3CP50206F.

[76] Sebastian Mackowski. “Hybrid nanostructures for efficient light harvesting”. In: *Journal of Physics: Condensed Matter* 22.19 (Apr. 2010), p. 193102. DOI: 10.1088/0953-8984/22/19/193102.

[77] Joseph Lakowicz. *Principles of fluorescence spectroscopy*. New York: Springer, 2006. ISBN: 978-0-387-31278-1.

[78] Chris D. Geddes and Joseph R. Lakowicz. “Metal-Enhanced Fluorescence”. In: *Journal of Fluorescence* 12.2 (2002), pp. 121–129. DOI: 10.1023/a:1016875709579.

[79] Joseph R. Lakowicz. “Radiative Decay Engineering: Biophysical and Biomedical Applications”. In: *Analytical Biochemistry* 298.1 (Nov. 2001), pp. 1–24. DOI: 10.1006/abio.2001.5377.

[80] Pascal Anger, Palash Bharadwaj, and Lukas Novotny. “Enhancement and Quenching of Single-Molecule Fluorescence”. In: *Physical Review Letters* 96.11 (Mar. 2006). DOI: 10.1103/physrevlett.96.113002.

[81] Joanna Niedziółka-Jönsson and Sebastian Mackowski. “Plasmonics with Metallic Nanowires”. In: *Materials* 12.9 (May 2019), p. 1418. DOI: 10.3390/ma12091418.

[82] Marcin Szalkowski et al. “Plasmon-induced absorption of blind chlorophylls in photosynthetic proteins assembled on silver nanowires”. In: *Nanoscale* 9.29 (2017), pp. 10475–10486. DOI: 10.1039/c7nr03866f.

[83] Dorota Kowalska et al. “Spectrally selective fluorescence imaging of Chlorobaculum tepidum reaction centers conjugated to chelator-modified silver nanowires”. In: *Photosynthesis Research* 135.1-3 (Oct. 2017), pp. 329–336. DOI: 10.1007/s11120-017-0455-y.

[84] Wenkai Zhang et al. “Effective excitation and control of guided surface plasmon polaritons in a conjugated polymer–silver nanowire composite system”. In: *J. Mater. Chem. C* 1.6 (2013), pp. 1265–1271. DOI: 10.1039/c2tc00568a.

[85] Dorota Kowalska et al. “Metal-Enhanced Fluorescence of Chlorophylls in Light-Harvesting Complexes Coupled to Silver Nanowires”. In: *The Scientific World Journal* 2013 (2013), pp. 1–12. DOI: 10.1155/2013/670412.

[86] Timur Shegai et al. “Coloring fluorescence emission with silver nanowires”. In: *Applied Physics Letters* 96.10 (Mar. 2010), p. 103114. DOI: 10.1063/1.3355545.

[87] Shy-Hauh Guo et al. “Spacer Layer Effect in Fluorescence Enhancement from Silver Nanowires over a Silver Film Switching of Optimum Polarization”. In: *Nano Letters* 9.7 (June 2009), pp. 2666–2670. DOI: 10.1021/nl901112h.

[88] Ekmel Ozbay. “Plasmonics: Merging Photonics and Electronics at Nanoscale Dimensions”. In: *Science* 311.5758 (Jan. 2006), pp. 189–193. DOI: 10.1126/science.1114849.

[89] Piotr Bujak et al. “Polymers for electronics and spintronics”. In: *Chemical Society Reviews* 42.23 (2013), p. 8895. DOI: 10.1039/c3cs60257e.

[90] Chul-Hyun Kim et al. “Silver Nanowire Embedded in P3HT:PCB for High-Efficiency Hybrid Photovoltaic Device Applications”. In: *ACS Nano* 5.4 (Mar. 2011), pp. 3319–3325. DOI: 10.1021/nn200469d.

[91] Chun-Chao Chen et al. “Visibly Transparent Polymer Solar Cells Produced by Solution Processing”. In: *ACS Nano* 6.8 (July 2012), pp. 7185–7190. DOI: 10.1021/nn3029327.

[92] Karolina Smolarek et al. “Silver nanowires enhance absorption of poly(3-hexylthiophene)”. In: *Applied Physics Letters* 103.20 (Nov. 2013), p. 203302. DOI: 10.1063/1.4829623.

[93] Jaebeom Lee et al. “Bioconjugated Ag Nanoparticles and CdTe Nanowires: Metamaterials with Field-Enhanced Light Absorption”. In: *Angewandte Chemie* 118.29 (July 2006), pp. 4937–4941. DOI: 10.1002/ange.200600356.

[94] Karolina Sulowska et al. “Real-time fluorescence sensing of single photoactive proteins using silver nanowires”. In: *Methods and Applications in Fluorescence* 8.4 (July 2020), p. 045004. DOI: 10.1088/2050-6120/aba7cb.

[95] Jaebeom Lee et al. “Bioconjugates of CdTe Nanowires and Au Nanoparticles: Plasmon-Exciton Interactions, Luminescence Enhancement, and Collective Effects”. In: *Nano Letters* 4.12 (Nov. 2004), pp. 2323–2330. DOI: 10.1021/nl048669h.

[96] Hong Wei and Hongxing Xu. “Nanowire-based plasmonic waveguides and devices for integrated nanophotonic circuits”. In: *Nanophotonics* 1.2 (Nov. 2012), pp. 155–169. DOI: 10.1515/nanoph-2012-0012.

[97] Xin Guo et al. “Nanowire plasmonic waveguides, circuits and devices”. In: *Laser & Photonics Reviews* 7.6 (Jan. 2013), pp. 855–881. DOI: 10.1002/lpor.201200067.

[98] J.-C. Weeber et al. “Near-field observation of surface plasmon polariton propagation on thin metal stripes”. In: *Phys. Rev. B* 64 (4 July 2001), p. 045411. DOI: 10.1103/PhysRevB.64.045411.

[99] Rashid Zia, Jon A. Schuller, and Mark L. Brongersma. “Near-field characterization of guided polariton propagation and cutoff in surface plasmon waveguides”. In: *Phys. Rev. B* 74 (16 Oct. 2006), p. 165415. DOI: 10.1103/PhysRevB.74.165415.

[100] D. F. P. Pile and D. K. Gramotnev. “Channel plasmon–polariton in a triangular groove on a metal surface”. In: *Opt. Lett.* 29.10 (May 2004), pp. 1069–1071. DOI: 10.1364/OL.29.001069.

[101] Sergey I. Bozhevolnyi et al. “Channel plasmon subwavelength waveguide components including interferometers and ring resonators”. In: *Nature* 440.7083 (Mar. 2006), pp. 508–511. DOI: 10.1038/nature04594.

[102] B. Steinberger et al. “Dielectric stripes on gold as surface plasmon waveguides”. In: *Applied Physics Letters* 88.9 (Feb. 2006), p. 094104. DOI: 10.1063/1.2180448.

[103] R. F. Oulton et al. “A hybrid plasmonic waveguide for subwavelength confinement and long-range propagation”. In: *Nature Photonics* 2.8 (July 2008), pp. 496–500. DOI: 10.1038/nphoton.2008.131.

[104] Primoz Kusar et al. “Measurement and Reduction of Damping in Plasmonic Nanowires”. In: *Nano Letters* 12.2 (Jan. 2012), pp. 661–665. DOI: 10.1021/nl203452d.

[105] P. B. Johnson and R. W. Christy. “Optical Constants of the Noble Metals”. In: *Physical Review B* 6.12 (Dec. 1972), pp. 4370–4379. DOI: 10.1103/physrevb.6.4370.

[106] Monisha Kumar and K. Porsezian. “A comparative study of surface plasmon polariton propagation characteristics of various metals”. In: *AIP Conference Proceedings*. Author(s), 2016. DOI: 10.1063/1.4947958.

[107] Hong Wei et al. “Plasmon Waveguiding in Nanowires”. In: *Chemical Reviews* 118.6 (Feb. 2018), pp. 2882–2926. DOI: 10.1021/acs.chemrev.7b00441.

[108] Shunping Zhang and Hongxing Xu. “Optimizing Substrate-Mediated Plasmon Coupling toward High-Performance Plasmonic Nanowire Waveguides”. In: *ACS Nano* 6.9 (Aug. 2012), pp. 8128–8135. DOI: 10.1021/nn302755a.

[109] Paul Johns et al. “Dynamics of Surface Plasmon Polaritons in Metal Nanowires”. In: *The Journal of Physical Chemistry C* 121.10 (Feb. 2017), pp. 5445–5459. DOI: 10.1021/acs.jpcc.6b12748.

[110] Qiang Li and Min Qiu. “Plasmonic wave propagation in silver nanowires: guiding modes or not?” In: *Optics Express* 21.7 (Apr. 2013), p. 8587. DOI: 10.1364/oe.21.008587.

[111] R F Oulton et al. “Confinement and propagation characteristics of subwavelength plasmonic modes”. In: *New Journal of Physics* 10.10 (Oct. 2008), p. 105018. DOI: 10.1088/1367-2630/10/10/105018.

[112] Yurui Fang et al. “Remote-Excitation Surface-Enhanced Raman Scattering Using Propagating Ag Nanowire Plasmons”. In: *Nano Letters* 9.5 (2009). PMID: 19391601, pp. 2049–2053. DOI: 10.1021/nl900321e. eprint: https://doi.org/10.1021/nl900321e.

[113] Liang Su et al. “Visualization of molecular fluorescence point spread functions via remote excitation switching fluorescence microscopy”. In: *Nature Communications* 6.1 (Feb. 2015). DOI: 10.1038/ncomms7287.

[114] A. Prymaczek et al. “Remote activation and detection of up-converted luminescence via surface plasmon polaritons propagating in a silver nanowire”. In: *Nanoscale* 10.26 (2018), pp. 12841–12847. DOI: 10.1039/c8nr04517h.

[115] Robert Blankenship. *Molecular mechanisms of photosynthesis*. Oxford Malden, MA: Blackwell Science, 2002. ISBN: 978-0-470-75847-2.

[116] E. Hofmann, W. Welte, and K. Diederichs. *PERIDININ-CHLOROPHYLL-PROTEIN OF AMPHIDINIUM CARTERAE*. Aug. 1997. DOI: 10.2210/pdb1ppr/pdb.

[117] James A. Bautista et al. “Singlet and Triplet Energy Transfer in the Peridinin-Chlorophyll a-Protein from Amphidinium carterae”. In: *The Journal of Physical Chemistry A* 103.14 (Jan. 1999), pp. 2267–2273. DOI: 10.1021/jp983943f.

[118] Tomáš Polívka, Roger G. Hiller, and Harry A. Frank. “Spectroscopy of the peridinin–chlorophyll-a protein: Insight into light-harvesting strategy of marine algae”. In: *Archives of Biochemistry and Biophysics* 458.2 (Feb. 2007), pp. 111–120. DOI: 10.1016/j.abb.2006.10.006.

[119] COMSOL Multiphysics. “Introduction to COMSOL multiphysics®”. In: *COMSOL Multiphysics, Burlington, MA, accessed Feb* 9 (1998), p. 2018.

[120] Kevin M. McPeak et al. “Plasmonic Films Can Easily Be Better: Rules and Recipes”. In: *ACS Photonics* 2.3 (Feb. 2015), pp. 326–333. DOI: 10.1021/ph5004237.

[121] Tobias A. F. König et al. “Electrically Tunable Plasmonic Behavior of Nanocube–Polymer Nanomaterials Induced by a Redox-Active Electrochromic Polymer”. In: *ACS Nano* 8.6 (June 2014), pp. 6182–6192. DOI: 10.1021/nn501601e.

[122] Max J. Schnepf et al. “Nanorattles with tailored electric field enhancement”. In: *Nanoscale* 9 (27 2017), pp. 9376–9385. DOI: 10.1039/C7NR02952G.

[123] Michał Ćwik et al. “Optical Properties of Submillimeter Silver Nanowires Synthesized Using the Hydrothermal Method”. In: *Materials* 12.5 (Mar. 2019), p. 721. DOI: 10.3390/ma12050721.

[124] Yujie Xiong et al. “Poly(vinyl pyrrolidone): A Dual Functional Reductant and Stabilizer for the Facile Synthesis of Noble Metal Nanoplates in Aqueous Solutions”. In: *Langmuir* 22.20 (Aug. 2006), pp. 8563–8570. DOI: 10.1021/la061323x.

[125] I. Washio et al. “Reduction by the End Groups of Poly(vinyl pyrrolidone): A New and Versatile Route to the Kinetically Controlled Synthesis of Ag Triangular Nanoplates”. In: *Advanced Materials* 18.13 (July 2006), pp. 1745–1749. DOI: 10.1002/adma.200600675.

[126] Qiao Zhang et al. “A Systematic Study of the Synthesis of Silver Nanoplates: Is Citrate a “Magic” Reagent?” In: *Journal of the American Chemical Society* 133.46 (Nov. 2011), pp. 18931–18939. ISSN: 0002-7863. DOI: 10.1021/ja2080345.

[127] Zaheer Khan et al. “Preparation and characterization of silver nanoparticles using aniline”. In: *Arabian Journal of Chemistry* 10 (May 2017), S1506–S1511. DOI: 10.1016/j.arabjc.2013.05.001.

[128] Patrycja Bober et al. “Oxidation of Aniline with Silver Nitrate Accelerated by p-Phenylenediamine: A New Route to Conducting Composites”. In: *Macromolecules* 43.24 (Nov. 2010), pp. 10406–10413. DOI: 10.1021/ma101474j.

[129] I. Yu. Sapurina and J. Stejskal. “Oxidation of aniline with strong and weak oxidants”. In: *Russian Journal of General Chemistry* 82.2 (Feb. 2012), pp. 256–275. DOI: 10.1134/s1070363212020168.

[130] Yuxiu Li et al. “One-step synthesis of ultra-long silver nanowires of over 100 um and their application in flexible transparent conductive films”. In: *RSC Advances* 8.15 (2018), pp. 8057–8063. DOI: 10.1039/c7ra13683h.

[131] Dorota Buczynska et al. “Correlating Plasmon Polariton Propagation and Fluorescence Enhancement in Single Silver Nanowires”. In: *The Journal of Physical Chemistry C* 124.28 (June 2020), pp. 15418–15424. DOI: 10.1021/acs.jpcc.0c02364.

[132] Encai Hao and George C. Schatz. “Electromagnetic fields around silver nanoparticles and dimers”. In: *The Journal of Chemical Physics* 120.1 (Jan. 2004), pp. 357–366. DOI: 10.1063/1.1629280.

[133] Arti Vaish and Harish Parthasarathy. “ANALYSIS OF A RECTANGULAR WAVEGUIDE USING FINITE ELEMENT METHOD”. In: *Progress In Electromagnetics Research C* 2 (2008), pp. 117–125. DOI: 10.2528/pierc08031801.

[134] Marcin Szalkowski et al. “Wide-Field Fluorescence Microscopy of Real-Time Bioconjugation Sensing”. In: *Sensors* 18.1 (Jan. 2018), p. 290. DOI: 10.3390/s18010290.

[135] Foske J. Kleima et al. “Peridinin Chlorophyll a Protein: Relating Structure and Steady-State Spectroscopy”. In: *Biochemistry* 39.17 (Apr. 2000), pp. 5184–5195. DOI: 10.1021/bi992427s.

[136] Yeechi Chen et al. “Excitation enhancement of CdSe quantum dots by single metal nanoparticles”. In: *Applied Physics Letters* 93.5 (Aug. 2008), p. 053106. DOI: 10.1063/1.2956391.

[137] Sebastian Mackowski et al. “Metal-Enhanced Fluorescence of Chlorophylls in Single Light-Harvesting Complexes”. In: *Nano Letters* 8.2 (Dec. 2007), pp. 558–564. DOI: 10.1021/nl072854o.

[138] Maciej Bialy et al. “Controlled encapsulation of colloidal semiconductor quantum dots in a microdroplet”. In: *Phys. Chem. Chem. Phys.* (2024), pp. -. DOI: 10.1039/D4CP03419H.

[139] Dileep Mampallil and Huseyin Burak Eral. “A review on suppression and utilization of the coffee-ring effect”. In: *Advances in Colloid and Interface Science* 252 (Feb. 2018), pp. 38–54. DOI: 10.1016/j.cis.2017.12.008.

3.7 Appendix

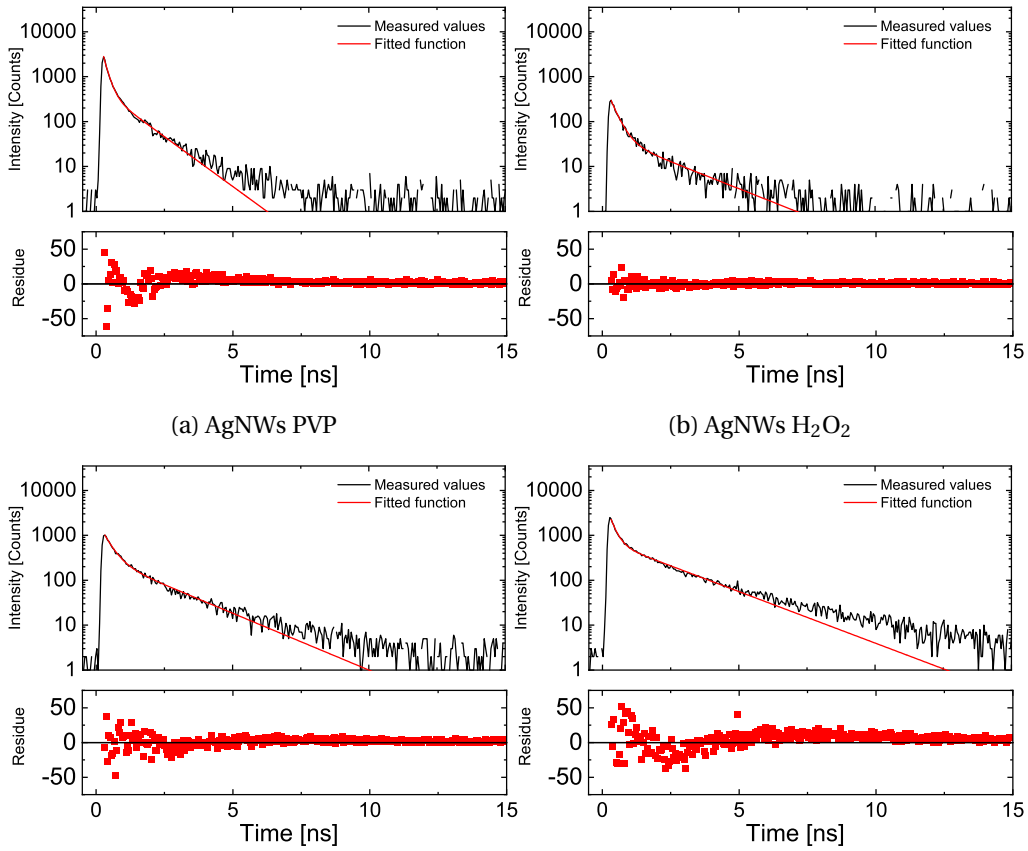

(a) AgNWs PVP

(b) AgNWs H_2O_2

(c) AgNWs aniline+H_2O_2

(d) AgNWs aniline

Figure 3.47: Fluorescence decay curves of layer of PCP at AgNWs with fitted biexponential functions and their residues.

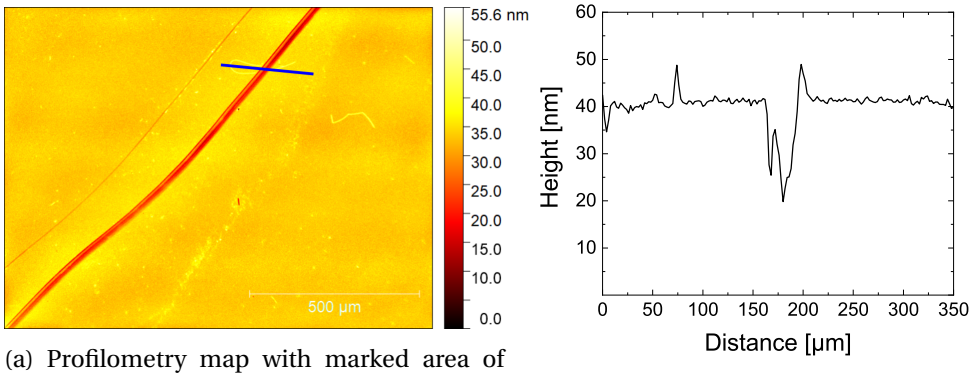

(a) Profilometry map with marked area of height profile (blue line)

(b) height profile

Figure 3.48: Profilometric map of the height of the sample obtained by spinocoating a mixture of AgNWs, PVA and PCP, with marked height profile and corresponding graph. The line visible in diagonal is a scratch made to remove polymer layer from the sample.

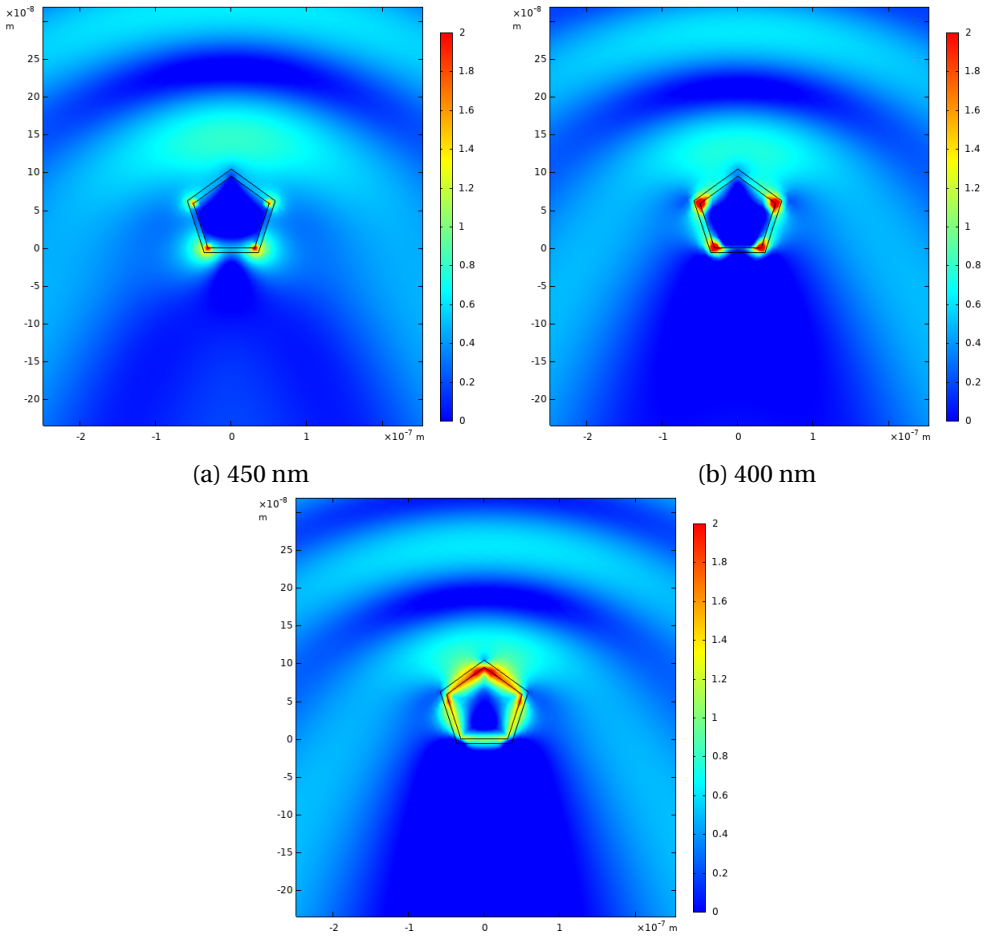

(a) 450 nm

(b) 400 nm

(c) 360 nm

Figure 3.49: Logarithmic electric field distribution around 100 nm wide silver nanowire for (a) 450 nm, (b) 400 nm, (c) 360 nm exicatation.

LIST OF PUBLICATIONS

- Ćwik, M., Buczyńska, D., Sulowska, K., Roźniecka, E., Mackowski, S., Niedziółka-Jönsson, J. (2019). Optical Properties of Submillimeter Silver Nanowires Synthesized Using the Hydrothermal Method. Materials (Basel, Switzerland), 12(5), 721. https://doi.org/10.3390/ma12050721

- Buczyńska, D., Ćwik, M., Roźniecka, E., Sulowska, K., Piatkowski, D., Maćkowski, S., Niedziółka-Jönsson, J. (2020). Correlating Plasmon Polariton Propagation and Fluorescence Enhancement in Single Silver Nanowires. The Journal of Physical Chemistry C, 124(28), 15418–15424. https://doi.org/10.1021/acs.jpcc.0c02364

- Ćwik, M., Sulowska, K., Buczyńska, D., Roźniecka, E., Domagalska, M., Maćkowski, S., Niedziółka-Jönsson, J. (2021). Controlling plasmon propagation and enhancement via reducing agent in wet chemistry synthesized silver nanowires. Optics Express, 29(6), 8834. https://doi.org/10.1364/oe.412903

- Maciej Biały, Karolina Sulowska, Kamil Wiwatowski, Michał Ćwik, Dorota Buczyńska, Wojciech Nogala, Martin Jonsson-Niedziółka, Dawid Piątkowski, Sebastian Maćkowski, and Joanna Niedziółka-Jonsson The Journal of Physical Chemistry C 2025 129 (2), 1260-1269 DOI: 10.1021/acs.jpcc.4c05904

CONFERENCES

- XXI. Annual Linz Winter Workshop (Linz, AUSTRIA) January 28, 2019 - February 4, 2019 Advances in Single-Molecule Research for Biology Nanoscience Optical properties of ultra-long silver nanowires synthesized using hydrothermal method

- Molecular Plasmonics (Jena, GERMANY) 23 -25 May, 2019 Optical properties of ultra-long silver nanowires synthesized using hydrothermal method

- 62. Zjazd naukowy PTChem (Warsaw, POLAND), 2-6 September 2019 Własności optyczne ultradługich nanodrutów srebra otrzymanych metodą hydrotermalną

- META 2020, the 11th International Conference on Metamaterials, Photonic Crystals and Plasmonics (Warsaw, POLAND), 20-23 July, 2021 Silver nanowires - remotely excited (bio)sensors